Max Planck Institute of Colloid and Interfaces

Interfaces Department

Nucleation and Growth of Unsubstituted Metal Phthalocyanine Films from Solution on Planar Substrates

Dissertation
zur Erlangung des akademischen Grades
"doctor rerum naturalium"
(Dr. rer. nat.)
in der Wissenschaftsdisziplin Physik

eingereicht an der
Mathematisch-Naturwissenschaftlichen Fakultät
der Universität Potsdam

von

Fatemeh Ghani

Potsdam, November 2012

Abstract

Organic solar cells (OSC) are interesting as low cost alternative to conventional solar cells. Unsubstituted Metal-phthalocyanines (Pc) are excellent electron donating molecules for heterojunction OSC. Usually organic solar cells with Pcs are produced by vapor deposition, although solution based deposition (like spin casting) is cheaper and offers more possibilities to control the structure of the film. With solution based deposition several parameters (like temperature, solvent and etc.) affect the self-organized structure formation via nucleation and growth. The reason why vapor deposition is typically used is the poor solubility of the metal-phthalocyanines in most common solvents. Furthermore the process of nucleation and growth of Pc aggregates from solution is not well understood. For preparation of Pc films from solution, it is necessary to find the appropriate solvents, assess the solution deposition techniques, such as dip coating, and spin casting. It is necessary to understand the nucleation and growth process for aggregation/precipitation and to use this knowledge to produce nanostructures appropriate for OSC. This is important because the nanostructure of the films determines their performance.

In this thesis, optical absorption and the stability of 8 different unsubstituted metal Pc's were studied quantitatively in 28 different solvents. Among the several solution based deposited thin films produced based on this study, copper phthalocyanine (CuPc) dissolved in trifluoroacetic acid (TFA) is chosen as a model system for an in-depth study. CuPc has sufficient solubility and stability in TFA and upon solution processing forms appropriate structures for OSCs. CuPc molecules aggregate into layers of nanoribbons with a thickness of ~ 1 nm and an adjustable width and length. The morphology and the number of deposited layers in the thin films are controlled by different parameters, like temperature and solution concentration. Material properties of CuPc deposited from TFA are studied in detail via x-ray diffraction, UV-Vis and FT-IR spectroscopy. Atomic force microscopy was used to study the morphology of the dried film.

The mechanism of the formation of CuPc nanoribbons from spin casted CuPc/TFA solution in ambient temperature is investigated and explained. The parameters (e.g. solution concentration profile) governing nucleation and growth are calculated based on the spin casting theory of a binary mixture of a nonvolatile solute and evaporative solvent. Based on this and intermolecular interactions between CuPc and substrate a nucleation and growth model is developed explaining the aggregation of CuPc in a supersaturated TFA solution.

Finally, a solution processed thin film of CuPc is applied as a donor layer in a functioning bilayer heterojunction OSC and the influence of the structure on OSC performance is studied.

Keywords: Copper Phthalocyanine, Adsorption, nucleation and growth, Spin casting, Organic Solar Cell.

Dedication

To my parents

List of abbreviations

Phthalocyanine:

Pc	Phthalocyanine
MPc	Metal phthalocyanine
CoPc	Cobalt phthalocyanine
CuPc	Copper phthalocyanine
FePc	Iron phthalocyanine
MgPc	Magnesium phthalocyanine
MnPc	Manganese phthalocyanine
NiPc	Nickel phthalocyanine
SnPc	Tin phthalocyanine
ZnPc	Zinc phthalocyanine

Other molecules:

C_{60}	Buckminsterfullerene-C60
Al	Aluminium
BCP	Bathocuproine
PCBM	Phenyl-C61-butyric acid methyl ester
Acids:	
AA	Acetic acids
FA	Formic acid
PA	Phosphoric acid
SA	Sulfuric acid
TFA	Trifluoroacetic acid
Ionic liquids:	
STOR	1-Ethyl-3-methylimidazoliumacetate
EMIM	1-Ethyl-3-methylimidazoliumethyl sulfate
Conventional	solvents:
ACN	Acetonitrile
CBZ	Chlorbenzene
TCM	Chloroform

DCM	Dichloromethane
DMAC	Dimethylacetamide
DMF	Dimethylformamide
DMPU	1,3-Dimethyl-3,4,5,6-tetrahydro-2(1H)-pyrimidinone
DMSO	Dimethyl sulfoxide
EtOH	Ethanol
EtOAc	Ethyl acetate
IPA	Isopropanol
MeOH	Methanol
NMP	N-Methyl-2-pyrrolidone
THF	Tetrahydrofuran

Substrates:

SiO_2	Silicon dioxide
ITO	Indium tin oxide sputtered on glass substrate

Methods and etc.

UV-Vis	Ultra violet-visible
FT-IR	Fourier transform infrared
XRPD	x-ray powder diffraction
XRR	x-ray reflectivity
AFM	Atomic force microscopy
TEM	Transmission electron microscopy
Cryo-TEM	Cryogenic transmission electron microscopy
SEM	Scanning electron microscopy
OSC	Organic solar cell

HOMO	Highest occupied molecular orbital
LUMO	Lowest unoccupied molecular orbital

Preface

Die vorliegende Arbeit ist während meiner Tätigkeit als Wissenschaftliche Mitarbeiterin in der Arbeitsgruppe von Herrn Dr. Hans Riegler am Max-Planck-Institut unter der Leitung von Herrn Prof. Dr. Möhwald entstanden. Die Motivation zu der behandelten Thematik entstammt meiner wissenschaftlichen Arbeit im Rahmen der Forschungsschwerpunkte des Fachgebiets sowie in dem vom Bundesministerium für Bildung und Forschung (BMBF) geförderten Forschungsprojekt (Project 03X3525F, SOHyb – Keimbildungsinduzierte Selbstorganisation zur Strukturierung organischer Hybridsolarzellen).

Index

1. Introduction

Research focus, back ground and motivation

Urgent needs to reduce CO_2 emission have raised the interest in renewable energy sources, such as using solar energy to produce electricity. Organic solar cells (OSC) are new systems promising cost-efficient production with low environmental impact [1]. Many researchers focus on the production of OSCs, understanding their physical and chemical parameter and improving them [2]. A typical heterojunction OSC is made of two layers of electron accepting and donating organic material sandwiched between two inorganic conductive electrodes [3]. The configuration of the nanostructure within these layers is an important parameter which influence the energy conversion efficiency [4]. A nanostructure network in the range of the diffusion length of the exciton (electron-hole bound state), < 100 nm, is promising for effective exciton diffusion to the interface, charge generation and collection [5]. Understanding and controlling the parameters which influence the nanostructure formation is one approach to increase the energy conversion efficiency. This research work is aimed to produce structures of small molecules (phthalocyanine) from cost-efficient solution based deposition techniques, like spin casting, and to understand the nucleation and growth of the aggregates on the surface from solution.

Metal phthalocyanines (MPc) have attracted considerable attention due to their unique optical and electronic properties [6] as well as their chemical and thermal stability [7]. They are molecular organic semiconductors [8] with numerous applications, such as organic solar cells [5, 9-11], chemical sensors [12-15], field effect transistors [16-18], and optical data storage [19-21]. Recently, highly efficient organic solar cells containing phthalocyanines were produced [22] exploiting their favorable optical and electronic properties, like the large absorption coefficient and an energy band gap, which matches the solar spectrum [6, 7, 23]. Additionally, phthalocyanines are attractive for organic photovoltaics due to their low material costs [24]. It is interesting to use low cost and simple device preparation via solution processing [25-27], like roll-to-roll processing [28], ink-jet printing [29], or spin casting [30]. The poor solubility of the unsubstituted molecule in common solvents hinders using these methods [31, 32]. Two strategies are currently used to overcome this problem. One focuses on chemical functionalization of the molecule, which decreases the conductivity of the Pc and degrades the performance of the OSC [33]. Modification substantially increases the material cost compared to the readily available unsubstituted Pcs [6, 34, 35]. The second approach applies high vacuum vapor deposition, which is cost extensive and technically complicated [36].

Clearly, it is desirable to find appropriate solvents for unsubstituted Pcs to be used for deposition of a thin film by solution processing techniques. Solution based deposited thin films of Pcs are still new. Most of the studies concentrate on production of such thin films from vapor phase [37-40] or application in devices [41-45]. The mechanism of the film formation (nucleation and growth) is still not well understood. Especially it is interesting to investigate parameters which influence the formation of nanostructures in the film. These parameters can be controlled to influence the size and shape of the nanostructure and produce structures favorable for the application in OSCs.

Objectives

The goals of this thesis are to understand the film formation mechanism (nucleation and growth) of unsubstituted metal phthalocyanine via solution based deposition techniques like spin casting or dip coating, to find the parameters to control the film structure, to produce thin films, and apply them in OSCs.

In the first step to overcome the solubility problem, a systematic study on the solubility of unsubstituted metal phthalocyanines in different solvents including conventional standard solvents, acids and ionic liquids is performed. The solubility, stability and absorption coefficient is investigated by absorption spectroscopy. With the help of these results, solution based deposited thin films of unsubstituted phthalocyanines were produced. Among several thin films deposited via spin casting and dip coating, novel structures of CuPc nanoribbons were found. The structures form on SiO_2, glass or ITO surfaces after evaporation of the solvent from CuPc/TFA solution. Similar structures are produced with other unsubstituted metal Pcs dissolved in TFA. Due to the chemical stability [46], reliable organic semiconducting properties of CuPc [47] and applicability in organic photovoltaic devices [48], the preparation of a thin film of CuPc from solution is studied in detail. The parameters which control the film morphology like concentration of solution and temperature were investigated. Furthermore material properties and the mechanism of the formation of the CuPc structures deposited from supersaturated solution are studied. Especially, the parameters which play an important role in supersaturation of CuPc solution, nucleation and growth of the thin film are discussed. The aggregation of CuPc from solution by evaporation of solvent is explained based on nucleation and growth in a binary nonvolatile solute and evaporating solvent mixture.

This thin film is applied in a heterojunction bilayer OSCs. It demonstrates the practical feasibility of technically rather simple wet processing of heterojunction bilayer OSCs containing Pcs without chemically modifying the Pcs. The approach can be extended to an all-wet-processing preparation of OSCs by the sequential use of suitable “orthogonal” solvents i.e., solvents that do not dissolve the underlying layer upon deposition of a new one.

Outline

Chapter 2 of this thesis focuses on the theoretical background and methods used. First the theory of nucleation, growth and adsorption is explained. Properties of phthalocyanines are briefly introduced. The theory of spin casting and dip coating in preparation of a thin film from solution is explained briefly. Also heterojunction organic solar cell is introduced briefly. Chapter 3 contains experimental details on materials, on sample preparation and measurement methods. Chapter 4 presents the result of solubility studies of eight unsubstituted metal-phthalocyanines and their stability and optical absorption. Chapter 5 presents examples of thin films prepared using the results of the solubility study. Findings on the influence of concentration and temperature on structures prepared by dip coating of CuPc/TFA solution are presented in this chapter. In Chapter 6 the material characteristics measured on CuPc dissolved in and deposited from TFA are explained. In chapter 7 a nucleation and growth model is developed to explain the formation mechanism of CuPc into nanoribbons by deposition from TFA solution. In chapter 8 the application as a donor film in hybrid organic solar cells is investigated. The appendix contains further measurements and descriptions which support the arguments in the main body.

2. Scientific Background

Chapter overview: This chapter aims to provide an overview for understanding the following chapters. Nucleation and growth in solution based deposited films are introduced. Adsorption models and solution processed thin film deposition techniques are described. Pc molecules and some information on their characteristic properties are presented. Finally OSC architecture and function are introduced.

2.1 Solution based film deposition

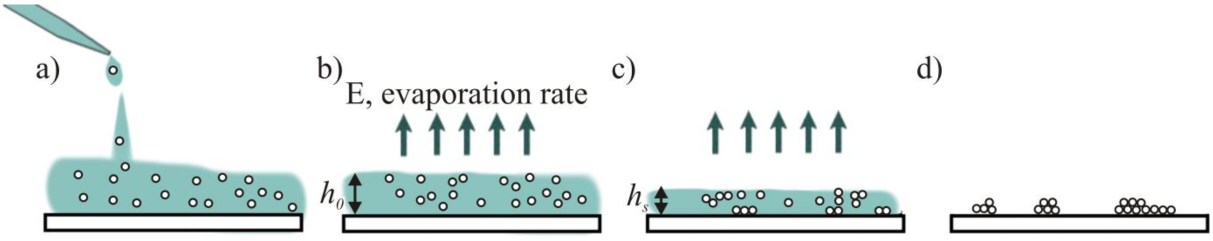

Figure 2-1 a) A solution is placed onto the substrate, b) an evaporating liquid film with the thickness h_0 and concentration c_0 is formed, c) the solution becomes supersaturated at the thickness h_s and concentration c_s and the solute start to aggregate, d) the solvent has completely evaporated and a film of solute remains on the substrate.

In solution based deposition a substance (solute) is deposited onto the substrate from a solution, see Figure 2-1. The process is described based on the model of a mixture of the nonvolatile solute and evaporating solvent. The solution containing the solute is placed onto the substrate, Figure 2-1a. A liquid film with a thickness (h_0) and concentration (c_0) covers the substrate. From this liquid film, the solvent evaporates, Figure 2-1b. Because of evaporation, the liquid film thickness reduces and the solution becomes concentrated. When the solution becomes supersaturated (concentration c_s and height h_s), the solute starts to aggregate (nucleation and growth), Figure 2-1c. After complete solvent evaporation, a film of solute remains on the substrate, Figure 2-1d [49].

2.1.1 Nucleation

Two steps are essential in the formation of a solid assembly from solution: first the formation of a stable aggregate (nucleus) and then growth of the nucleus into a larger aggregate. Before supersaturation, molecules or ions (solute) in solution collide and sometimes form aggregates and dissolve again in solution. In a supersaturated solution these aggregates reach a critical size. Aggregates equal to or larger than the critical size do not dissolve again and are stable. These aggregates are called nuclei. After nucleus formation the aggregates grows further relatively unimpeded [49].

There are two classes of nucleation: homogenous and heterogeneous nucleation. Homogenous nucleation is the spontaneous formation of a new phase inside a uniform phase. Heterogeneous nucleation is the aggregation in the presence of an interface (a foreign surface). A heterogeneous nucleation has a lower barrier than of the homogeneous nucleation, therefore most nucleation processes are heterogeneous nucleation [49, 50].

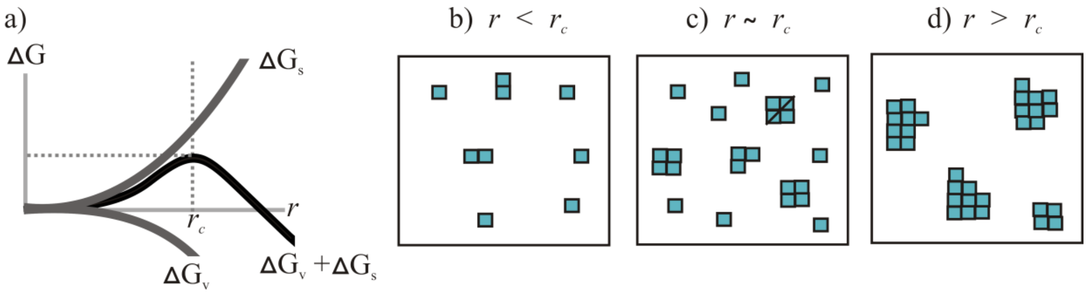

Figure 2-2 a) Surface Gibbs free energy, ΔG_s, and volume free energy, ΔG_v, in formation of aggregate as a function of aggregate radius. b) $r < r_c$ formation of unstable aggregate, c) $r \sim r_c$ formation of nuclei, d) $r > r_c$ growth of nuclei.

Homogenous nucleation: when the solution becomes supersaturated, the Gibbs free energy of the system increases. The overall Gibbs free energy of a supersaturated solution can be reduced by segregation of solute from the solution, i.e. aggregation. The changes of Gibbs free energy (ΔG) by formation of a cluster have two terms. 1) The volume Gibbs free energy for the transformation of growth-units from solution into solid phase (ΔG_{vol}):

$$\Delta G_{vol} = -n\,\Delta g \tag{2-1}$$

Where, Δg is the difference in molar free enthalpy of the two phases. It is clear that by increasing the concentration of the solution the Gibbs free energy of aggregation per volume decreases. 2) This energy reduction is opposed by the interface energy. The total change of the Gibbs free energy for the formation of a spherical aggregate in the solution is described as:

$$\Delta G = \Delta G_{vol} + \Delta G_{sur} = -\frac{4}{3}\pi r^3 \frac{1}{a^3}\Delta g + 4\pi r^2 \gamma \tag{2-2}$$

Where γ is the interface energy per unit area and *r* is the aggregate radius, *a* is the size of the solute molecules. Figure 2-2a shows the changes in the Gibbs free energy as a function of aggregate radius. From this figure it is clear that an aggregate with radius smaller than r_c, dissolves and reduces the overall free energy. The nucleus forms when the radius of the aggregate exceeds the critical size, r_c, Figure 2-2b and 2-2c. An aggregate larger than r_c (nucleus) grows spontaneously, Figure 2-2d [49, 51-54].

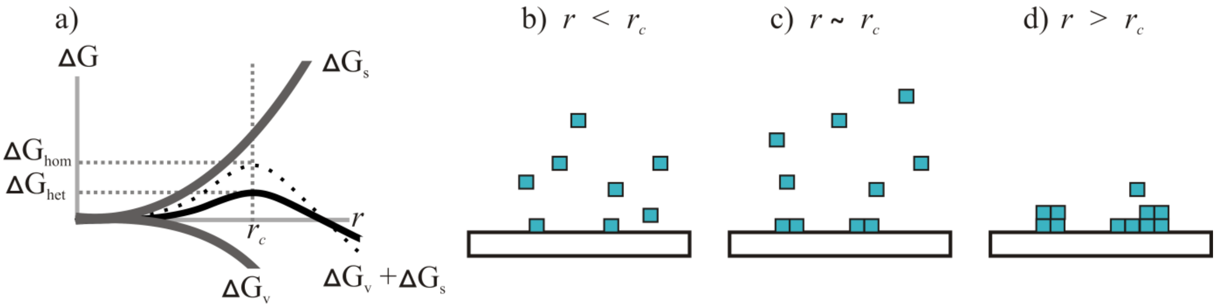

Figure 2-3 a) Gibbs free energy of homogeneous, ΔG_{hom}, and heterogeneous, ΔG_{het}, nucleation as a function of aggregate's radius. b) $r < r_c$ formation of unstable aggregate, c) $r \sim r_c$ heterogeneous nucleation on a substrate, d) $r > r_c$ growth of nuclei.

Heterogeneous nucleation: heterogeneous nucleation is occurring when a wetting surface is involved. For instance, instead of spherical nuclei in the bulk, spherical cap-shaped nuclei are formed at the interface. For a drop which is almost wetting the surface, the radius of curvature of the drop surface is larger than the radius of a sphere of the same volume, so that the drop nucleates at a smaller total Gibbs free energy, see Figure 2-3a. The change of Gibbs free energy by formation of a cluster is again calculated from the contributions of the volume and interfaces. Geometrical calculations and the force balance of the surface tensions of a partially wetting droplet show that in heterogeneous nucleation the Gibbs free energy of homogeneous nucleation is reduced by a function of the contact angle ($f(\theta)$):

$$\Delta G_{het} = \Delta G_{hom} f(\theta) \tag{2-3}$$

Therefore the phase transition starts at smaller supersaturation concentration rather than homogeneous nucleation [49, 52, 53, 55, 56].

Nucleation is influenced by temperature, type of the solvent, additive in the solvent, and impurities in solvents. For instance, Cao et al report that the critical size of nanoparticles by preparation from supersaturated solution increases with temperature, since temperature influences supersaturation and also interface energy [54].

2.1.2 Growth

After the nucleation, the aggregates grow by attachment of the solute to the nucleus. Kossel [57] and Stranski [58] introduce a model to explain the growth of an ionic crystal (e.g NaCl cubic lattice). In this model the ions can attach to different surface sites (six sites in case of the cubic lattice). Each site has an individual potential energy. Growth from solution involves also transport of ions to the solid surface (diffusion) and adsorption of the ions to the solid surface [49, 52, 53, 56].

The growth process is influenced by concentration gradient due to material diffusion [59]. When atoms and molecules in some volume attach to a nucleus, a depletion region appears around the nucleus where the concentration is smaller. The size of the depletion and its influence on the growth depend on the aggregation rate and diffusion of the solute in the solution [55, 60]. The parameters which influence the growth, like growth rate, diffusion of solute in solution depend on the studied system [54, 56].

2.2 Adsorption models

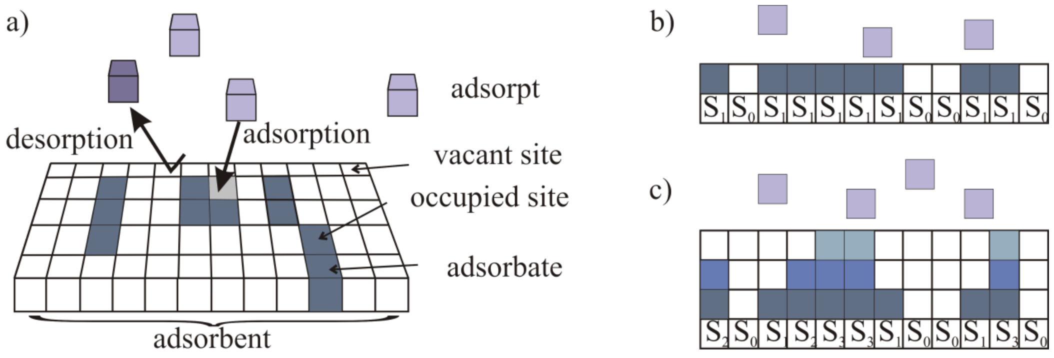

Figure 2-4 a) Schematic drawing of adsorption b) Langmuir for monolayer, c) BET for multilayer adsorption

The material onto which the adsorption takes place is called adsorbent; the substance in the adsorbed state is called adsorbate and the substance to be adsorbed, adsorptive or adsorpt, see Figure 2-4a. In adsorption the adsorbed substance can desorb from and adsorb again onto the surface. The amount of adsorbed substance is described by the number of adsorbed moles per area, Γ. This amount, Γ, depends on several parameters, such as temperature, partial pressure (in case of adsorption by evaporation) or concentration (in case of adsorption from solution) [53, 55]. The adsorption experiments are usually performed at constant temperature. An empirical or theoretical expression of the adsorbed material as a function of pressure or concentration at constant temperature is called adsorption isotherm. Adsorption isotherms help to understand the adsorption process and predict the amount of adsorbed material.

In the following, the most famous adsorption models, Langmuir and BET see Figure 2-4b and 2-4c, are introduced. The Sigmoid adsorption model used to explain the result in chapter 7 is described afterwards.

2.2.1 Langmuir and BET adsorption

Langmuir assumes that there is a certain number of binding sites in a monolayer on the substrate per area S. S_1 is the number of occupied and $S_0 = S\text{-}S_1$ is the number of vacant sites, see Figure 2-4b. The adsorption is proportional to the number of vacant sites S_0, and the number of adsorbate molecules, i.e. concentration in solution or pressure in gas, $k_{ad}\, S_0\, P$. In Langmuir adsorption each binding site can bind just one molecule and the binding energy is independent of the other bound molecules. In equilibrium the adsorption, $k_{ad} S_0$, and desorption rate, $k_{de} S_1$, are equal. The coverage of the surface is [49, 53]:

$$\Theta = \frac{S_1}{S} = \frac{k_{ad} P}{k_{de} + k_{ad} P} \tag{2-4}$$

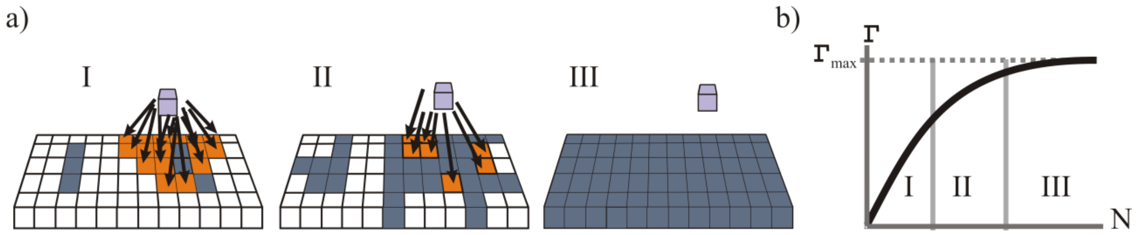

Figure 2-5 a) Schematic drawing of a Langmuir adsorption, b) isotherm as a function of amount of deposited material: At low coverage more vacant sites are available on the substrate and the adsorption rate is large (I). As the vacant sites are filled, the adsorption rate decreases (II) and becomes zero (III).

Alternatively the adsorption isotherm can be expressed by introduction of the equilibrium constant $K_L = k_{ad}/k_{de}$ and the maximum number of adsorbed moles per area where all the binding sites are occupied, Γ_{mon}:

$$\Gamma = \frac{\Gamma_{mon} K_L P}{1 + K_L P} \tag{2-5}$$

The Langmuir model explains the adsorption only for one monolayer, figure 2-5a and 2-5b. For multilayer adsorption, the BET model is used; see Figure 2-4c. The BET model (Stephen Brunauer, P. H. Emmett , Edward Teller) [61] assumes a Langmuir adsorption in each layer. It considers that each layer has a particular adsorption heat, Q_i. Also adsorption is only taking place without including lateral interaction between the adsorpt and adsorbate. The adsorbed molecules cannot move between adsorbed layers and the desorption rate in each layer is proportional to the adsorption heat, so that the adsorption to a vacant site in each layer is expressed by a rate of $k^i_{ad} P S_{i-1}$ and the desorption by $a_i S exp(-Q_i/RT)$. The adsorption isotherm is obtained by addition of the total number of adsorbed mole per area. Assuming:

$$\alpha = \frac{k_{ad}^{1}P}{a_1} e^{Q_1/RT} \quad \text{and} \quad \beta = \frac{k_{ad}^{i}P}{a_i} e^{Q_i/RT}, \beta = {}^{P}/_{P_0} \tag{2-6}$$

one obtains:

$$S_1 = \alpha\, S_0 \quad \text{and}\; S_i = \alpha\ \beta^{i-1}\, S_0 = C\, \beta^i\, S_0 \tag{2-7}$$

The BET adsorption depends on the C and β, according to:

$$\Gamma = \frac{C\,\beta}{(1-\beta)(1-\beta+C\beta)}\Gamma_{mon} \tag{2-8}$$

2.2.2 Sigmoidal adsorption

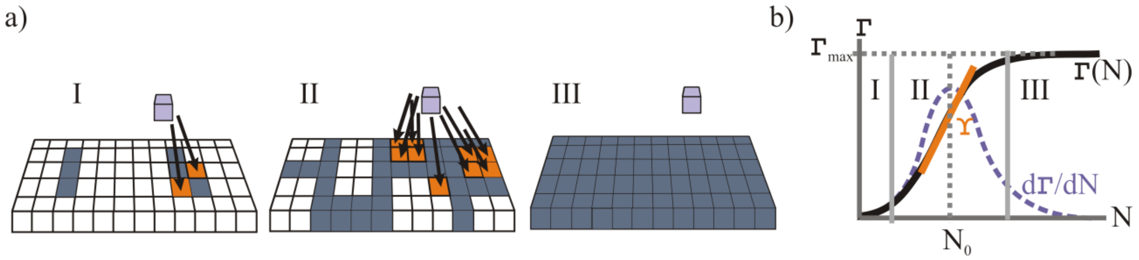

Figure 2-6) Schematic drawing of a sigmoidal adsorption, b) isotherm as a function of amount of deposited material (N) and the adsorption rate: At low coverage small amount of material is available and the adsorption rate is small (I). As the vacant sites are filled, the adsorption rate decreases due to the lateral interaction of adsorbing and adsorbed material (II), and as the substrate is filled up the adsorption rate becomes zero (III).

Sigmoidal adsorption involves a cooperative effect. In this case the molecules attach stronger to a surface if they interact with neighboring adsorbed molecules [53]. At low amounts of adsorbed material ($N << N_0$,) few adsorbate can interact with the adsorpt, Figure 2-6a (II. As the fraction of adsorbate increases, the adsorbing molecules find more possibilities for interaction with the adsorbed molecules, therefore the adsorption rate increases; Figure 2-6a (II). As the fraction of adsorbate further increases ($N >> N_0$), less free places are available for the adsorpt, so that the adsorbent becomes saturated with the adsorbate and the adsorption rate decreases to zero, Figure 2-6a (III). Such an adsorption curve has a sigmoidal shape:

$$\Gamma(N) = \frac{\Gamma_{max}}{1 + e^{-\gamma(N-N_0)}} \tag{2-9}$$

At the inflection point (N_0) of the sigmoid function the adsorption rate ($d\Gamma/dN$) has a maximum [62], see Figure 2-6b. The amount of adsorbed material (N_0) is large enough to provide many binding sites that the adsorpt and the adsorbent is not saturated ($\Gamma(N) = \Gamma_{max}/2$). By increasing the amount of adsorbed material, the amount of vacant sites on the adsorbent decreases ($\Gamma(N) >> \Gamma_{max}/2$) so that the adsorption rate also decreases. When the adsorbent becomes saturated the amount of adsorbed material is maximal (Γ_{max}) and the adsorption rate decreases to zero.

The Langmuir model can be modified to include also lateral interactions by including the energy term of binding sites for neighboring adsorbed molecules. For that it is assumed that the average number of binding sites of an adsorbed molecule is $n\theta$ and the additional energy per bond is E. The Langmuir constant changes to [63]:

$$K_L' = K_L \exp\left(\frac{Q + n\theta E}{RT}\right) \tag{2-10}$$

Using this constant as Langmuir constant in the adsorption isotherm gives the adsorption isotherm including the lateral interaction between the neighboring atoms. This model is also called also Frumkin–Fowler–Guggenheim [64, 65].

2.3 Solution based deposition

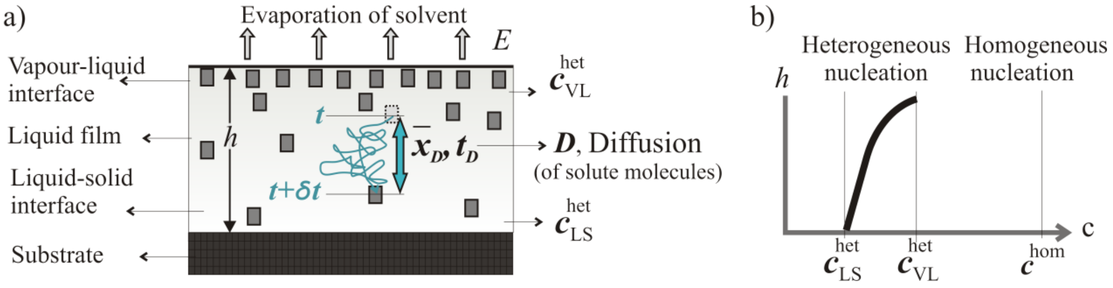

Figure 2-7 a) Schematic drawing of a liquid film with a height h and evaporation rate E, solute concentration c, and diffusion coefficient D; b) Concentration of solution at the vapor-liquid, liquid-solid interface

In solution based deposition, like spin casting, a liquid film with a thickness *h* is sandwiched between two interfaces: liquid-vapor (the liquid film and the solvent vapor in ambient air) and solid-liquid (the solid substrate and the liquid film), see Figure 2-7a. From the liquid-vapor interface the solvent evaporates. Therefore a layer with higher concentration forms near this interface. From this layer the solute molecules diffuse through the liquid film causing the concentration increase in the liquid film. The concentration gradient in the liquid film depends on the diffusion coefficient (*D*) of the solute molecule in the liquid film with a thickness (*h*) and the evaporation rate of solvent (*E*) [66]. E.g. when in an arbitrary time interval the diffusion distance of solute molecules is much larger than the liquid film thickness, *h*, the concentration, *c*, remains almost uniform in that time interval.

During evaporation the concentration of solute molecules increases. At any point where supersaturation is reached, nucleation starts. Generally there are three regions for nucleation, 1) homogeneous nucleation in the liquid film away from any interface, 2) heterogeneous nucleation at liquid-vapor interface or 3) at solid-liquid interface. Heterogonous nucleation starts earlier at any interface (heterogeneous) [56]. There are two regions for heterogeneous nucleation:

1) Liquid-vapor interface especially because the concentration near to this interface is higher due to evaporation, see Figure 2-7b. Even with relatively large diffusion in the liquid film there is always a concentration increase due to evaporation. Therefore the solute concentration is always higher near this interface, compared to elsewhere in the solution.
2) The solid-liquid interface near the solid surface of the substrate. The concentration near this interface depends on the diffusion and evaporation rate. If the diffusion is effective enough the concentration gradient will be small. If the tendency of solute molecules to adsorb and nucleate on the substrate is strong enough then they start to aggregate near the supersaturation concentration. Although the solute concentration is smaller near this interface, the nucleation start earlier at the substrate.

The concentration gradient in the liquid film (influenced by evaporation rate and diffusion coefficient in the liquid film of thickness *h*) and solute-substrate interaction are two major parameters determining where nucleation starts.

After supersaturation nuclei may form and then the growth starts. Due to the adsorption of the molecules from solution into nuclei, the concentration decreases at growth front. Simultaneously evaporation causes a concentration increase. The competition between evaporation and aggregation cause the concentration in supersaturation state to be almost constant, until the solvent is completely evaporated. Thus, the rate of the aggregation after supersaturation is influenced by the evaporation rate. Furthermore at distances larger than the diffusion distance of the solute, concentration gradient appear. These concentration gradient may cause formation of new nuclei and influence the homogeneity of the patterns formed [67, 68] [54]. Therefore the shape and size of the deposited pattern is influenced by diffusion of solute molecules [69]. In case of spin or dip coating, the liquid film thickness is in the µm range and the experiments are performed at uniform temperature. In this range the process is isothermal and fluctuations due to heat transfer are negligible [70, 71].

Diffusion

In a fluid the material diffuses from higher to the lower concentration. The first Fick's law relates the diffusion of a flux J in such a medium to the concentration gradient in the steady state [55]:

$$J = -D\frac{\partial c}{\partial x} \tag{2-11}$$

D is the diffusion coefficient. The second Fick's law predicts that the concentration changes with time by diffusion according to:

$$\frac{\partial c}{\partial t} = D\frac{\partial^2 c}{\partial x^2} \tag{2-12}$$

The motion of an atom or molecule in a viscous medium can be modeled as the motion of a sphere. The force required to move such a sphere depends on the size of the sphere and the viscosity of the medium. The motion of atoms or molecules in a fluid is described by the Stokes-Einstein relation to first approximation, (η: viscosity of the fluid and a: diameter of the atom or molecule) [72]:

$$D = \frac{k_B T}{3\pi\eta a} \tag{2-13}$$

Spin casting

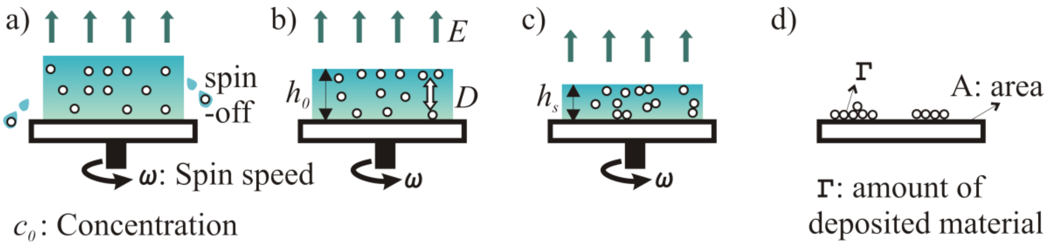

Figure 2-8) Schematic drawing of spin-casting indicating the dominant process at the beginning of the spin casting (spin-off) and later after the equilibrium liquid film thickness is reached.

For spin casting, a drop of liquid solution is placed onto a rotating substrate. The liquid spreads rapidly over the substrate due to the centrifugal forces, and the excess material is spun off at the edge of the substrate, Figure 2-8a. In the early stages of spin casting the rate of thinning by centrifugal forces is much greater than by evaporation. The thinning of a liquid film after spin-off is just due to evaporation and occurs constantly. The transition point between the spin off and evaporation stages is taken to be the point where the thinning rate due to evaporation is the same as the thinning rate due to centrifugal forces. The film thickness at the transition is defined as h_0, see Figure 2-8b. The time after reaching the transition point is called here drying time t_{drying}. Supersaturation, nucleation and growth occur in t_{drying}. The liquid film becomes supersaturated due to evaporation of the solvent, see Figure 2-8c. After complete evaporation, a solid film is deposited onto the substrate, Figure 2-8d [73, 74].

The film thinning for an ideal (Newtonian) liquid is described by Meyerhofer as [74]:

$$\frac{dh}{dt} = -2Kh^3 - E \tag{2-14}$$

where h: film thickness, E: evaporation rate and K: Spin-off coefficient, which is defined as:

$$K = \frac{\omega^2}{3\nu} \tag{2-15}$$

here *ω* is the spinning speed, *v*, the kinetic viscosity of the liquid. Karpitschka et al. solved the equation analytically, if the evaporation rate is constant. The amount of material deposited at the end of the spinning process in the dry film is [75]:

$$\Gamma = \frac{N(h \rightarrow 0)}{A} \approx 0.8\, c_0 \left(\frac{E}{K}\right)^{\frac{1}{3}} \approx c_0 \left(\frac{E}{3\nu}\right)^{\frac{1}{3}} \omega^{-\frac{2}{3}} \tag{2-16}$$

here *N* is the amount of material and *A* is the surface area. The equation above describes that the amount of deposited material can be controlled by the initial concentration, evaporation rate, and spinning speed.

Dip coating

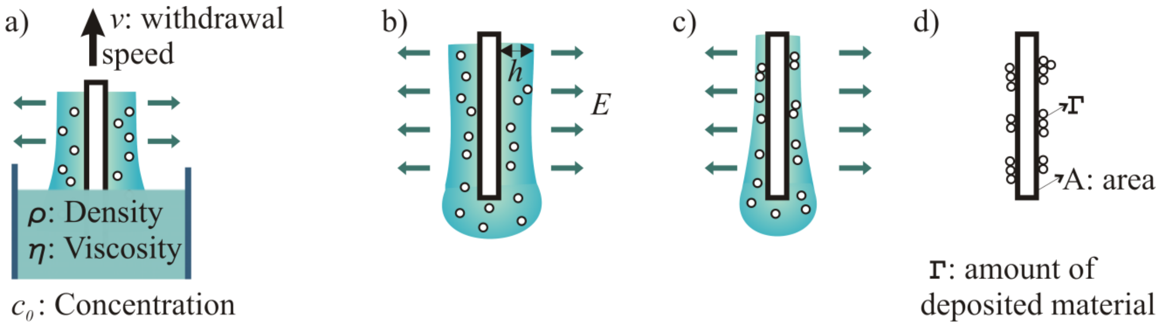

Figure 2-9) Schematic drawing of the dip coating process including the different steps: a, b) immersing the substrate into solution and withdrawing the substrate and solvent evaporation, c,d) solvent evaporation and drying.

Dip coating is also a solution deposition technique. The substrate is immersed into the solution and withdrawn at a constant speed, *v*, Figure 2-9a. As the substrate is withdrawn from solution, a liquid film covers the substrate, Figure 2-9b. The film flows down until an hydrodynamic equilibrium thickness is reached, Figure 2-9c. This equilibrium thin film is defined where evaporation is neglected. The withdrawal speed (*v*), the viscosity (*η*) and density (*ρ*) of the liquid are the main parameters determining the thickness of the liquid film [76, 77]. Landau and Levich calculated the coating thickness, *h* [78]:

$$h = \frac{(\eta \cdot v)^{2/3}}{\Upsilon_{LV}^{1/6} (\rho \cdot g)^{1/2}} \tag{2-17}$$

Where Υ_{LV} is the liquid-vapor surface tension and g: gravity. After complete solvent evaporation, the solid film remains on the substrate, 2-9d. Consequently, the amount of deposited material is:

$$\Gamma = \frac{N(h \to 0)}{A} \approx c_0 . h \tag{2-18}$$

2.4 Phthalocyanine molecule

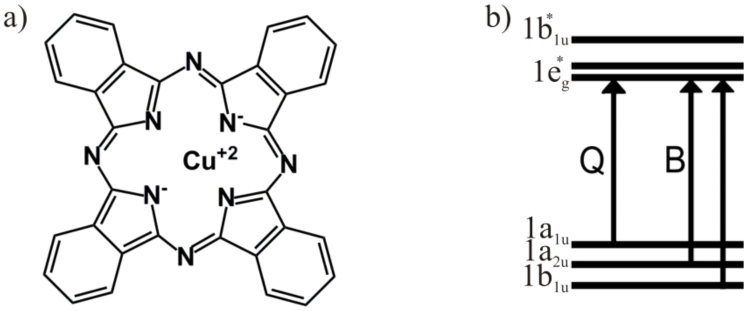

Figure 2-10 a) Chemical structure of a Pc molecule (here CuPc), b) π→π* transition, according to the calculations of Stillman et al. [79]

Pc molecules are used in this work for application in OSC and as model system to study formation of nanostructures by absorption of the molecule in thin film solution deposition methods, like spin casting and dip coating. The motivation of using these molecules is the diverse application of their thin films [6] especially in organic photovoltaics [80]. The word phthalocyanine is derived from greek word “naphtha” (rock oil) and “cyanine” (dark blue), see Figure 2-10a. Pc was discovered in 1907 by Braun and Tcherniac [81]. In 1929 the first patent on the Pc preparation was published by Dandridge, Drescher, and Thomas [82]. Since then Pc’s are used in science and technology for diverse applications. Metal Pcs have unique optical and electronic properties [23] and a high chemical and thermal stability [7]. They are used as organic semiconductors [8] with numerous applications such as OSCs [5, 9-11, 22, 80, 83], chemical sensors [12-14] and electronic devices like field effect transistors [16-18] and optical data storage [20, 84].

There are also many spectroscopic studies on Pc in vapor [85] in solid, [86], in solution [87] as well as theoretical studies on their spectroscopic properties [88]. Experimental and theoretical studies showed that the UV-Vis spectrum of metal Pcs is dominated by π-π* transitions in the strong Q-band (600nm-750nm) and the broad B-Band (300nm-450nm) [24, 89-91]. Gouterman et al. showed that to a first approximation the strong Q-band (600nm-750nm) is associated with transitions from a_{lu} to e_g* orbitals (π-π*). The broad B band is related to transitions between a_{2u} and b_{1u} to e_g* orbitals, see Figure 2-10b [85, 90-92].

Dissolved Pcs often show solvatochromic effects [32, 93-98]. Dimerization of Pc molecules in solution causes a (reversible) band shift [99]. The deformation of the Pc molecules due to interactions with the solvent changes the symmetry of the molecules and influences the absorption spectra, e.g. the splitting of absorption bands in case of D_{2h} to C_{2V} transitions [100].

2.5 Organic solar cells

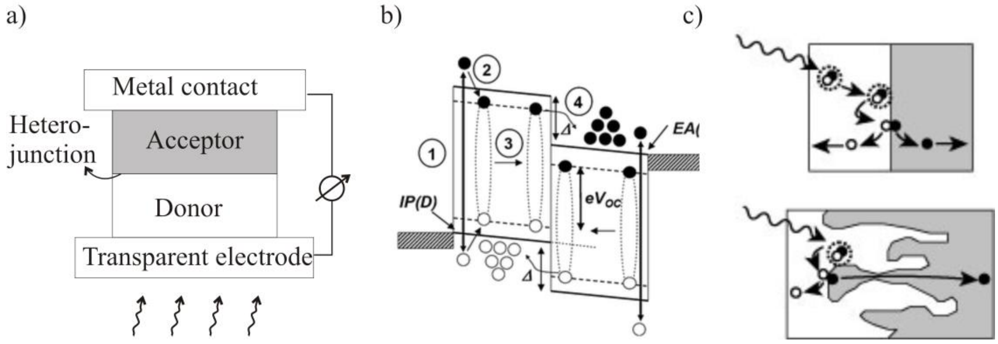

Figure 2-11 a) schematic of a heterojunction bilayer OSC b) band diagram of heterojunction bilayer OSC from[101], c) increasing the efficiency at the interface from [102]

OSCs are devices made of polymers or small molecules that convert light into electric current (photovoltaic effect). Heterojunction bilayer OSCs are made of an electron releasing (donor) layer and an electron accepting (acceptor) layer sandwiched between two conductive electrodes. One of the electrodes should be transparent to light, see Figure 2-11a. Up to now, heterojunction bilayer OSCs achieve higher efficiencies rather than single layer OSCs [103-105]. In OSC the absorption of photons (Figure 2-11b step 1 and 2) results in the creation of bound electron-holes pairs in the absorbing layer, called excitons. The excitons diffuse to the heterojunction (Figure 2-11b step 3) and dissociate to electrons and holes. Electrons transfer to the acceptor layer and holes to the donor layer (Figure 2-11b step 4). In Figure 2-11b, *IP(D)* denotes the HOMO energy level of the donor layer and *EA* the LUMO energy level of the acceptor layer. The difference between *IP(D)* and *EA* determines the open circuit voltage under illumination (V_{oc}) [101].

For an efficient OSC, the excitons should reach the heterojunction within the lifetime of the exciton (some nanoseconds) [102]. The transport of the exciton in the organic layer occurs by diffusion at a distance < 50 nm. One of the methods to collect the excitons efficiently and thus improve the OSC, is structuring the interface of the heterojunction. Here structuring means increasing the interfacial area in the range of the exciton diffusion length, e.g. by increasing the roughness of the interfacial area and formation of an interpenetrating donor–acceptor network [102] [106], see Figure 2-11c. One way to structure the interface is using the solution deposition method and controlling the parameters influencing the nucleation and growth from solution, such as solvent, temperature, and etc [107].

OSCs containing unsubstituted Pcs are typically prepared by high vacuum deposition because of their poor solubility [80, 108]. To use alternative, technologically simpler solution deposition, many research activities focused on synthesizing new soluble Pcs by adding chains or radicals to the Pc molecule [109-111]. For instance, recently Varatto et al. [112] used functionalized ZnPc to produce OSCs from solution (with a rather small power conversion efficiency of up to 0.12%). Schuhmann et al. [113] used substituted CuPc in OSCs with a power conversion efficiency of 0.3%. Unfortunately, most of the substituted Pcs are less stable than the unsubstituted compounds, and their electronic properties also differ [6, 35] [23]. In addition, chemical modification increases the material cost. Hence, it is desirable to prepare OSCs with reasonable efficiency from unsubstituted Pcs by solution deposition. Only recently, Sue et al. [38], and Komino et al. [40] prepared spin coated films of CuPc dissolved in TFA/chlorobenzene. Derouiche et al. blended CuPc and C60 (or PCBM) in dichlorobenzene and TFA mixture to prepare a bulk heterojunction [45, 114].

2.5.1 Current-Voltage characteristic measurements

The power conversion efficiency is the ratio between the electrical output of a solar cell abd the incident energy of sunlight. The electric current of a photovoltaic solar cell corresponds to the number of created charges that are collected at the electrodes. This number depends on the fraction of photons absorbed; the fraction of electron-hole pairs that are produced, and finally the fraction of charges reaching the electrodes [101] [26].

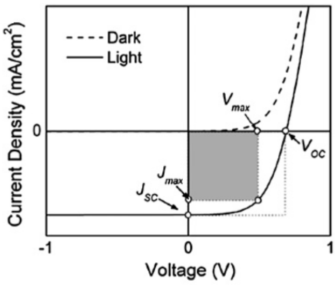

Figure 2-12) Typical I-V curve of a solar cell [101]

The power conversion efficiency (PCE) is determined by measuring the voltage-current characteristics of OSCs under illumination and once in dark. The solar cell behaves like a diode in an electric circuit under dark condition (no illumination). Under illumination charge carriers can drift in this electric field to the electrodes and the solar cell has a different potential on its electrodes. The electrodes of OSC have different Fermi levels, see Figure 2-12a. The electrons move to the metal with lower work function and the holes to the opposite electrode. The maximum voltage is called the open circuit voltage V_{OC}, which corresponds to the difference in the metals' work functions and balances the built-in field, see Figure 2-12 [26]. The maximum generated photocurrent flows under short-circuit conditions (J_{sc}). To calculate the PCE, the device parameters i.e., open circuit voltages (V_{oc}), short circuit currents (J_{sc}), and maximum power point ($J_{max} \times V_{max}$) are measured. The PCE, which is the most important metric of an OSC is defined as (P_{inc} : incident power density) [101]:

$$PCE = \frac{J_{max} \times V_{max}}{P_{inc}} \tag{2-19}$$

The fill factor is the ratio of the actual maximum power output of a solar cell to its theoretical output if both current and voltage were at their maximum pint (J_{sc}, V_{oc}). It represents the ideality of a solar cell, and is calculated as:

$$FF = \frac{J_{max} \times V_{max}}{J_{sc} \times V_{oc}} \tag{2-20}$$

3. Experimental Details

Chapter overview: In this chapter the experimental details are presented. First, materials and the general preparation methods are introduced. Detailed information on preparation of specific samples and measurements are introduced afterwards.

3.1 Methods

In this work mainly AFM is used to study morphology and coverage. Experimental methods and set up used in this thesis are explained in appendix-2. Below Tapping-mode AFM as the main method is introduced.

3.1.1 Atomic force microscopy (AFM)

In Atomic force microscopy (AFM) a flexible cantilever is used to probe the interaction between the sample and tip, see Figure 3-1. The tip, has a radius of curvature $\leq$10nm. The cantilever is a miniature spring with a length of 100-400 μm and a spring constant of some mN/m. During the measurement it is attracted or repelled mainly by van der Waals forces. The attractive or repulsive forces bend the cantilever. This deflection is detected using a laser beam reflected from the back of the cantilever into a photodetector. This laser spot moves in the photodetector, as the cantilever is deflected towards or away from the sample surface. The signal is calculated by comparing the signals from four quadrants of the detector [115], see Figure 3-1a. Regarding the distance between sample surface and tip (d), three different primary imaging modes are possible: contact mode ($d < 0.5$ nm), non-contact mode ($0.5 \text{ nm} < d < 10$ nm), and tapping mode ($d \sim 0.5$-2 nm), see Figure 3-1b. In contact mode, the tip scans the sample surface by being pushed against the surface. Contact mode is suitable for hard surfaces where the tip cannot damage the surface [116]. In non-contact mode the separation of tip and surface is so large, that the interaction between tip and sample-surface is small and mostly in the range of the damped forces in ambient conditions. Therefore non-contact mode is appropriate for measurement mostly under vacuum [117], and even sub-molecular resolution can be achieved [118].

In tapping mode, the cantilever oscillates and the tip taps the surface slightly during scanning, see Figure 3-1b. Thus the surface is damaged less than in contact mode while the lateral forces are eliminated. The cantilever oscillates near its resonance frequency. The interaction between sample and tip influences the amplitude and phase. The oscillation is monitored by a feedback loop and the height of the cantilever will be adjusted accordingly to measure the changes in the surface of the sample [119].

In the following I use tapping mode for measuring the morphology of thin films of organic molecules, which allows a higher resolution than non-contact mode. Furthermore the tapping mode does not destroy the organic layers as in contact mode, see Appendix 5.

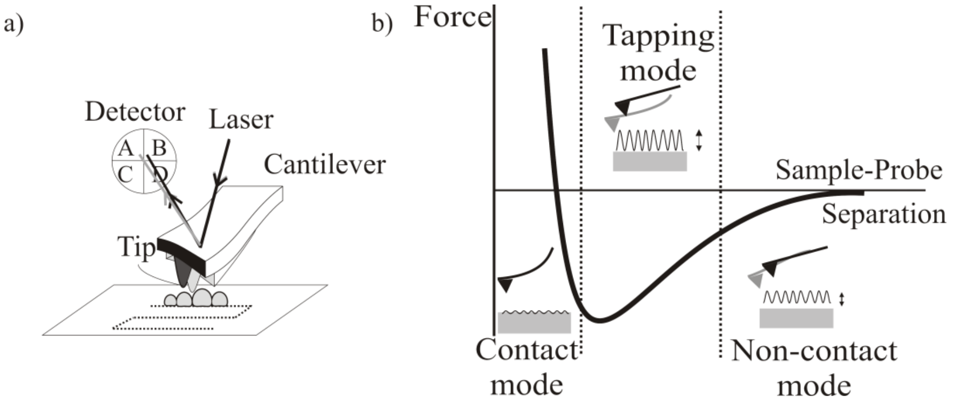

Figure 3-1 a) Schematic drawing of AFM measurement, b) the force curve of interaction between tip (probe) and sample surface.

Radius of the curvature of the tip: The tip radius has a significant influence on the lateral resolution and the size of the measured features, see Figure 3-2. Considering the relation between the tip radius (R) and the feature's radius (r), there are three general cases possible: R > r, R ~ r and R < r. If the tip radius is much smaller than the feature's radius, the measured width depends on the shape of the tip, especially on the conical angle of the tip, see Figure 3-2a [120]. When the tip radius and the feature radius are of the same size the measured width is a sum of the tip and feature width. To a first approximation calculations are available for measured height (H) assuming the geometry of Figure 3-2b:

$$H = r\left[1 - \sqrt{\frac{r_c^2}{(R+r)^2}}\right] \tag{3-1}$$

The width of a feature is estimated as (h: height of the feature) [121]:

$$W = \sqrt{8Rh} \tag{3-2}$$

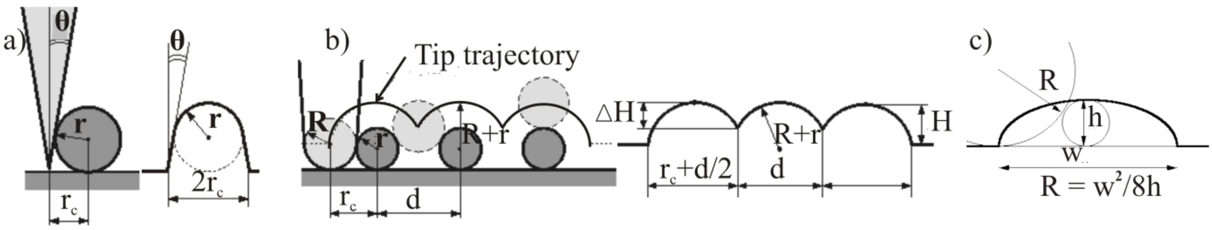

Figure 3-2 Schematics of a) curvature radius of the tip (R) smaller than studied feature radius (r), b) R ≈ r, c) lateral resolution of AFM, images from [120, 121].

When the tip radius is much larger than the feature’s size, obviously the measurement resolution is not sufficient to detect the real size of the features. With the equation (3-2) the measured size of a feature can be estimated to first approximation. Consider we measure a spherical feature with a diameter of 1 nm using tips of various radii: 10 nm, 2 nm, and 1 nm. The measured size of the same feature for each tip radius is, respectively: ~ 10 nm, ~ 4 nm, and ~ 3 nm.

Tip-sample interaction: The resolution of AFM images is also influenced by the environmental conditions. E.g. the sample surfaces can be covered with a layer of adsorbed gases such as water vapor, oxygen, dioxide carbon etc., which impacts the measurement. For the water layer, the humidity plays an important role. A hydrophilic substrate exposed to ambient atmosphere can be covered with a thin film of liquid water. The liquid water film covers both tip and sample surface. It is reported that when tip and sample are in contact, the water in the overlapping region is displaced and accumulated at the edge of the contact area and forms a meniscus when the tip is retracted [122]. During an oscillation of the AFM tip, the shape of the meniscus changes permanently and influences the measurement. Further influences arise from sample-tip interactions. Sticky substances or very loosely bound materials can be attracted to the tip by a very gentle contact of the tip and sample in oscillation intervals of the tapping mode. This effect can change the tip radius slightly even in the first approach [123], thus giving features with larger size than expected.

Device: For AFM measurements different devices were used: Veeco multimode and dimension and JPK Nanowizard 3. Tapping mode-tips (NCHR type) with ~ 10 nm radius of curvature and (NCRW type) with ~ 2 nm radius of curvature and resonance frequency of 320 kHz were purchased from Nano World. For high resolution AFM measurement tips with 1 nm radius of curvature and resonance frequency of 150 kHz from Budget Sensors were used. All measurements were performed in ambient atmosphere.

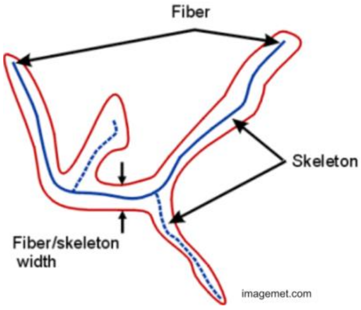

Figure 3-3) Schematic drawing of fiber analysis in SPIP software, image from [124].

Analysis: For the evaluation of the AFM data SPIP 6.0.1 software was used. Using pore and fiber analysis in SPIP, the number of fibers, width of fibers and coverage in each AFM image were Figured out. Especially fiber's width and length in SPIP are estimated by the area of the shape divided by the fiber length, which is the mean width perpendicular to the fiber. For measuring the length the skeleton of a polygon shape fiber is estimated by thinning the shape into a one pixel wide branched line. The skeleton length is the sum of the length of all branches (or segments) of the skeleton, see Figure 3-3 [124]. However it is not possible using this software to distinguish the fibril structure. At coverages where the fibril structure is not pronounced clearly, the measured values are not correct and have to be measured per hand. The number of nodes per area is counted manually because no appropriate software was found.

3.1.2 Ultra Violet-Visible spectrophotometry (UV-Vis)

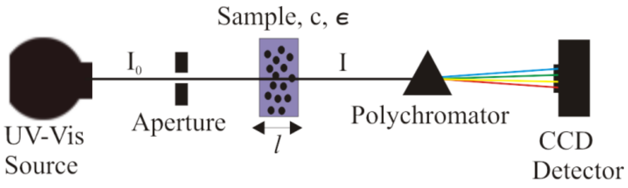

Figure 3-4) Schematic drawing of UV-Vis spectrometer

The absorption spectroscopy measurements were performed with an Agilent 8453 spectrophotometer. The light sources of the spectrophotometer were a deuterium and a halogen lamp. The combination of dispersion and spectral imaging is accomplished by using a concave holographic grating. The grating disperses the light onto the diode array (detector) at an angle proportional to the wavelength. A schematic drawing of the UV-Vis spectrometer is shown in Figure 3-4.

Thin films were prepared by spin casting the solution onto a glass substrate. A quartz cuvette from Starna Scientific (England) was used for UV-Vis measurements of solutions. The light paths of the cuvettes were chosen as 1, 0.1 or 0.01 cm, respectively, to optimize the absorption range for the measurement. The cleaning procedure is similar to that for SiO_2 wafers.

3.2 Materials

Unsubstituted metal Pc: In this thesis unsubstituted metal Pc were used 1) to prepare a solution to be used in for deposition from solution, 2) to produce a thin film from solution with application in OSC and 3) to study the formation of such a film from solution: CuPc (> 99%) and ZnPc (> 99%) were kindly supplied by Minakem Leuna. The other Pcs, MgPc (90%), MnPc (90%), CoPc (> 97%), FePc (90 %), NiPc (85%), and SnPc (97%), were purchased from Sigma Aldrich.

Other materials: For OSCs, the following materials were used in high vacuum vapor deposition: C_{60} (> 99.9%) from MER, bathocuproine (BCP, ~97%) from Fluka and Aluminum (99.999%) from Alfa Aesar.

The solvents, listed in table 1-1, are used as supplied without further treatments.

Table 3-1: List of the solvents and their supplier

	Solvents	Abbreviation	Purity (%)	Density $Kg \cdot m^{-3}$	Supplier
	Acids:				
1.	Acetic acids	AcOH	99.8	1048	Fisher Scientific
2.	Formic acid	FA	99.5	1220	Fisher Scientific
3.	Phosphoric acid	PA	99	1680	Fisher Scientific
4.	Sulfuric acid	SA	99.99	1840	Sigma-Aldrich
5.	Trifluoroacetic acid	TFA	99	1535	Acros Organics
	Ionic liquids:				
6.	1-Ethyl-3-methylimidazoliumacetate	STOR	90	1027	BASF
7.	1-Ethyl-3-methylimidazoliumethyl sulfate	EMIM	99	1024	Iolitec
	Standard solvents:				
8.	Acetone		99.5	790	J.T.Baker
9.	Acetonitrile	ACN	99.95	786	Merk
10.	Anisole		99	995	SAFC
11.	Benzene		99.5	880	Roth
12.	Chlorbenzene	CBZ	99.8	1106	Sigma-Aldrich
13.	Chloroform	TCM	99.5	1490	Chemsolute
14.	Decanol		98	825	Alfa Aesar
15.	Dichloromethane	DCM	99.8	1330	VWR
16.	Dioxane		99	1034	Acros Organics
17.	Dimethylacetamide	DMAC	99.97	940	Fisher Scientific
18.	Dimethylformamide	DMF	99	994	AppliChem
19.	1,3-Dimethyl-3,4,5,6-tetrahydro-2(1H)-pyrimidi7none (DMPU)	DMPU	98	1060	Alfa Aesar
20.	Dimethyl sulfoxide	DMSO	99.9	1100	Merck
21.	Ethanol	EtOH	99.8	790	VWR

22.	Ethyl acetate	EtOAc	99.5	900	Chem solute
23.	Isopropanol	IPA	99.7	785	Chem solute
24.	Methanol	MeOH	99.8	790	J.T.Baker
25.	N-Methyl-2-pyrrolidone	NMP	99.8	1026	Roth
26.	Tetrahydrofuran	THF	99.9	890	Sigma-Aldrich
27.	Toluene		99	866	Acros Organics

Substrate

SiO_2: SiO_2 provides an amorphous surface with a very low roughness (<1 nm). It was used as a model substrate to study the formation of the thin film in solution deposition. Silicon wafers with artificially grown oxide layers of ~300 nm thickness (SiO_2 substrates) were purchased from Silchem (Freiberg, Germany).

The cleaning procedure, the purity and the age of the wafer influence the surface property of the silica wafers. Wafers with metal contamination or old wafers have different properties and can produce different results [125, 126].

The SiO_2 substrates were cleaned with acetone and ethanol in an ultrasonic bath, with 10 min for each solvent separately. Then they were rinsed several times with deionized water. Afterwards they were submerged into a piranha solution (hydrogen peroxide and sulfuric acid, mixing ratio 1 to 2) for 30 min and finally washed 10 times with deionized water and 10 min with deionized water in ultrasonic bath.

ITO: indium tin oxide (ITO) is used in OSCs as a conductive transparent electrode on a glass substrate. However the high roughness (> 2 nm) and structured surface of ITO makes it improper as a model substrate to study nucleation and growth.

Glass substrates coated with different film of ITO (~ 15 nm ITO, roughness of ~ 2nm, and resistance of 500 Ω/sq; ~ 300 nm ITO, roughness of > 2nm, and resistance of 5 Ω/sq) were obtained from PGO (Iserlohn-Germany). The ITO substrates were cleaned by submerging them into acetone and ethanol in ultrasonic baths, in each solvent for 20 min. Finally they were rinsed thoroughly with deionized water.

ITO for OSC: for OSC substrates (ITO, 300 nm) with a sheet resistance of 5 Ω/sq were used. For the preparation of OSCs, ITO substrates of the size 13 × 24 mm were structured with laser in Helmholtz Zentrum Berlin, so that the front and back electrode in the OSC are isolated.

Glass: Glass substrates from Carl-Roth (Germany) for UV-Vis measurement were cleaned as SiO_2 substrates.

3.3 Sample preparation and measurement protocol

3.3.1 Solubility measurement protocol

Solution preparation for solubility study: First a stock solution of each Pc was prepared. From this 3 to 4 diluted solutions were derived. Acid solutions were prepared by shaking (20 min with 500 mot/min). Metal Pc molecules can be dissolved in many acids and usually interact with acids. This interaction can lead to protonation of metal Pc. This will be discussed later in each case. The solutions with conventional liquids and with ionic liquids were prepared by sonication (10 min) at room temperature.

Solubility measurement protocol: Two measurement protocols are used:

1. The molar absorption coefficients were derived from the relation between the absorption intensity and the concentration of the metal Pc.
2. The saturation concentrations were derived from the absorption intensities of saturated solutions using the molar absorption coefficients. If available, molar absorption coefficients were determined by the measurements according to protocol 1. If the solubility was too low to reliably measure a precise molar absorption coefficient in the applied solvent, a mean value of the measured molar absorption coefficients of similar kind of solvents and with similar spectra was used.

Molar absorption coefficient measurements: For the molar absorption coefficient measurements only the following selection of solvents were used:

Acids: SA and TFA

Ionic liquids: STOR

Conventional solvents: DMAC, DMF, DMPU, DMSO, NMP

For the other solvents from Table 3-1 the solubility was typically too low to obtain quantitative concentration data or their solvatochromic/chemical effects were too strong. They were not used for the molar absorption coefficient studies.

The main uncertainty in the concentration data (estimated > 10%) originates from the weighing errors of the low sample weights because of the typically rather low solubilities.

Saturation concentration measurements: An amount of metal Pc exceeding the maximum solubility (i.e., leading to the precipitation of undissolved Pcs) was introduced into the various solvents to obtain saturated solutions.

After typically 20-30 minutes the saturated solutions were separated from the undissolved Pc by centrifugation at room temperature for 10 min at 25.000g. FA solutions were centrifuged at 0 °C to reduce the catalytic decomposition of acid [127, 128]. The spectroscopic measurements with the clear supernatants were performed immediately after the centrifugation.

The dispersion of the solid Pc particles in the rather viscous ionic liquids takes longer than only a few minutes. Typically after 24 hours the solution reached its maximum concentration. The ionic liquid solutions were shaken per hand occasionally and finally centrifuged one day after preparation.

3.3.2 Solution based deposited thin films

Solution preparation for CuPc thin film deposition: First a stock solution of CuPc in TFA with a concentration of 1.7×10^{-3} mol·L^{-1} (near saturation solution) was prepared by stirring the solution with a magnetic stirrer for 3 hours. From this 3 to 4 diluted solutions were prepared.

Spin casting: A drop of the solution is placed onto the rotating substrate. The solution spreads on the substrate and after evaporation of the solvent a thin dry film remains. Spin coater SCI and SCE (NOVOCONTROL Technologies GmbH) devices were used. Because TFA as a corrosive solvent turned out to be aggressive for spin coaters, the coating was performed under a hood. The rotating speed is given as round per second (rps).

Dip coating: The substrates are immerged into the solution and drawn out with a given speed. After solvent evaporation a thin film remains on the substrate. Dip coating is done with a home-made device. The device was built with an electric motor connected to a controller for setting up the speed, tweezers to hold the substrate and a closed box in which substrate and solution are placed. Dip coating is performed in the box, so that the environmental air fluctuations have less impact on film formation.

Drop casting: Drop casting is technically the simplest way of deposition from solution. The solid film is not homogenous in comparison with spin casting and dip coating. But the film is thicker, because the thickness of the film is not limited by centrifugal or gravitational force. The film formation is complicated and influenced by the evaporation and Marangoni effect [129]. Drop casting was used to bring more material onto the substrate for measurements where the material properties of the film were studied, like XRD or FT-IR spectroscopy.

The substrates for sample preparation are used immediately after cleaning. After preparation the samples were stored in a closed plastic box.

3.3.3 X-ray diffraction measurement

XPRD: To investigate the crystallographic structure of CuPc after dissolution in TFA and evaporation of the solvent, a thick film is scratched very carefully, the product is gathered and X-ray powder diffraction of the product is measured. Later this powder was heated to 200°C under vacuum for 30 min to remove any residual solvent residuals. The crystal structures before and after dissolution in TFA and after heating were analyzed.

Furthermore, XRD was performed on a drop casted film, once after preparation and once after heating up to 200°C for 30 min. The X-ray diffraction method is explained in appendix-1.

Analysis: The measured diffraction patterns were compared data from the data bank of the International Centre for Diffraction Data (ICDD) and also other published XRDPs on CuPc which are not in the ICDD data bank [130]. To compare the diffraction patterns precisely, the patterns of α-CuPc from the Crystallography Open Database (COD) were simulated based on the Hoshino et al. studies [131], using the molecular and crystal structure visualization software "Diamond" version 3.1f. The simulated patterns were compared with the measurements to track the crystal structure and lattice parameters of CuPc deposited from TFA solution by evaporation of solvent.

Device: a D8 Diffractometer (Bruker-Germany) is used for the diffraction measurements.

3.3.4 SEM and TEM

SEM samples were prepared by drop casting the solution onto the SiO2 substrate.

For TEM measurements a drop of the solution was places on the TEM grid and dried.

Cryo-TEM measurements were obtained at FU-Berlin by Dr. Böttcher. For the measurement a thin film of the liquid CuPc/TFA solution was placed on the TEM-grid and undercooled spontaneously. The frozen liquid film was investigated using transmission electron microscopy at liquid nitrogen temperature.

Further information on the measurement set up is presented in appendix 1.

3.3.5 FT-IR and UV-Vis spectroscopy of thin films

FT-IR samples were prepared by drop casting the solution (1.7×10^{-3} mol·L^{-1}) onto the SiO_2 substrate.

UV-Vis samples were prepared by spin casting the same solution at 35 rps. The samples were measured once after evaporation of the solvent and once after heating them to 200°C under vacuum for 30 min. The FT-IR measurement setup is described in appendix 1.

3.4 OSC preparation

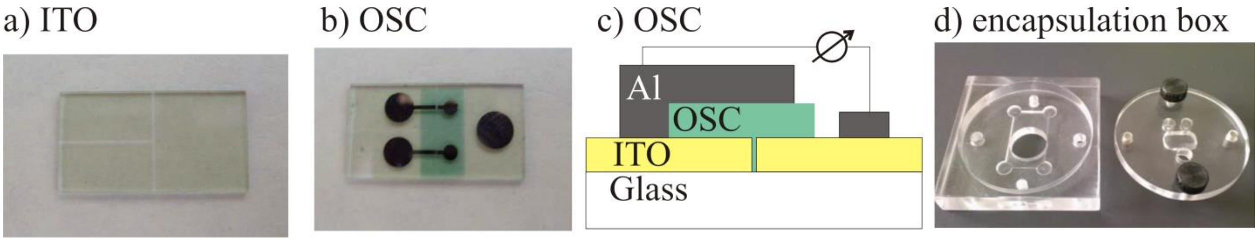

Figure 3-5 a) Photograph of ITO substrate, b) photograph of OSC, c) schematic drawing of OSC, d) photograph of encapsulation box.

OSCs based on a combination of solution and vacuum processing were fabricated as follows: Layers of different CuPc coverages were prepared on ITO by solution processing with single or multiple drop spin casting (each drop is added after the film is dried) under ambient conditions (room temperature, ambient atmosphere). The spin casting of OSC film is explained in detail in chapter 8. Then the samples were heated for 30 min at 200°C under vacuum to remove the residual solvent. Upon these samples, via vacuum vapor deposition, a 30 nm layer of C60 as acceptor (~0.07 nm/s), a 10 nm thick BCP buffer (~0.03 nm/s) as hole-blocking layer [48, 132] and finally a 100 nm thick Aluminium back contact (~0.15 nm/s) were deposited (For high vacuum evaporation set up see appendix 1), see Figure 3-5a for ITO substrate, 3-5b for OSC, and 3-5c for schematic of the OSC. Directly after the preparation the devices were encapsulated (under inert gas) to avoid degradation induced by the ambient humidity and oxygen, see Figure 3-5d.

PCE measurement: The photovoltaic properties of the OSC are measured using a commercial sun simulator at the Helmholtz Zentrum-Berlin. In the sun simulator, the OSCs are illuminated by a xenon and halogen lamp; which gives a spectrum similar. After encapsulation, the cells were taken out of the glove box and were transported to the sun simulator with a commercial source (1.5 AM, 100 mW·cm^{-2}, 25°C). A voltage is applied between 1 V and -1 V in 0.025 V steps to the cell, and the current is measured.

4. Solubility of Unsubstituted Metal Phthalocyanines

Chapter overview: For deposition of a thin film from solution, information on the solubility of unsubstituted metal Pc is needed. Unfortunately there are no studies on the solubility of unsubstituted Metal Pcs. The generally poor solubility of unsubstituted metal Pcs limits their use in low cost solution deposition technologies. Usually high vacuum deposition techniques are used to deposit thin films of unsubstituted metal Pcs or the molecules are chemically functionalized to be soluble. Both methods are technically complicated and increase the cost of the material [6, 36] [34] [35]. Furthermore chemical functionalization changes the performance of Pcs in OSC [33].

In the following a systematic study on the solubility of unsubstituted metal Pcs is presented. The solubility and stability of the molecules are investigated in various neutral conventional solvents, acids, and ionic liquids. The aim of the study is a systematic quantitative assessment of the solubility of various unsubstituted metal Pcs, their saturation solubilities and their interactions with the solvents.

These results are published in “Journal of Chemical & Engineering Data” [133].

4.1 Solubility measurement

The molar absorption coefficients and saturation concentrations were determined spectroscopically via the Lambert-Beer law assuming a linear relationship between the absorbance, A_λ, the molar absorption coefficient, ε_λ, of the absorbing species at the wavelength λ, the concentration, c, and the light path, l:

$$A_\lambda = \epsilon_\lambda c\, l \tag{4-1}$$

For the solubility studies, the absorbance of the Q band was used to measure the solute concentration. Although the position of the absorption bands and their shape can be solvent dependent, their relative positions remain roughly constant [134] and usually the absorption coefficient does not vary drastically [135]. According to Stillman et al. the high energy B band represents mostly the charge transfer transitions [130, 136-139]. The less solvatochromic Q band is in most cases well separated from its neighboring bands and there is no vibronic mixing between the Q band and the higher lying states [93]. The influence of the vibronic transitions near the Q band was neglected, since in most cases they were much smaller than the Q bands. In cases, in which more than one intensive Q band exists (Q band splitting), only the molar absorption coefficient of the stronger transition as a measure for the solubility is taken. To a rough approximation, the molar absorption coefficient of the Q band is in the range of 10^5 $L \cdot mol^{-1} \cdot cm^{-1}$ [46]. Dimerization may change the molar absorption coefficient of the Q band slightly, e.g., from 2.5×10^5 $L \cdot mol^{-1} \cdot cm^{-1}$ (monomer) to 2.2×10^5 $L \cdot mol^{-1} \cdot cm^{-1}$ (dimer) as shown by Hush et al. [140]. The measurements show that depending on the central metal atom the molar absorption coefficient may change by up to one order of magnitude, whereas solvent effects cause only smaller variations.

4.2 Determination of the molar absorption coefficients

The molar absorption coefficients were determined from the slope of the absorption intensity of the Q band versus the amount-of-substance concentration (as an example see Figure 4-1). For this protocol the maximum solubility had to be sufficiently high and the solution had to be sufficiently stable. Then the coefficients could be derived with sufficient certainty (typically ±10%). However, sufficiently high solubility was not given for many of the conventional solvents and some of the ionic solvents. Some of the acidic solutions were not sufficiently stable. In these cases no molar absorption coefficient is presented (Table 4-1).

For the spectroscopic determination of the saturation concentration a molar absorption coefficient is needed. In those cases where a reliable value could not be derived from the concentration-dependent absorptivity due to low solubility, a mean molar absorption coefficient is derived. This mean coefficient is the averaged value of the molar coefficients of solutions of the same Pc dissolved in comparable solvents with sufficiently high concentration and with very similar spectra.

Only in the case of SnPc and NiPc, the mean molar absorption coefficients for conventional solvents have to be derived from acidic solutions, because there were no conventional solvents of sufficient solubility.

Table 4-1: Molar absorption coefficient of metal Pcs derived from the intensities of the Q band*

Solvents	CoPc	CuPc	FePc	MgPc	MnPc	NiPc	SnPc	ZnPc
Acids:								
SA	1.5	1.6	0.34	1.2	0.5	1.7	0.6	2.4
TFA	1.3	1.3	0.18	1.1	‡	4.2	1	1.4
Ionic liquids:								
STOR	†	†	0.47	3.7	†	†	†	3.1
Conventional solvents:								
DMAC	0.8	†	0.12	2.4	0.18	†	†	2
DMF	1.1	†	0.26	2.1	0.28	†	†	2.7
DMPU	1.8	†	0.5	2.7	0.18	†	†	2
DMSO	†	†	0.1	1.7	0.38	†	†	2.1
NMP	1.3	†	0.1	1.8	0.11	†	†	1.6
From literature:								
DMF [87]		0.16	0.23		2.3			4.00
DMSO [93]	1.2		7.6			1.5		2.9
Glass [86, 141]	1.20	5.60	1.60		3.50	4.00		1.60
Doped glass [142]	3.8	4.00	2.50		1.50	1.60		1.70
Polymer [143]		3.00						2.00

* The unit is (10^5 L·mol^{-1}·cm^{-1}). The error in the absorption coefficient is estimated to be ± 10 % of the reported values.

‡ Due to strong spectral changes, the mean absorption coefficient was used.

† Due to low solubility (concentration <10^{-4} mol·kg^{-1}), the mean absorption coefficient was used.

Table 4-2: Maximum concentration, c_{max}*

Solvents	CoPc	CuPc	FePc	MgPc	MnPc	NiPc	SnPc	ZnPc
Acids:								
FA	5.75×10^{-6}	†	3.1×10^{-5}	1.63×10^{-3}	‡	6.36×10^{-4}	2.96×10^{-5}	3.02×10^{-1}
PA	‡	†	1.73×10^{-5}	‡	‡	†	†	†
TFA	8.63×10^{-4}	2×10^{-3}	2.94×10^{-3}	5.52×10^{-4}	‡	3.2×10^{-4}	7.43×10^{-4}	2.19×10^{-3}
Ionic liquids:								
STOR	1.91×10^{-6}	4.71×10^{-7}	3.61×10^{-4}	1.06×10^{-4}	†	1.25×10^{-4}	2.02×10^{-6}	9.19×10^{-4}
EMIM	8.53×10^{-7}	†	4.32×10^{-4}	1.75×10^{-4}	6.64×10^{-3}	†	†	3.1×10^{-5}
Conventional solvents:								
Acetone	†	†	†	†	1.01×10^{-4}	†	†	†
CAN	5.22×10^{-7}	†	5.09×10^{-6}	2.76×10^{-4}	6.81×10^{-6}	†	†	3.65×10^{-6}
Anisole	1.75×10^{-6}	4.57×10^{-7}	1.01×10^{-5}	1.05×10^{-4}	7.32×10^{-4}	1.23×10^{-6}	8.36×10^{-6}	2.8×10^{-6}
Benzene	†	2.61×10^{-7}	‡	3.91×10^{-6}	6.85×10^{-5}	†	4.86×10^{-7}	†
CBZ	1.14×10^{-7}	3.74×10^{-7}	1.56×10^{-5}		6.39×10^{-4}	2.9×10^{-4}	1.41×10^{-5}	†
TCM	†	†	†	†	†	†	2.26×10^{-5}	†
Decanol	†	†	2.68×10^{-5}	1.9×10^{-4}	1.32×10^{-4}	†	†	5.33×10^{-5}
DCM	†	†	5.95×10^{-6}	1.32×10^{-5}	6.28×10^{-3}	4.31×10^{-4}	2.57×10^{-5}	†
Dioxane	3.92×10^{-5}	4.42×10^{-7}	4.76×10^{-6}	5.63×10^{-4}	2.47×10^{-3}	†	2.05×10^{-6}	1.27×10^{-4}
DMAC	4.03×10^{-5}	†	3.21×10^{-4}	3.12×10^{-4}	7.47×10^{-3}	†	7.53×10^{-6}	9.96×10^{-4}
DMF	2.06×10^{-4}	†	2.71×10^{-4}	1.7×10^{-4}	8.24×10^{-3}	†	8.73×10^{-6}	†
DMPU	6.47×10^{-4}	3.75×10^{-6}	6.05×10^{-4}	7.35×10^{-4}	5.99×10^{-3}	7.26×10^{-4}	1.27×10^{-6}	5.59×10^{-3}
DMSO	3.32×10^{-5}	†	1.94×10^{-4}	2.63×10^{-4}	1.97×10^{-3}	†	5.6×10^{-6}	5.58×10^{-4}
EtOH	3.46×10^{-7}	†	1.01×10^{-5}	4.29×10^{-5}	1.92×10^{-3}	†	†	2.38×10^{-6}
EtOAc	†	†	†	2.38×10^{-5}	2.99×10^{-5}	†	†	†
IPA	†	†	†	7.67×10^{-6}	1.43×10^{-4}	†	†	1.53×10^{-6}
MeOH	1.33×10^{-7}	†	1.05×10^{-5}	7.48×10^{-7}	1.84×10^{-3}	†	2.38×10^{-7}	1.23×10^{-6}
NMP	‡	5.36×10^{-7}	2.85×10^{-4}	5.48×10^{-3}	3.45×10^{-4}	†	5.15×10^{-7}	6.92×10^{-3}
THF	9.87×10^{-5}	9.1×10^{-6}	1.25×10^{-5}	6.48×10^{-3}	6.62×10^{-3}	1.43×10^{-6}	2.9×10^{-6}	7.97×10^{-4}
Toluene	8.3×10^{-8}	3.25×10^{-7}	7.15×10^{-7}	2.75×10^{-6}	6.03×10^{-5}	5.63×10^{-7}	1×10^{-6}	†

* The unit is molality (mol·kg-1). The uncertainty in the amount of MPc maximum concentration is estimated to be ± 50% of the reported values.

‡ Due to strong spectral change, the value could not be measured accurately.

† Due to Low solubility (concentration <10-8 mol·kg-1) and low absorption (<0.05), the value could not be measured accurately.

4.3 Determination of the concentration of the saturated solutions

With the help of the molar absorption coefficients, the maximum (saturation) concentrations, c_{max}, were determined from the measured saturation absorbance, $A_{(max)\lambda}$, of the Q bands, see Figure 4-1.

If a molar absorption coefficient could not be determined for the individual Pc-solution, a mean molar absorption coefficient is used. The detailed results on the maximum concentration of metal Pcs, c_{max}, in different solvents are listed in Table 4-2.

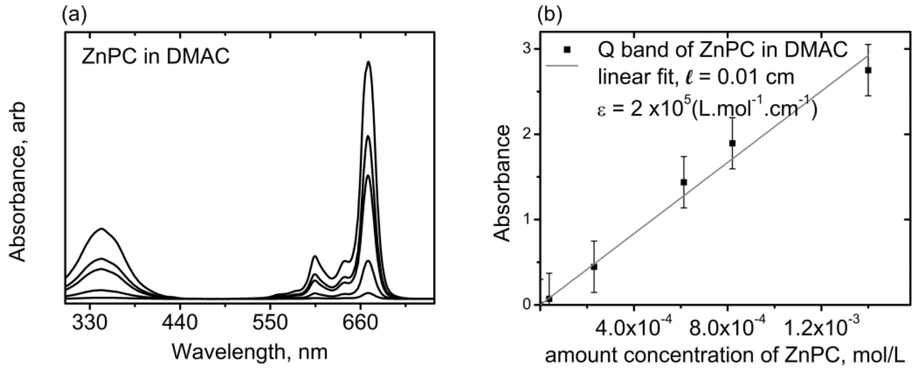

Figure 4-1 a) Absorption spectra of ZnPc in DMAC for different concentrations; b) Absorption intensity of the Q-band versus the concentration of ZnPc; the slope of the line yields the molar absorption coefficient.

Before presenting the results for the individual Pc solutions in detail, here are first a few, more general remarks:

- Metal Pcs dissolve quite well in SA. The saturation concentration in SA is reported to be 1 mol·kg^{-1}. It is also known that at high concentrations the metal atom can be removed from the Pc molecules. This decomposition of metal Pc is time, concentration and temperature dependent [144-147]. SA solutions are not stable. Accordingly, no spectra of Pcs in SA are presented.
- TFA and FA almost tend to alter the spectra of the Pcs compared to those obtained for conventional solvents. Ellis et al. suggested that TFA protonates all four nitrogen atoms in the porphyrin section [148]. Studies of Ledson et al. show that in Pc just the outer bridge nitrogen atoms are protonated [134]. Ledson et al. discuss, that the outer nitrogen may

play a role and the molecule can be slightly deformed [134]. Through the protonation of the Pcs new energy bands become active, and the absorption band shifts. Obviously the acidity of solvents affects the spectra, as can be seen also from the spectral modifications in the case of EMIM, the more acidic ionic solvent, compared to STOR, see following measurements for ZnPc and MgPc.

- FA can be decomposed catalytically by Pcs (HCOOH → H2O + CO2). Hanke et al. studied the activation energy for the catalytic decomposition of FA in the presence of a metal Pc and at different temperatures [128, 149, 150]. To minimize this reaction cold FA (~0°C) is used for this study. Even cooling the solution was often not sufficient to avoid decomposition. In several cases no saturation concentration could be determined.
- The average error, estimated for the maximum concentration, originates mainly from errors in the mean molar absorption coefficients. In addition, the equilibrium concentration might in some cases not have been reached due to the solubility kinetics or decomposition, etc. Based on this an error of up to ±50% of the presented values was assumed for saturation concentrations to provide a very conservative estimate.

4.4 The saturation concentration results

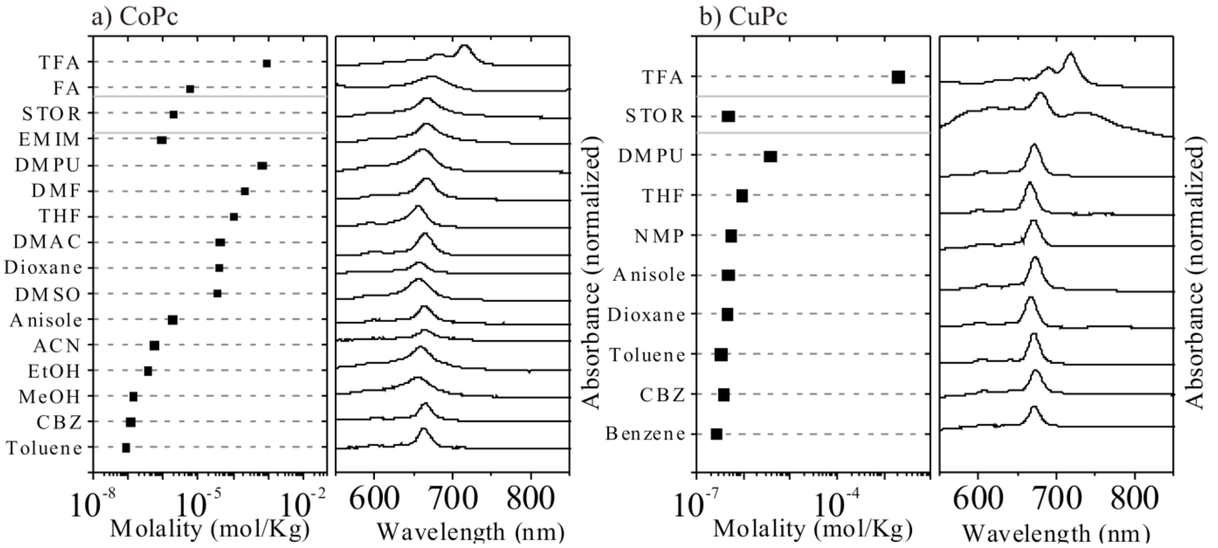

Figure 4-2 a) Maximum concentration of CoPc in different solvents (left) and their corresponding normalized Q-band absorption spectra (right); b) Maximum concentration of CuPc in different solvents (left) and their corresponding normalized Q-band absorption spectra (right)

4.4.1 CoPc

CoPc dissolves with measurable amounts in many of the conventional standard solvents, in acids, and in ionic liquids (see Figure 4-2a). The typical Q bands remain relatively unaltered in conventional solvents and in ionic liquids. In acids, the spectra are shifted and broadened. The spectrum of CoPc in TFA shows the typical protonation band of the Q band [97]. The unpaired electron of the cobalt in Pc can interact with solvents and also oxygen [151, 152]. This interaction leads to shifts of the absorption bands.

The molar absorption coefficient could not be measured accurately in ionic liquids and also in some of the conventional solvents due to the low solubility. The estimation of the concentration in these cases is based on a mean value of the measured molar absorption coefficients ($(1.3 \pm 0.7) \times 10^5\ \mathrm{L \cdot mol^{-1} \cdot cm^{-1}}$). CoPc solutions are not long-term stable. Solution preparations and measurements should be done within less than a five hours.

4.4.2 CuPc

CuPc is hardly soluble in any of the tested solvents (Figure 4-2b). The spectra of CuPc dissolved in conventional solvents show the typical, “normal” Q band. CuPc only dissolves in one of the ionic liquids, STOR, albeit with very low concentration and with a somewhat distorted spectrum. CuPc dissolves with high concentrations only in TFA, where it becomes protonated and new bands appear in the absorption spectrum [39, 153].

Due to the low solubility ($< 10^{-4}\ \mathrm{mol \cdot Kg^{-1}}$), the molar absorption coefficients of CuPc in conventional solvents and in ionic liquids could not be measured individually. For estimating the concentrations the molar absorption coefficient ($(1.4 \pm 0.7) \times 10^5\ \mathrm{L \cdot mol^{-1} \cdot cm^{-1}}$) was derived from TFA solutions. CuPc is quite stable (four weeks) in the solutions.

4.4.3 FePc

FePc dissolves at reasonable concentrations in many of the tested solvents. However, some spectra, including even those from some standard solvents show shifts, broadening and band splittings (Figure 4-3a). The low saturation concentrations ($<10^{-4}\ \mathrm{mol \cdot kg^{-1}}$) are derived with a mean molar absorption coefficient ($(2.7 \pm 1.4) \times 10^4\ \mathrm{L \cdot mol^{-1} \cdot cm^{-1}}$).

FePc solutions are not chemically stable (less than 4 hours). The metal center of FePc can be oxidized easily when interacting with solvents [154]. As a result the absorption band broadens/changes [154-156]. According to Minor et al. increasing the oxidation state of the central metal changes the Q band and different FePc species are produced in the solution [92]. This instability of FePc can be followed easily by visual inspection of the solvent as pronounced color changes. In TFA this color change occurs within one hour. Notably this effect is time and temperature dependent.

Additionally, FePc tends to dimerize at high concentration in solvents like NMP, DMF and DMSO. This dimerization results in a shift and broadening of the absorption band. In NMP and DMF the interaction of the nearly parallel Pc rings in the dimers causes a splitting of the monomer transition and the generation of new transitions [99].

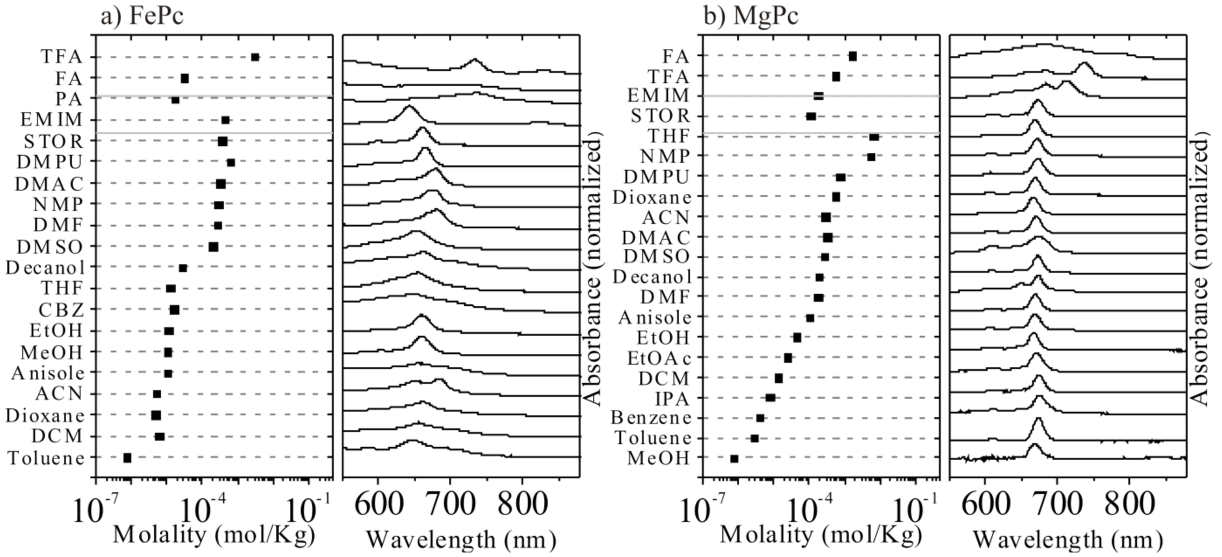

Figure 4-3 a) Maximum concentration of FePc in different solvents (left) and their corresponding normalized Q-band absorption spectra (right); b) Maximum concentration of MgPc in different solvents (left) and their corresponding normalized Q-band absorption spectra (right).

4.4.4 MgPc

MgPc is the most soluble Pc (Figure 4-3b). Most of the standard solutions have a regular Q band at 670 nm. In the ionic liquid EMIM, the absorption bands are red-shifted and split. These shifts and spectra modifications are even more pronounced in acid solutions due to the protonation of MgPc leading to symmetry changes of the molecule [157-159].

MgPc dissolves in FA at rather high concentrations (more than 10^{-3} mol·kg^{-1}), giving a dark blue liquid. The broadened absorption band is a sign of activation of several transitions near the Q band. FA decomposes in the presence of MgPc [128, 160]. Therefore, the maximum concentration presented has to be regarded carefully.

For solvents where the solubility is low, a mean molar absorption coefficient ($(2.1 \pm 1.6) \times 10^5$ L·mol^{-1}·cm^{-1}) is used. The solutions of MgPc are stable for a week (except for the FA solution).

4.4.5 MnPc

MnPc shows comparatively high solubilities in many standard solvents and one of the ionic liquids (EMIM) (Figure 4-4a). The Q bands are usually unaltered, except for NMP and DMPU solutions.

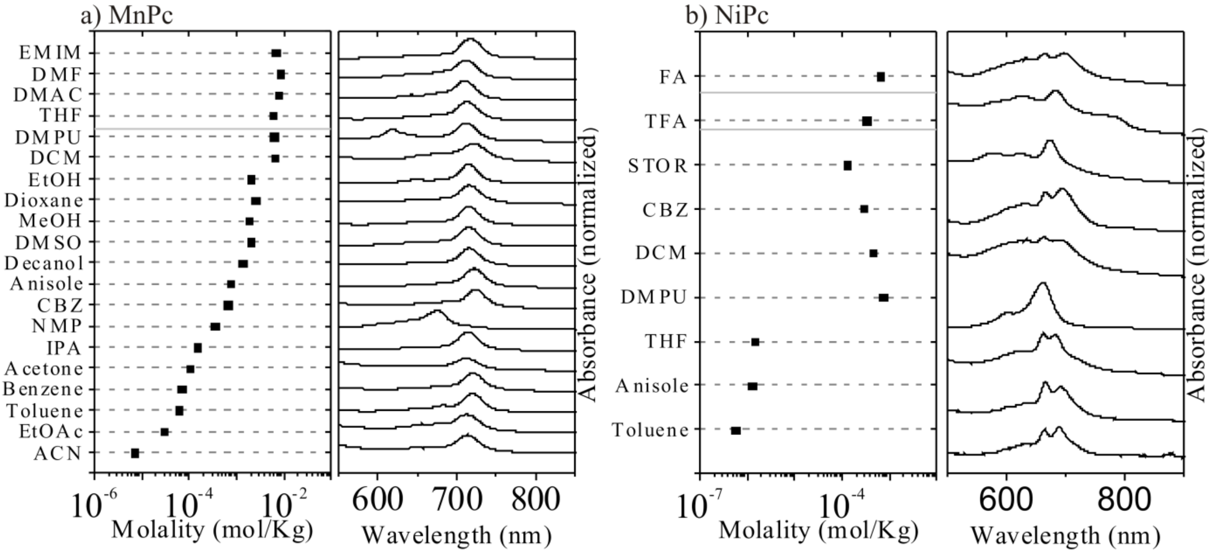

Figure 4-4 a) Maximum concentration of MnPc in different solvents (left) and their corresponding normalized Q-band absorption spectra (right); b) Maximum concentration of NiPc in different solvents (left) and their corresponding normalized Q-band absorption spectra (right).

MnPc is (as FePc and CoPc) well-known for its charge transfer between the metal and the Pc ring [161]. In interaction with the solvent the central metal can be oxidized from Mn(II) to Mn(III) [162, 163]. It was not possible to obtain stable solutions in acids and measure their spectra. For poor solvents, the maximum concentration is estimated with a mean molar absorption coefficient of (2.7 ± 1.4) × 10^4 L·mol^{-1}·cm^{-1}.

MnPc solutions are not very stable and have to be prepared and measured within less than 4 hours.

4.4.6 NiPc

In most of the studied solvents, NiPc has a solubility below a reasonable spectroscopic quantification limit. The Q band is typically split into two bands, see Figure 4-4b. Supposedly this originates from a lowered symmetry of the molecule resulting in non-degenerate electronic states [100]. For estimating the concentration, it was assumed that the most intensive absorption band has the "normal" oscillation strength of the symmetrical Pcs with degenerated LUMO (eg) and thus a single Q band [46]. A mean value of (3 ± 1.5) × 10^5 L·mol^{-1}·$\text{cm}^{-1}$is used for the molar absorption coefficient. It was derived from the spectra of solutions of TFA and SA which had a sufficiently high solubility to quantify a molar absorption coefficient. NiPc solutions are stable for four days.

4.4.7 SnPc

SnPc has a rather low solubility in the studied solvents (Figure 4-5a). The Q bands in all conventional solvents are quite regular. In acids, the spectra are shifted in comparison to conventional solvents. Edwards et al. reported that strong acid solvent like TFA causes a dimerization or exciton coupling between SnPc rings [46].

Due to the low solubility in conventional solvents, the molar absorption coefficient could not be measured individually. Only for the DCM the molar absorption coefficient in DCM (roughly 4 × 10^4 L·mol^{-1}·cm^{-1}) could be estimated. The saturation solubility for the various solvents was estimated using a mean absorption coefficient ((7 ± 4) × 10^4 L·mol^{-1}·cm^{-1}) derived from DCM, SA and TFA solutions. SnPc solutions are stable for four days.

4.4.8 ZnPc

ZnPc is comparatively soluble in many solvents (many types of solvents, Figure 4-5b). In conventional solvents, the Q band remains unaltered. In acid, the Q band shifts, broadens and new absorption bands appear. The band broadening is similar to MgPc and other Pcs. Hanke et al. showed that the activation energy for the decomposition of FA in the presence of ZnPc is slightly larger than for FePc, CuPc, NiPc, and CoPc [150, 164].

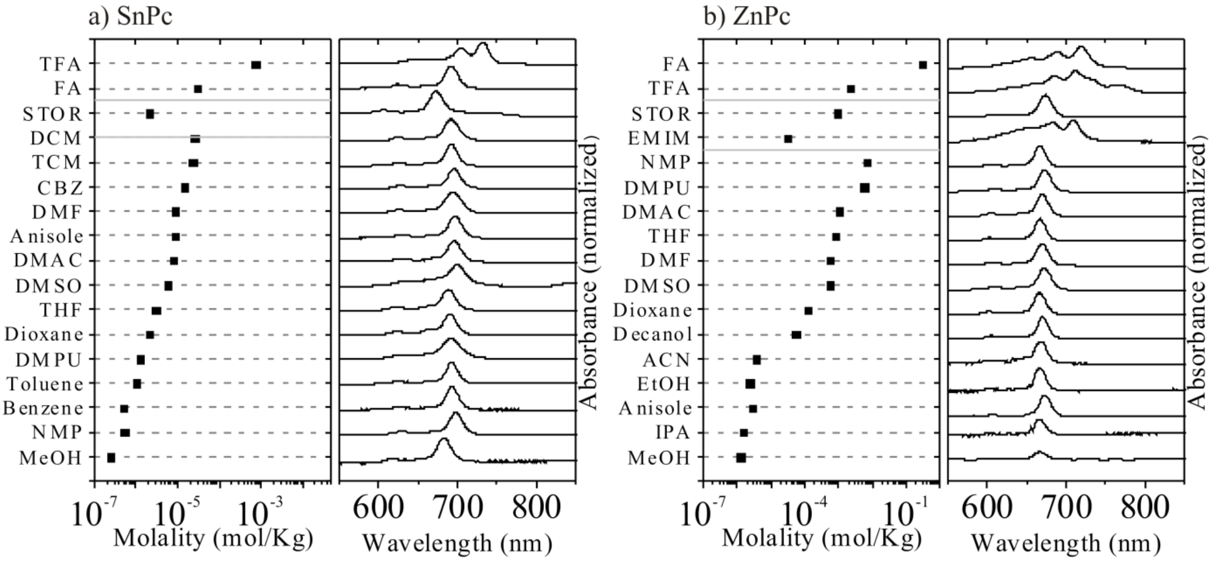

Figure 4-5 a) Maximum concentration of SnPc in different solvents (left) and their corresponding normalized Q-band absorption spectra (right); b) Maximum concentration of ZnPc in different solvents (left) and their corresponding normalized Q-band absorption spectra (right).

For poor solvents the saturation concentration was estimated with a mean molar absorption coefficient of (2.2 ± 1.1) × 10^5 L·mol^{-1}·cm^{-1}. ZnPc solutions (including FA) are stable within four weeks.

4.5 Summary and conclusions

The solubility and spectral solution properties of the unsubstituted metal Pcs CoPc, CuPc, FePc, MgPc, MnPc, NiPc, SnPc and ZnPc were studied quantitatively in different conventional solvents, ionic liquids, and acids. For each metal Pc solution the molar absorption coefficient was measured (above 10^{-4} mol·Kg^{-1}) or at least estimated (for the low solubility cases), based on the absorption intensity of the Q band. The saturation concentration was determined for quite a number of solvents, including “conventional” solvents (e.g., toluene, DMSO, etc.), ionic liquids, and acids (in particular TFA). Solvent-induced spectral alterations were discussed, in particular in view of the chemical stability of the solutions. According to this study, MgPc and ZnPc have the highest solubility and their solutions are stable in ambient atmosphere for weeks. FePc, MnPc and CoPc can be dissolved with considerable concentrations but their solutions are less stable and alter within hours up to one day. This can be seen from the broadening and shift of the Q bands. CuPc, NiPc and SnPc are little soluble in most of the tested solvents and the molar absorption coefficients and saturation concentrations could only be estimated (except for TFA, where the solubility is rather high). Especially CuPc has a good solubility in TFA. CuPc, NiPc and NiPc solutions are rather stable (more than one day) in ambient conditions.

5. Solution Processed Deposited Films

Chapter overview: In this section several morphologies prepared by deposition of solutions, introduced in the previous chapters are presented. Based on the solubility studies, solutions are used, which are chemically stable and show sufficiently high solubility. Finally, the structures, which seem to be appropriate for OSC, are chosen to be studied systematically.

An appropriate solvent for producing a dry thin film should 1) have a high enough evaporation rate, 2) have a high enough solubility to dissolve a reasonable amount of material for thin film deposition (> 10^{-4} mol L^{-1}), 3) be chemically stable. Films prepared with solvents of low evaporation rates do not dry under deposition conditions and are also not applicable, like DMSO, DMPU, NMP and etc.

An appropriate thin film for OSC should 1) be chemically stable, 2) have a homogenous coverage in µm ranges, 3) have feature/structures within the range of the exciton-diffusion length (< 100 nm), and 4) produce a close thin film to prevent short-circuits in OSCs.

5.1 Thin film deposition from solution

From the solubility results, see chapter 4, it can be seen that molecular films of several unsubstituted metal Pcs can be produced via solution deposition techniques like spin casting or dip coating. For instance, Figure 5-1 shows some of the structures prepared by spin casting a SiO_2 substrate with MgPc and ZnPc solutions. Figure 5-1a shows structures deposited from MgPc/FA solution. The structures are fibrous and do not form a closed film. Structures prepared by deposition of ZnPc in DMAC, Dioxane and THF solutions are not homogeneous and also do not yield a closed film.

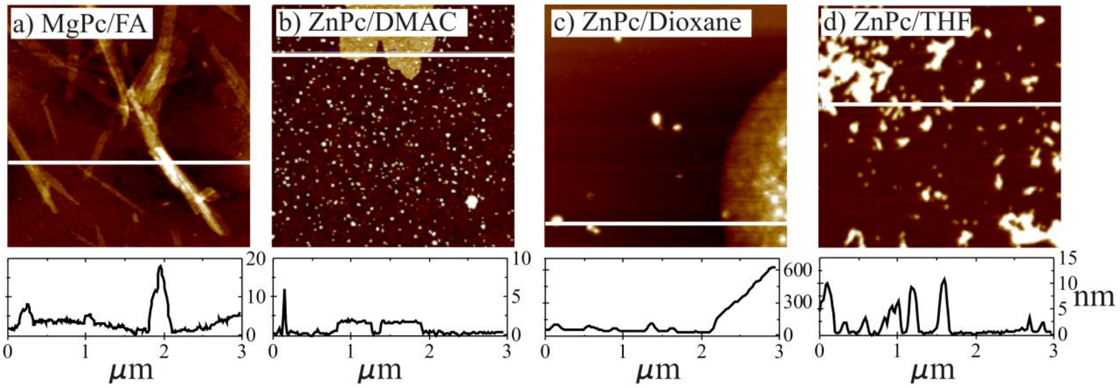

Figure 5-1) AFM images of different unsubstituted metal Pc prepared by spin casting (35 rps) the solution of a) MgPc/FA, b) ZnPc/DMAC, c) ZnPc/Dioxane and d) ZnPc/THF

Among several solvents TFA has a good solubility (~ 10^{-3} mol/L) and high evaporation rate (~ 0.5 μm/s). CuPc and ZnPc in TFA solution are stable while FePc, CoPc and MnPc solutions degrade under ambient condition within one day. Spin casted FePc, CuPc and MgPc TFA solution yield interesting fiber-like structures, which are potentially interesting for OSCs, see Figure 5-2. The CuPc have a homogeneous coverage up to 100 of μm, Figure 5-2a. FePc coverage is not homogenous and alters within some μm on the substrates, Figure 5-2b. MgPc coverage is also homogeneous as is the case of CuPc, Figure 5-2c. ZnPc aggregates into large particles which are inappropriate for OSC, Figure 5-2d. According to literature, CuPc and ZnPc are both the most appropriate materials for an OSCs with unsubstituted Pc [165].

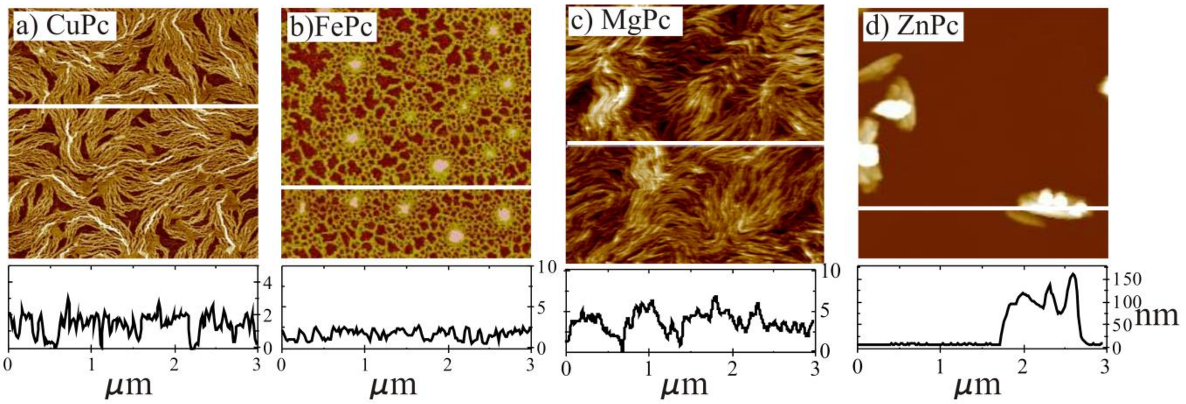

Figure 5-2) AFM images of different unsubstituted metal Pc prepared by spin casting (35 rps) a solution of a) CuPc, b) FePc, c) MgPc, and d) ZnPc in TFA.

Because CuPc/TFA solutions have proven in the initial experiments to be the most promising candidates for OSC production, the CuPc structure deposited from TFA by spin casting are studied in detail. CuPc/TFA favorable properties are: good solubility [133] and acceptable evaporation rate of the solvent, chemical stability of the CuPc/TFA solution [133], promising morphology found in the initial study, as well as application in OSC [80, 108].

5.2 CuPc deposited from solution

CuPc structures deposited from solution can be controlled via several parameters. In the following, the influence of concentration and temperature is shown. Furthermore the structure can be controlled by deposition from a solution mixture, e.g. mixture of TCM and TFA, see appendix 6.

5.2.1 Dip coating with different concentrations at room temperature

The SiO_2 substrate was dip coated into CuPc/TFA solutions with concentrations ranging from 2×10^{-6} to 1.2×10^{-3} $mol \cdot L^{-1}$ for 1 mm/s (millimeter per second) dipping speed, see Figure 5-3.

At low coverages a submonolayer is observed, where CuPc aggregates into single ribbons with a height of ~ 1 nm, varying width (< 50 nm) and length, see Figure 5-3a and 5-3b. At higher coverages, a submonolayer mesh is formed. The CuPc molecules aggregate into long, interconnected flat ribbons of uniform height (~ 1 nm) and varying widths (tens of nm). The ribbons are lying flat on the substrate without any overcrossing and form a mesh (2-dimentional aggregates), see Figure 5-3c to 5-3f. The concentration of the solution determines the amount of deposited material and influences the morphology. By increasing the concentration, the size of CuPc nanoribbons increase, see Figure 5-3a to 5-3f for width. The width, length and coverage of CuPc films are controllable via the solution concentration. As Figure 5-4a shows the coverage is linearly increasing with concentration. The widths increase linearly with increasing the concentration (amount of the material per area), Figure 5-4b.

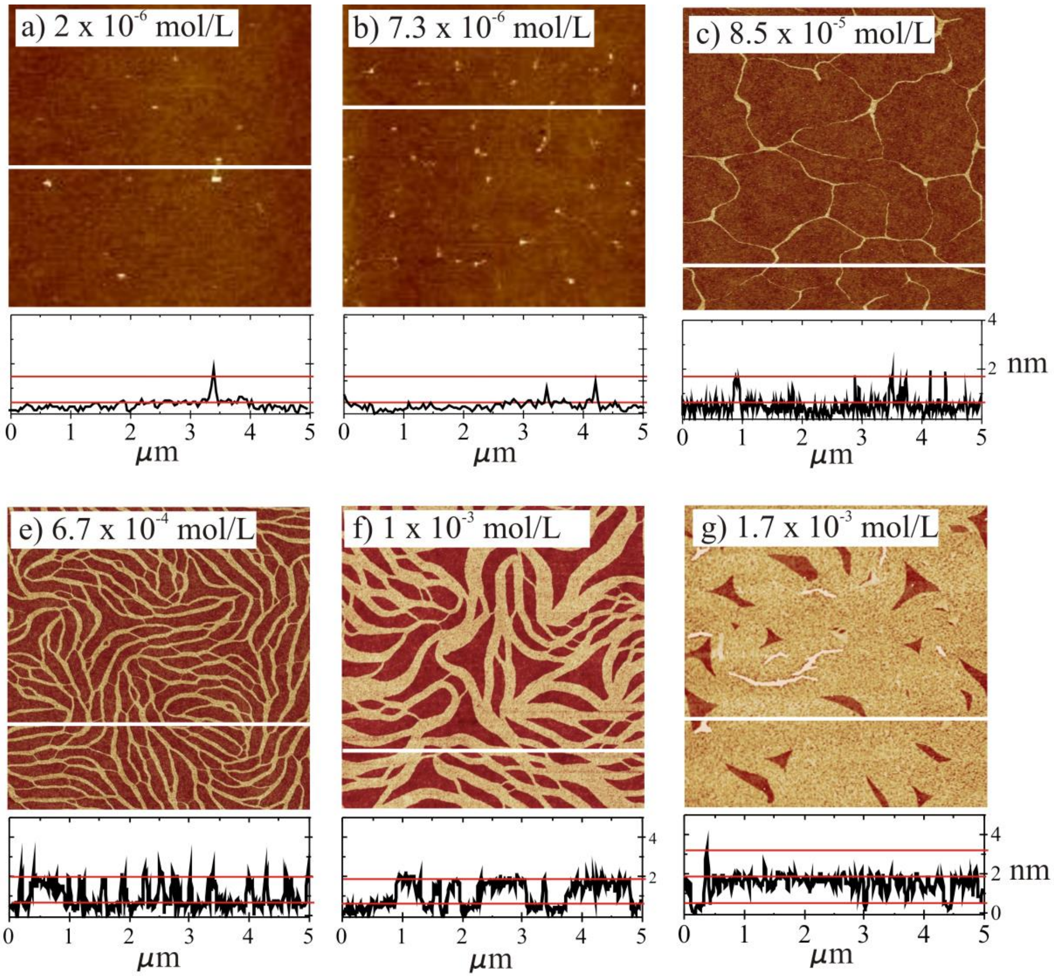

Figure 5-3) CuPc deposited by dip coating (1 mm/s) the SiO_2 substrate into CuPc/TFA solution. The yellow areas in AFM images represent the CuPc structures and the dark brown areas represent the SiO2 surface.

With increasing the amount of the adsorbed material the following is found: an increase of 1.) the number of ribbons per area, 2.) their widths, and finally at multilayer coverage 3.) the number of layers of ribbons, with the height of each layer being ~1 nm, see Figure 5-3. To a first approximation, the increase is linear. Further measurements on film thicknesses are presented in appendix 2. Similar morphologies form by spin casting the solution, which will be presented in chapter 7, where also the adsorption of the molecules from solution and the formation of the structures will be discussed in detailed.

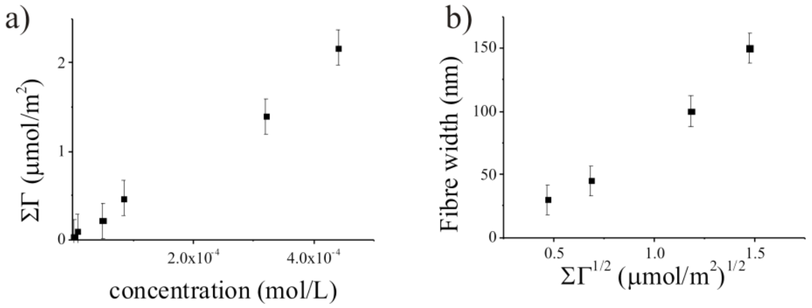

Figure 5-4 a) Amount of the adsorbed material versus solution concentration, b) Fiber width versus amount of the adsorbed material.

5.2.2 Dip coating at different temperatures

Figure 5-5 shows CuPc structures deposited at different temperatures. To this end, the substrate was dip coated into CuPc/TFA solution (7×10^{-4} mol·L^{-1}, 1 mm/s) at different environmental temperature ~ 0°C, at room temperature, ~ 22°C, and heated up to ~ 70-80°C, see Figure 5-5. At ~ 0°C, discrete areas of constant thickness (Figure 5-5a), at room temperature (~ 22°C) areas of stripes with uniform intensity (Figure 5-5b) and at higher temperature aggregates of varying but high intensity are found, Figure 5-5.

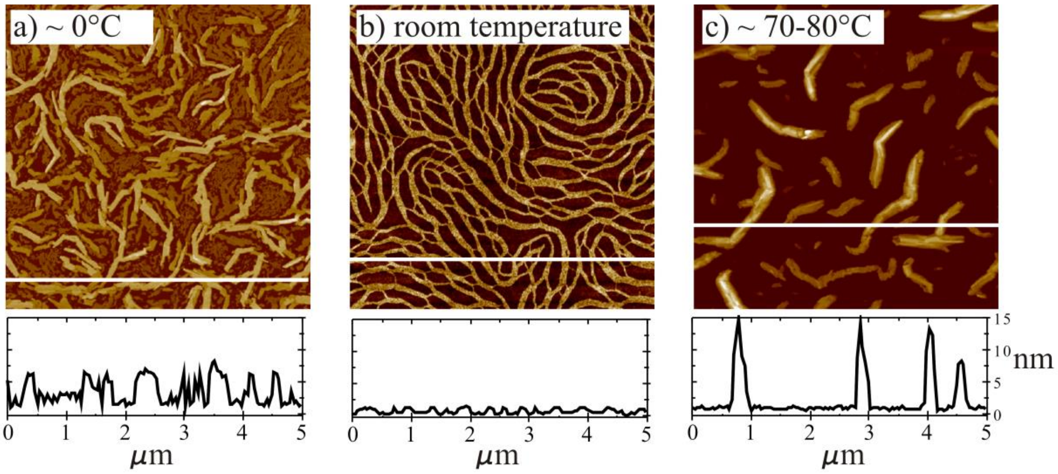

Figure 5-5) CuPc deposited by dip coating (7 × 10 4 mol•L-1, 1 mm/s) at a) ~ 0°C, b) room temperature, c) ~ 70-80°C.Below are given the height profiles along the white lines in the images.

At ~0°C CuPc aggregates into islands which overlap. At room temperature as explained above CuPc aggregates into nanoribbons of ~ 1 nm thickness. At ~70-80°C, single isolated aggregates form. These aggregates have a thickness of up to 15 nm. These aggregates can be used as a template for OSC. Apparently it is possible to control the CuPc structures deposited from solution with ambient temperature.

5.3 Summary and conclusions

CuPc dissolved in TFA is used among several thin films of Pcs as the most promising morphology for OSCs for further studies.

It is found that, CuPc deposited from TFA solution at room temperature aggregates into nanoribbons of ~ 1 nm thickness. The width of the nanoribbons depends on the concentration of CuPc. At higher temperature isolated rod-like aggregates of 10-15 nm thickness and µm length form. At lower temperature (~ 0°C) separate islands of < 5 nm thickness cover the substrate. It is shown that the shape of the aggregate and the coverage depend on temperature and CuPc concentration.

6. Material Properties of Copper Phthalocyanine Deposited from TFA Solution

Chapter overview: In this chapter the material properties of the CuPc dissolved in TFA and precipitated form TFA solution by evaporation of the solvent at room temperature are presented. The crystal structure of CuPc deposited from TFA is compared with those of common CuPc-crystal phases. The stability, dimerization and solvatochromic effect of CuPc in solution are studied. The aggregation of CuPc in solution and the influence on the absorption spectrum are investigated. The spectral characteristics of the CuPc thin film is studied with FT-IR and UV-Vis spectroscopy.

6.1 Crystal structure of CuPc precipitated from TFA

CuPc molecules align into molecular stacks in solid form [23]. The color of CuPc varies between blue and green and is affected by the mode of molecular stacking within the crystal [6]. CuPc has polymorphs with crystal structures such as α-, β-, γ-, δ-, ε-, π-, χ-phases. Among them α- and β-phases are the most common ones [166-169]. The crystal structure of CuPc deposited from TFA was studied by X-ray powder diffraction of bulk CuPc and X-ray diffraction of drop casted films. The molecular orientation and size of the unit cell was estimated to a first approximation by comparing the measured diffraction with previously published data.

6.1.1 Bulk properties measured by X-ray powder diffraction

In the following three different XRPD measurements are presented: CuPc before dissolution in TFA, after dissolution in TFA and after heating up to 200°C for 30 min under vacuum .

Before dissolution in TFA: According to XRPD measurements, CuPc exists in a β-phase, see Figure 6-1a. In this phase CuPc molecules are packed in molecular stacks with ~0.97 nm distance between stacks and 0.48 nm distance between the individual molecules [170]. Within the stacks the molecules are inclined by 45° with respect to the main molecular axis, so that each copper molecule coordinates with the nitrogen atom in the outer ring of the two next molecules [7, 170, 171].

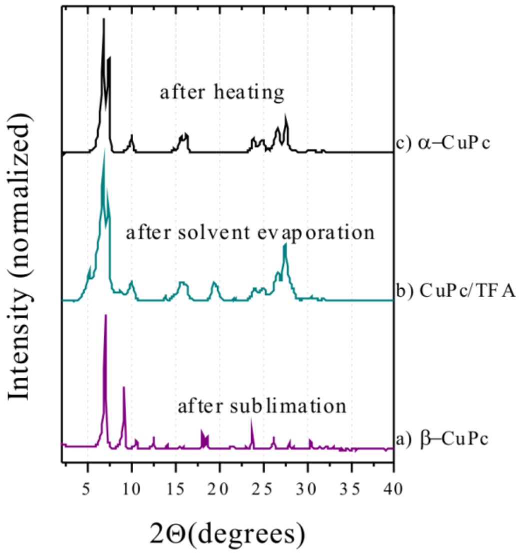

Figure 6-1) Measured diffraction pattern of CuPc a) after sublimation, b) after evaporation of TFA and c) after heating

After TFA evaporation: The diffraction pattern of CuPc deposited from TFA solutions (CuPc/TFA) resembles that of the α-phase , see Figure 6-1. The identical pattern was available neither in ICDD nor in publications. For this study, it was important to know if CuPc molecules are still arranged in the molecular stacks, because the stacking arrangement is used to estimate the material density in AFM images. Therefore, it was necessary to derive the key parameter of the structure from the diffraction pattern.

After TFA evaporation and heating: The measured diffraction pattern of CuPc is the XRPD pattern of α-phase. According to Hoshino et al., the unit cell in the α-phase is triclinic (space group P -1 (2)) with crystal axis a = 12.8860 Å, b = 3.7690 Å, c = 12.0610 Å, and α = 96.22°, β =90.62° and γ = 90.32°[131], see Figure 6-2. The molecules in the stack are tilted by ~ 26° with respect to the molecular axis.

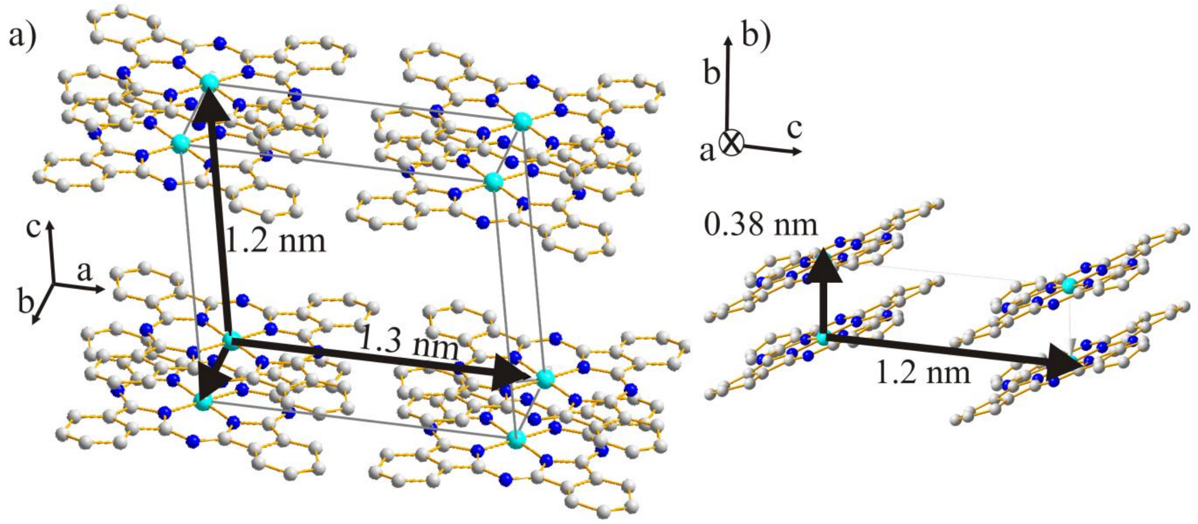

Figure 6-2 a) Unit cell of α-CuPc in bulk; b) 2-D crystal ; orientation of α-CuPc molecules in stacks

The XRPD pattern of CuPc after solvent evaporation (CuPc/TFA) shows all the peaks representing the d-spacing of the molecular stacks (~ 13.2 Å and 12.1 Å). This confirms that CuPc molecules are indeed arranged in molecular stacks. Notably, there are minor changes compared to the diffraction pattern of α-CuPc: shift in the d-spacing of some peaks (≤ 0.5 Å) and additionally new peaks appear at a d-spacing: 17.3 Å, 10.15 Å, 6.4 Å and 4.5 Å. However Hoshino et al. showed that the one at a d-spacing 6.4 Å and 4.6 Å may also appear in α-CuPc, but with intensity close to background noise. Nevertheless, they are expected in the calculated diffraction pattern. The peaks at d-spacings 17.3 Å and 10.5 Å do not appear in α-CuPc. It is reasoned that these peaks appear due to a symmetry break in the α-CuPc structure caused by solvent molecules present in the crystal. Additionally, these two peaks are approximately double d-spaced to the one at ~ 8.8 Å and 5.5 Å, which might become visible due to crystal distortion by solvent molecules. The presence of solvent molecules in the material is also confirmed by FT-IR spectra.

6.1.2 Film structure studies by X-Ray diffraction

The X-ray diffraction pattern of drop casted CuPc films has a broad peak around 5° to 8° which corresponds to a d-spacing of 17 Å to 12 Å, see Figure 6-3. After heating the film at 200°c for 30 min under vacuum, two diffraction peaks appear which are almost at the same d-spacing as that of the bulk after heating, i.e. ~13 Å and 12 Å. This is the typical spacing between the columnar stacks of CuPc as also seen in XRPD.

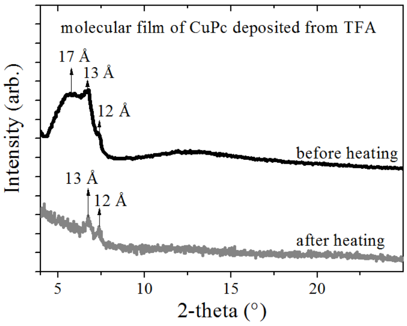

Figure 6-3) Measured XRD of a film of CuPc deposited from TFA by drop casting a) after deposition, b) after heating under vacuum for 30 min

These XRD results confirm that the nanoribbon pattern, presented in the former chapter, are formed from parallel columnar stacks of the molecules covering the substrate. The stacks have a distance of about 1.2-1.3 nm. In those stacks the molecules are inclined with respect to the molecular axis and have a distance of about ~ 0.4 nm, see Figure 6-4.

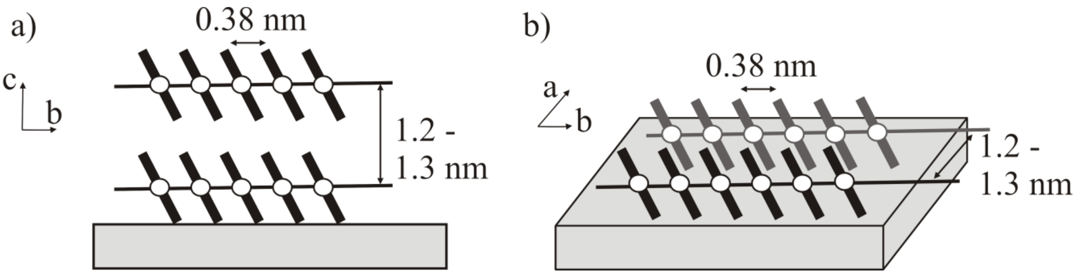

Figure 6-4 Schematic Pc arrangement a) perpendicular to the surface; d) parallel to the substrate

6.2 CuPc/TFA solution

6.2.1 CuPc/TFA solution properties

CuPc shows a strong absorption band in TFA solution. The four peripheral nitrogen atoms in CuPc can be protonated so that $[CuPc.H]^{+}$, $[CuPc.2H]^{2+}$,$[CuPc.3H]^{3+}$and $[CuPc.4H]^{4+}$ are formed. The number of protonated nitrogen atoms (1 to 4) depends on the acidity of the medium, or the excess amount of TFA in the solution [172, 173]. In case of protonation, the maximum absorption band of the Pc (Q band) is red-shifted [174]. According to Lin et al., protonation leads to a symmetry change of the Pc molecule. Thus the symmetry drops from D_{2h} to C_{2v}, and the e_g orbital (HOMO) splits into two orbitals, a_1 and b_1. The a_{2u} orbital (LUMO) does not change. The absorption band upon protonation is related to the $a_{2u}\rightarrow b_1$ transition. The intensity of the $a_{2u}\rightarrow b_1$ in comparison to $a_{2u}\rightarrow a_1$ depends on the concentration of the protonated species [174].

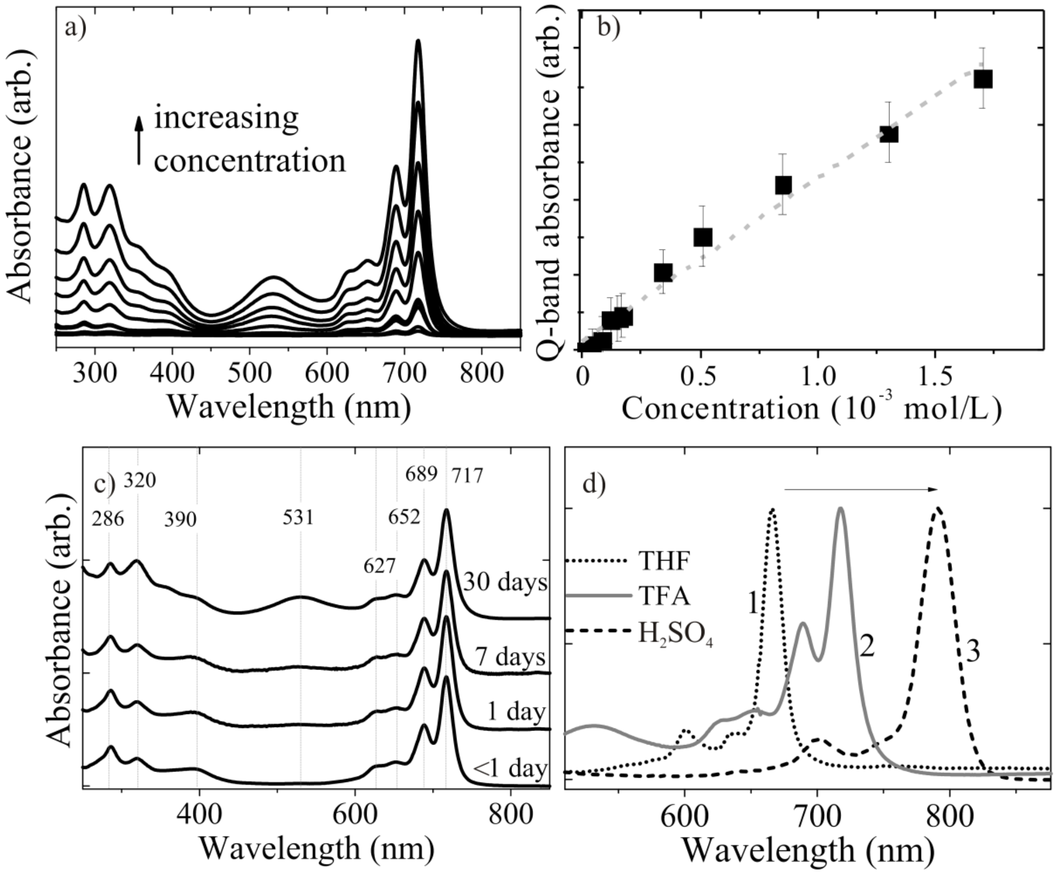

Figure 6-5 a) UV-Vis spectra of CuPc solutions of different concentrations: b) Absorbance of the Q-band versus CuPc concentration; c) UV-Vis spectra of a CuPc solution at different times after preparation; d) red shift in the absorption of the Q band with increasing solvent polarity (from THF to sulfuric acid).

Besides protonation dimerization, aggregation and degradation have an impact on the spectra. These parameters are studied together with the solvatochromic effect in CuPc solution.

Absorption: The concentration dependent absorption spectra of CuPc solutions are presented in Figure 6-5a, where the concentration is varied between 4.5×10^{-5} and 1.7×10^{-3} $mol \cdot L^{-1}$. The UV-Vis spectrum is associated mainly with $\pi \rightarrow \pi^*$ transitions of the strong Q-band (600nm-750nm) and the broad B-Band (300nm-450nm) with weaker transitions near those bands [89-91, 93, 130]. Gouterman et al. showed that to a first approximation the strong Q-band (600nm-750nm) originates from $\pi \rightarrow \pi^*$ transitions from a_{1u} to e_g^* orbitals. The broad B band is caused by transitions between a_{2u} and b_{1u} to e_g^* orbitals [85, 90-92]. The weak and broad absorption band at about 530 nm is associated with the charge transfer between ligand and metal in the Pc molecule [24].

Dimerization: Dimerization of Pc in concentrated solutions causes a shift and an intensity change of some CuPc absorption bands [99]. A deviation from Lambert-Beers' law for concentration dependent measurements is commonly used to check if dimerization occurs. To verify, if Lambert-Beers' law is obeyed, the absorbance of the Q-band, at 717 nm, versus CuPc concentration is plotted. Figure 6-5b shows that absorbance increases linearly with increasing concentration. Therefore, dimerization can be excluded for the concentration window under investigation.

Stability over time: Unprotonated metal Pcs are catalysts that are capable to activate oxygen [37, 174]. Additionally, protonation weakens the peripheral C-N bond, which can therefore react more easily with activated oxygen leading to decreased Pc stability in acidic solutions. Lin et al. reported that the decomposition depends also on the axial coordination ability [174]. While CuPc is one of the most stable metal-Pc, Fe-, Mn- or CoPc decompose fast in the presence of acids [46, 145].

To study the stability of the solution under ambient conditions, the absorption spectra are measured at different times after solution preparation between less than one day and one month (Figure 6-5c). The UV-Vis spectra show that CuPc is stable in TFA for at least one month. However, the intensity of the ligand and metal charge transfer band at 530 nm increases, which is an indication for a beginning aggregation [24]

Solvatochromic effect: Dissolved Pcs often show solvatochromic effects, such as changes in the position, intensity or half-width of the absorption bands due to the solvent-solute interaction [93, 95, 97]. The absorption bands can be red or blue shifted due to a charge transfer [93, 138, 157]. In the solvatochromic effect, the polar state involved in the transition will be stabilized more by polar solvent. Thus the transition energy changes and causes a red or blue shift in the absorption band [175].

Figure 6-5d shows a comparison of the CuPc Q-band in three different solvents: THF, TFA, and H_2SO_4. With increasing solvent polarity, from THF to H_2SO_4, the Q-band exhibits a bathochromic shift (red shift) due to the fact that the excited state of the π→π* transition in CuPc is polar and, thus, stabilized by a polar solvent. Therefore, the transition energy decreases and the corresponding band is red shifted [175].

6.2.2 Aggregation of CuPc in solution

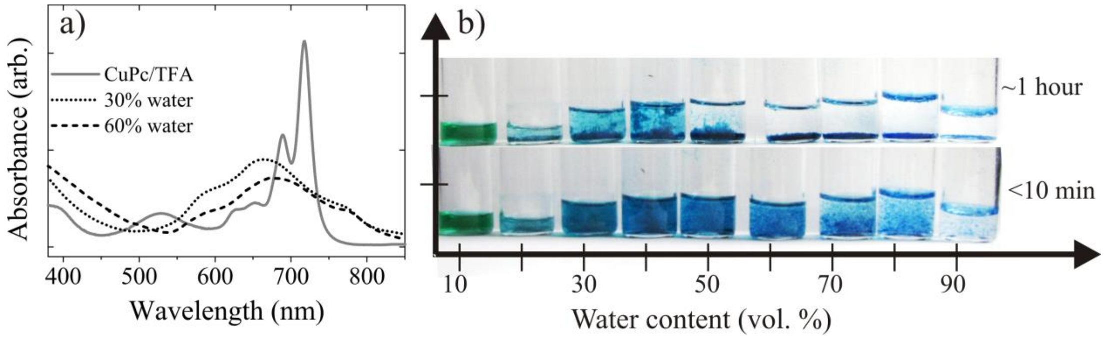

Figure 6-6 a) UV-Vis spectra of the Q-band region of CuPc in TFA without water and with 30%-vol. and 60%-vol. water; b) precipitation of CuPc in TFA/water mixtures for different water/TFA ratios after less than10 min and after 1 hour.

Aggregation of CuPc in a good solvent is achieved by either solvent evaporation or by adjusting the solubility through addition of a poor solvent. In both cases, the solution becomes supersaturated and CuPc starts to aggregate. Figure 6-6a shows how the addition of water, as poor solvent, to CuPc/TFA solutions (~ 10^{-4} mol·L^{-1}) leads to aggregation and influences the UV-Vis spectra. The Q-band of the solutions broadens, shifts to lower wavelengths, and displays a weaker absorbance.

This formation of CuPc aggregates in volume ratios between 10 to 60%-vol. water is shown in Figure 6-6b. The images confirm that for less than 10%-vol. water CuPc does not aggregate in the solution. For water contents between 20 and 50%-vol., the aggregates remain dispersed within the first 10 min after preparation and then slowly precipitate to some extent within 1 h . With further increase of the water content, CuPc aggregates directly and completely sediments within 10 min.

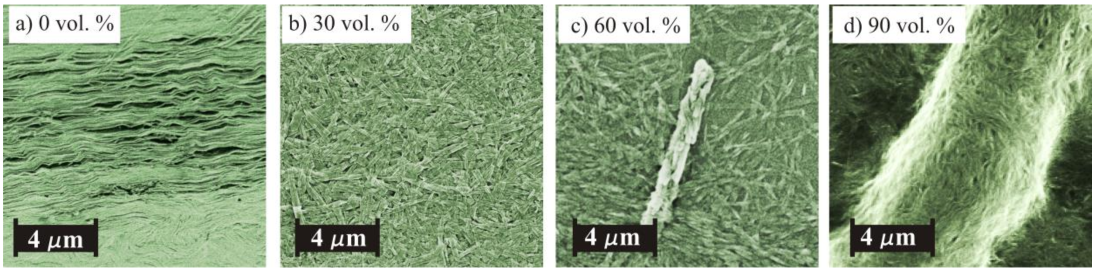

Figure 6-7) SEM images of CuPc/TFA aggregates from solvent with water content of a) 0%; b) 30%, c) 60% and d) 90%.

The size and shape of the CuPc aggregates, depending on the water content in the solution, was studied by SEM, Figure 6-7. The solutions/dispersions were drop casted onto the SiO_2 substrates and allowed to dry. If no water was added before drop casting, fibers that developed during drying were found, Figure 6-7a. The fibers have a width of less than 100 nm and lengths of some 10 μm. By increasing the water content to 30%-vol., an increase in fiber width to ~200 nm and a morphology change was observed, Figure 6-7b. Further addition of water led to the formation of larger rod-like aggregates with a diameter of ~1 μm and a length of some 10 μm (Figure 6-7c, 60%-vol. water). By further increasing the water content to 90%-vol., extended fibers with a diameter of 6 μm and a length of several 10s of μm were formed, Figure 6-7d.

Concerning the UV-Vis absorption and SEM images, two processes can be distinguished in aggregation of CuPc into fibrous structures: 1) aggregation in the solution by decreasing the solubility and formation of aggregates in solution, 2) aggregation due to evaporation of the solvent. The shape and size of the aggregates produced in these two processes and the UV-Vis spectra are different.

6.2.3 Cryo-TEM of CuPc in solution and TEM of CuPc aggregates

The TEM image of a frozen liquid film of CuPc/TFA (Figure 6-8a and 6-8b) and of dried CuPc structures precipitated from CuPc/TFA solution (Figure 6-8c, 4-8d and 6-8f) are compared to see if any aggregates of CuPc are present in the solution. Especially the fibrous aggregates, observed in the dry film, were detected.

The light gray area in the images of Figure 6-8a and 6-8b present the edge of a cell in the TEM-grid. The light grey area is the frozen liquid film (1.7×10^{-3} $mol\cdot L^{-1}$). As Figure 6-8a and 6-8b show, no aggregates could be detected in the frozen liquid film area.

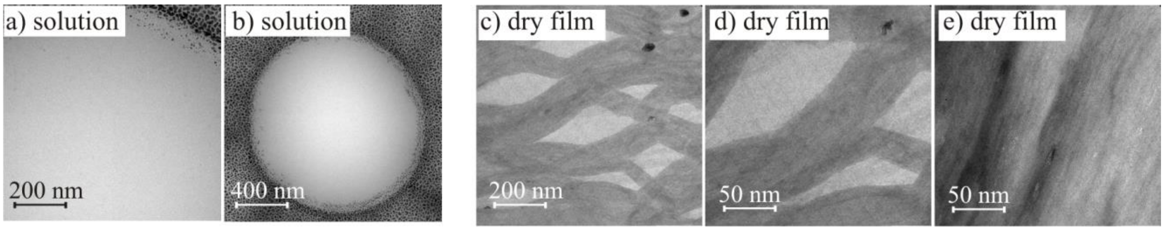

Figure 6-8 a, b) Cryo-TEM image of CuPc/TFA solution c, d and e) TEM image of dry film after solvent evaporation.

Figure 6-8c, 6-8d and 6-8e shows the TEM measurements of CuPc ribbons after solvent evaporation. The solution was drop casted onto the TEM grids and allowed to dry. Figure 6-8c and 6-8d show nanoribbons of some 10 nm width, formed by drop casting a solution of 3.4×10^{-4} $mol\cdot L^{-1}$ concentration. Figure 6-8e shows nanoribbons (width > 100 nm) prepared by drop casting a solution of higher concentration (1×10^{-3} mol/L). These Cryo-TEM measurements confirm the UV-Vis results that CuPc nanoribbons are not formed in the starting solution but by evaporation of the solvents.

TEM measurements show that the surface of CuPc nanoribbons is smooth to first approximation, Figure 6-8c. At higher resolution the surface of the nanoribbons has a striped texture, Figure 6-8e. Presumably this texture is due to the stacking arrangement of CuPc molecules, see Figure 6-8e.

6.3 Spectral characteristics of CuPc molecular films

The properties of CuPc molecular films were studied via FT-IR and UV-Vis spectroscopy after evaporation of the solvent and after heating at 200°C under vacuum for 30 min, see Figure 6-9a and b.

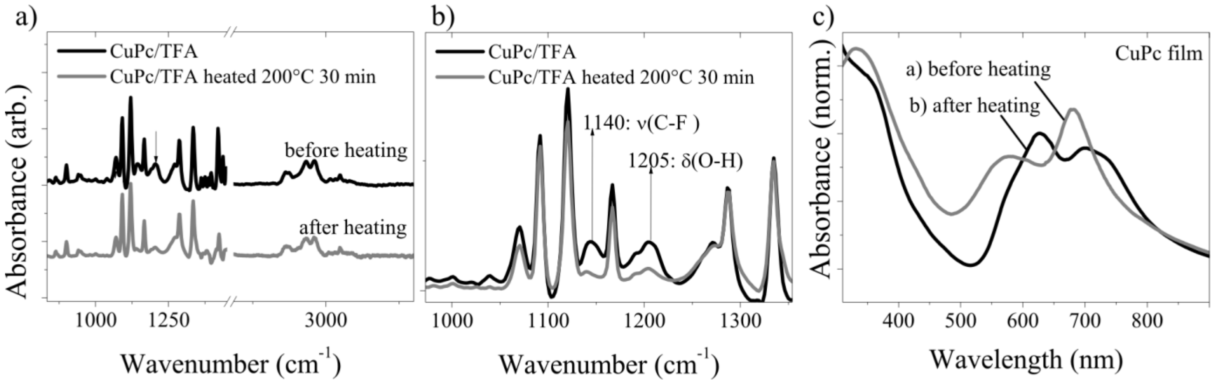

Figure 6-9 a), b) FT-IR spectra, c) UV-Vis spectra of CuPc film before and after heating

6.3.1 FT-IR Spectra after evaporation and after heating

The FT-IR spectra of a CuPc molecular films have typical vibration modes [176] [172] of the CuPc such as η(N-N) and ρ(C-C) at ~ 900 cm^{-1}, δ(Cu-N) at ~ 947 cm^{-1}, η(N-N) and η(C-C) at ~ 1070 cm^{-1}, δ(C-H) at ~ 1167 cm^{-1}, δ(C-C) and ρ(C-H) at ~ 1287 cm^{-1}, and ν(Cu-N), δ(C-N), ν(C-C) and η(N-N) at ~ 1334 cm^{-1}, see Figure 6-9a and 6-9b. In the FT-IR spectra of CuPc molecular films after evaporation of TFA, the ν(C-F) stretching mode at ~ 1140 cm^{-1} from TFA [177, 178] is present. This peak vanishes by heating the sample to 200°C for 30 min under vacuum. Heating decrease also the intensity of the δ(O-H) in plane bending mode at ~ 1205 cm^{-1} [179].

6.3.2 UV-Vis Spectra after evaporation and after heating

Figure 6-9c shows the absorption band of CuPc film after solvent evaporation and after heating at 200 °C under vacuum for 30 min. The Q-bands of CuPc film after deposition appear at ~ 580 nm and ~ 682 nm. These bands shift to higher wavelength, ~ 627 nm and ~ 700 nm, after heating the sample, see Figure 6-9c.

The UV-Vis spectra of thin solid films in comparison with solutions are more complicated due to interfacial and especially Davydov effects [93]. The latter result from the interactions in the unit cell which lead to the splitting of the exciton energy states in the solid molecular film. From the above FT-IR studies one concludes that by heating the molecular film the TFA molecules desorb. As XRPD studies show by heating the CuPc after precipitation from TFA the symmetry in the unit cell of CuPc changes slightly. The band shift in the UV-Vis absorption spectrum can be related to the annealing of the molecular film and elimination of TFA molecules.

6.3.3 AFM measurement after evaporation and after heating

Figure 6-10 shows the AFM image of CuPc nanoribbons spin coated on SiO_2 substrates a) after solvent evaporation and b) heated under vacuum at 200 °C for 30 min. The purpose of this heat treatment was 1) annealing (chemical and physical equilibration) and 2) getting rid of any residual solvent (including H_2O, TFA is hygroscopic). Figure 6-10 demonstrates that the heat treatment does not change the morphology of the CuPc ribbons significantly.

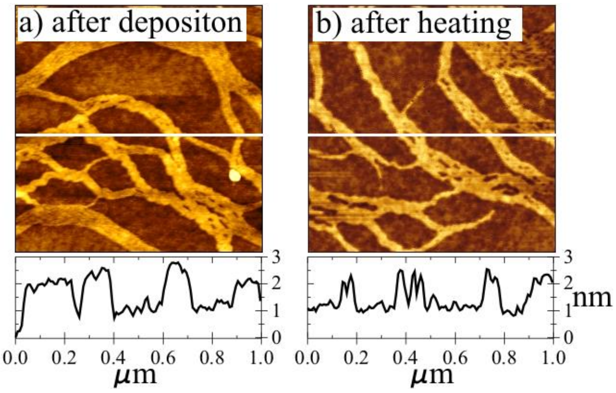

Figure 6-10) CuPc deposited by spin casting from TFA solution: a) after deposition b) ditto after additional heating at 200 °C for 30 min under vacuum.

6.4 Summary and conclusions

The measured FT-IR and UV-Vis spectra and X-ray diffraction results show that CuPc deposited from TFA solutions exhibits a distorted α-phase crystal, meaning that the CuPc molecules are arranged in molecular stacks each of which is approximately 1 nm apart and the spacing between CuPc molecules in the stack is about ~ 0.4 nm. The molecules are standing with the short edge on the substrate and build up molecular stacks parallel to the surface.

UV-Vis measurements of the solutions reveal that CuPc solutions show a solvatochromic effect, which depends on the acidity of the solvent. CuPc dissolves in TFA by protonation of the Pc moieties leaving the CuPc/TFA solution nevertheless chemically stable. Concentration dependent UV-Vis spectra propose that dimerization of CuPc molecules in TFA solutions is negligible. On the other hand, aggregation can be induced by adding a poor solvent to the solution. This aggregation can be followed by UV-Vis spectra as broadening of the Q-band and associated intensity decrease.

Cryo-TEM results confirm that CuPc molecules dissolve homogeneously in TFA. The nanoribbons form by evaporation of TFA. TEM measurements show that the surface of the CuPc nanoribbons is smooth. Especially, at high resolution, the surface of the nanoribbons shows a striped texture in the nm range. Presumably, this texture is due to the arrangement of CuPc molecules in the stacks. Spectroscopic measurements show that a small amount of solvent molecules is present in the dry film. They can be removed without significant influence on the morphology of the nanoribbons by heating at 200°C under vacuum for 30 min.

7. Nucleation and Growth of Copper Phthalocyanine

Chapter overview: In this chapter the nucleation and growth of CuPc nanoribbons from solution on SiO_2 substrate is studied. The CuPc nanoribbons form by spin casting the CuPc/TFA solutions. In the liquid film, the CuPc concentration increases due to evaporation of the solvent. Eventually the solution becomes supersaturated and the CuPc molecules deposit onto the substrate and form CuPc nanoribbons of approximately uniform height (~ 1 nm), see Figure 7-1 (cross-section below AFM images). To understand how these nanoribbons are formed by spin casting the solution and evaporation of solvent, the spin casting theory is studied in detail for CuPc/TFA.

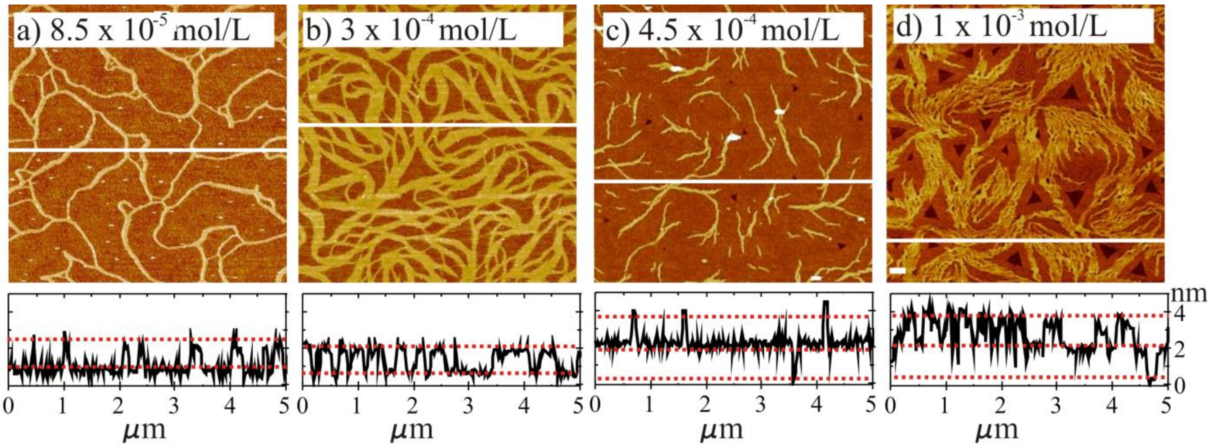

Figure 7-1) AFM image of CuPc nanoribbons spin casted from different CuPc/TFA solution concentration on SiO_2. The cross-section (height information) below each image shows that the height of nanoribbons is ~ 1 nm.

The spin casting theory is used to describe the parameter influencing the spin casted liquid film. From this theory the deposited amount of material is calculated and compared with measurements. The important parameters influencing supersaturation, nucleation and growth in the liquid film are calculated to first approximation. The influence of these parameters on nucleation and growth is discussed. The adsorption of CuPcs is explained using adsorption models and discussed based on intermolecular interactions.

Manuscript is under preparation for publishing in “Langmuir”.

7.1 Spin casting

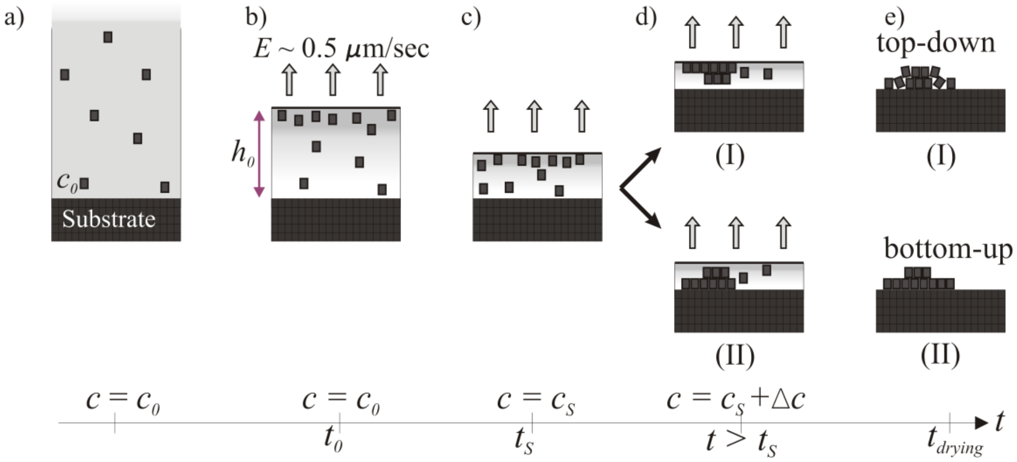

Figure 7-2) Schematic drawing of an evaporating liquid film of CuPc/TFA with CuPc enrichment, deposited by spin casting

The so called spin casting time (t_{sc}) starts with deposition of liquid and ends with complete evaporation, see Figure 7-3. In spin casting, a drop of CuPc/TFA solution is placed onto the rotating substrate, Figure 7-2a. In the beginning, the liquid film becomes thinner mainly due to spin-off (centrifugal forces, hydrodynamic thinning). In this stage evaporation has not a significant influence, so that the concentration remains the weighted concentration of the solution (c_0).

As the film thins, hydrodynamic thinning slows down and at transition point (t_0) the thinning is just due to evaporation of TFA. The transition point is where the evaporative and hydrodynamic thinning becomes equal, Figure 2-7b. The liquid film thickness at transition point is named here h_0.The time at transition point is called transition time (t_0), and at supersaturation is called supersaturation time (t_s). At t_{drying}, the evaporation is finished and the solute is precipitated.

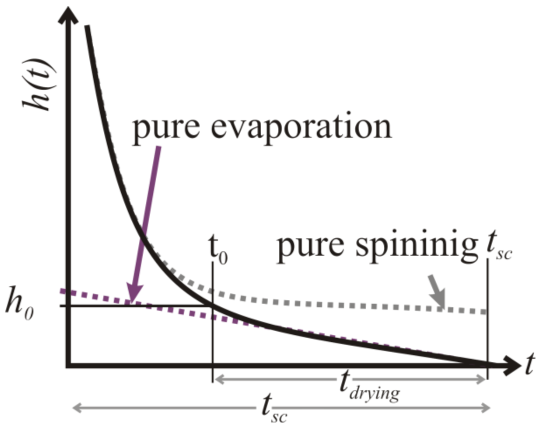

Figure 7-3) Film thickness curve versus time by spin casting

Due to the evaporative film thinning after t_0, the concentration of the liquid film increases. Near to the liquid-vapor interface the concentration is higher due to evaporation, Figure 7-2c. From the enrichment layer the solute diffuses and increases the concentration elsewhere in liquid film. The concentration change in the liquid film depends on the competition between evaporation and diffusion in the liquid film. The Sherwood number is a measure of the competition between diffusion and evaporation in the liquid film [75]. It is defined as: "evaporation rate (E) × liquid film thickness at transition point (h)/ diffusion (D)":

$$Sh = \frac{E.h_0}{D}$$

When the Sherwood number is much larger than one, the evaporation is more effective than concentration. Therefore the concentration near the liquid-vapor interface is significantly larger than elsewhere in the solution. The solution can become supersaturated near this interface, whereas elsewhere in the solution the concentration is below the supersaturation. In this case the solute aggregates near liquid-vapor interface (top-down aggregation), Figure 7-2d (I). After the complete evaporation the aggregates precipitate onto the substrate, Figure 7-2e (I).

When the Sherwood number is much smaller than one, the diffusion is so effective that the concentration in the evaporating liquid film is almost homogeneous. The concentration at liquid-vapor interface is still constantly increasing. However, due to diffusion of CuPc, the concentration increases near the substrate, too. Therefore the solution near substrate can become supersaturated at the same time as the liquid-vapor interface. With a concentration increase beyond supersaturation (Δc), the molecules overcome the nucleation barrier and aggregate near the substrate (bottom-up), Figure 7-2d (II). After complete evaporation the dry film is grown on the surface, Figure 7-2e (II).

AFM images at multilayer coverage, Figure 7-1c and 7-1d, suppose that a molecular film of nanoribbons grow on the substrate and on top of it smaller nanoribbons grow. It shows that the film of CuPc forms a bottom-up aggregation near substrate, as in Figure 7-2e (II).

7.1.1 CuPc coverage by spin casting

The spin casting theory is based on the approximation of the binary mixture of an ideal (Newtonian) volatile liquid and nonvolatile solute. In this theory the evaporation rate is considered to be constant. The amount of deposited material is calculated from solution concentration (c_0) and the liquid film thickness (h_0) at the transition point. This liquid film thickness, h_0, depends on the evaporation rate and spin casting speed.

In the following, the amount of deposited material is calculated based on the spin coating theory and compared with the measured values.

Coverage calculated from spin casting theory: From reflectometry measurements of spin casted TFA liquid films, the evaporation rate is measured as $E \sim 0.5$ µm·s^{-1} and $t_{drying} \sim 1.5$ s, see appendix 2. Karpitschka et al showed that the transition film thickness at transition point is [75]:

$$h_0 = \sqrt[3]{\frac{3\nu \cdot E}{2\omega^2}} = \tag{7-1}$$

$$h_0 = \sqrt[3]{\frac{3 \times 6.4 \times 10^{-7}[m^2 \cdot s^{-1}] \cdot 5 \times 10^{-7}[m.s^{-1}]}{2 \times 35^2\,[s^{-2}]}} = 7.3 \times 10^{-6}\,[m]$$

Where kinetic viscosity (ν) of TFA is 6.4×10^{-7} m·s^{-1} [180, 181]) and spin casting speed (ω = 35 rps).

According to the theory, the final coverage (the amount of material (N) per area (A)) is:

$$\Gamma = \frac{N(h=0)}{A} = \; h_0 \; c_0 \approx 7 \times 10^{-6} \, [m] \, c_0 \tag{7-2}$$

To a first approximation at constant temperature and evaporation rate, the concentration and cubic root of the inverse square of the spinning speed ($\omega^{2/3}$) influence the liquid film thickness. In comparison with concentration the spinning speed has a weaker influence on the coverage. **CuPc coverage determined from AFM images:** Coverages in the AFM images are evaluated by measuring the size of the area covered with CuPc in each image and multiplying it by the number of molecules per area from crystallographic data [131], see Figure 7-4. The maximum coverage of one monolayer without any crystallographic defects on the substrate per area is ~3.1 µmol·m^{-2}:

$$\begin{aligned} \Gamma_{monolayer} &= \frac{1}{area\ of\ CuPc} \cdot \frac{1}{N_A} \\ &= \frac{1}{0.4 \times 10^{-9}[m] \times 1.2 \times 10^{-9}[m]} \cdot \frac{1}{6.022 \times 10^{23}[mol^{-1}]} \\ &= 3.1 \times \; 10^{-6}[mol \cdot m^{-2}\,] \end{aligned} \tag{7-3}$$

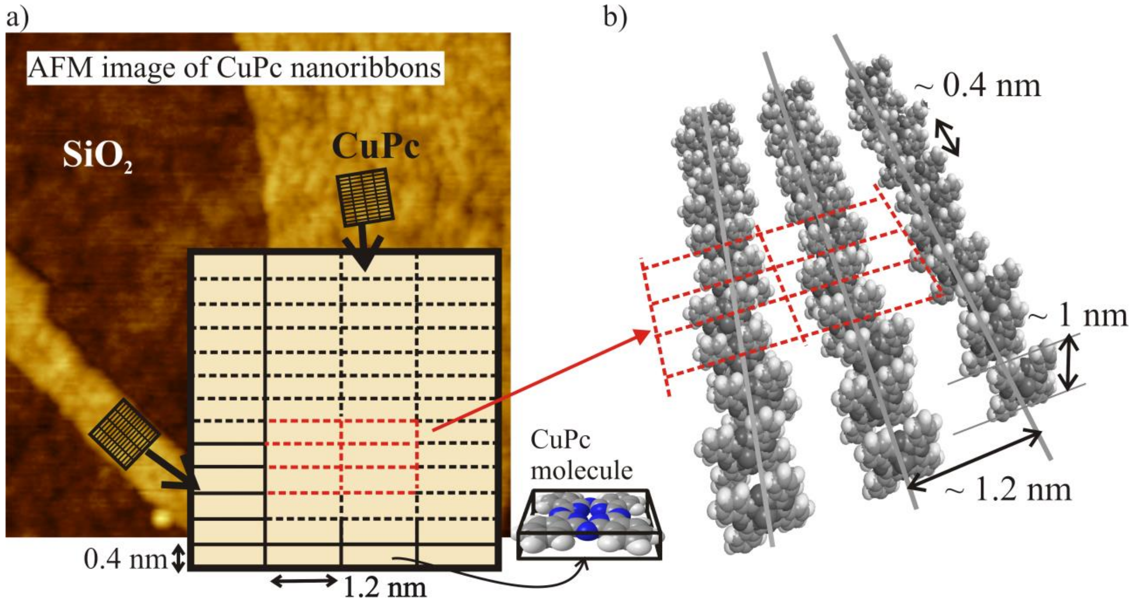

Figure 7-4) Schematic drawing of a) AFM image, yellow area covered with CuPc nanoribbons, brown area represents the bare SiO$_2$ substrate, b) Arrangement of CuPc molecules in molecular stacks

The relative surface area covered with CuPc is measured with SPIP software. It is multiplied with $\Gamma_{monolayer}$ to find the amount of material per area.

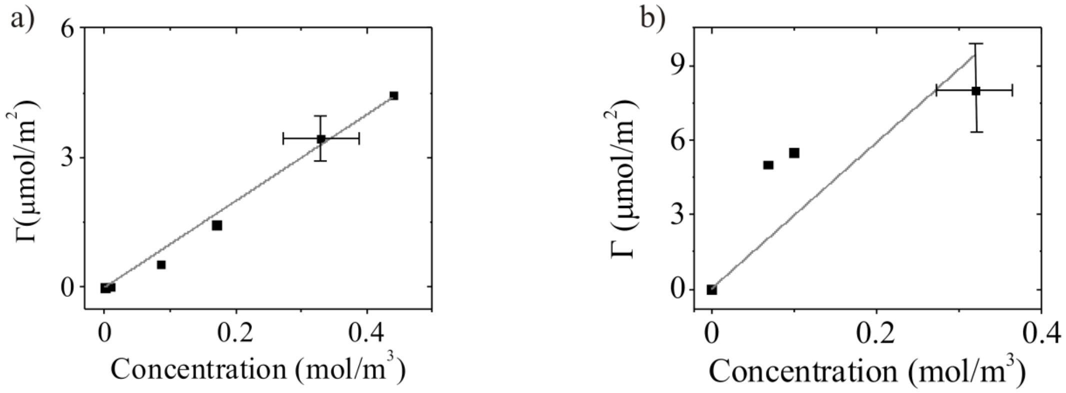

Figure 7-5) a) Coverage measured with AFM versus solution concentrations applied in spin casting, b) coverage estimated from film thickness measurement with ellipsometry, see Appendix 2.

The coverage for a set of AFM images, with CuPc solution of different concentration, spin coated at 35 rps is presented in Figure 7-5a, it is found that:

$$\Gamma = 10 \times 10^{-6}\,[m]\,c_0 \tag{7-4}$$

The difference in the calculated and measured value is in the range of measurement errors, these are mainly errors in the 1) measuring evaporation rate, 2) estimation of the area with SPIP software because of the uncertainty in the threshold of the structure contour, 3) molecule per area estimation due to the assumption of defect-free mono-crystallinity of CuPc nanoribbons, and 4) experimental errors in concentration (volume and weight) due to small weight and volume values for the stock solution.

Coverage from ellipsometry: The amount of deposited material is estimated from ellipsomeric film thickness measurements (appendix 2), Figure 7-5b. However, the estimation is not very accurate for several reasons. It is about 3×10^{-6} [m] c_0. The refractive index of CuPc nanostructures was not known very well. It is taken from literature for similar structures [182, 183]. It is very sensitive to crystal structure of CuPc and wavelength of the incident light. In ellipsometry larger areas of the sample are measured whereas in AFM the area in the middle of the substrate. In ellipsometry the larger aggregates or particle near to the outer film area may contribute to the film thickness. Furthermore the concentration of the solution is not accurate because of the small weight and volume. In one concentration series, although the absolute value has large errors, but since all solutions are prepared from the same stock solution, the relative concentration increase is correct.

Calculated and estimated coverage: The calculated coverage from spin coating theory, equation (7-2), and the measured coverage from AFM images, equation (7-4) and Figure 7-5a, depend both linearly on the solute concentration. The spin casting theory predicts the coverage of CuPc deposited from TFA solution pretty well. This confirms the validity of the theory, which is used in the following to describe nucleation and growth of CuPc structures in spin casted TFA solution.

7.1.2 Deposition of liquid film

In the following, the parameters which play an important role in nucleation and growth in spin casting process are discussed. These are concentration change, supersaturation, diffusion, and evaporation. These parameters are estimated to the first approximation as a function of time (t) for different solution concentrations (amount of material per area, Γ). Time in these calculations is a variable starting from transition point t_0 and ending at the drying point (t_{drying}). For each time interval (δt), t is the residual time and is defined mathematically as $t = t_{drying} - \delta t$. From reflectometry measurement the drying time (t_{drying}) is approximately ~ 1.5 s, see appendix-2. The time at which a solution becomes supersaturated is called supersaturation time (t_s) and the corresponding concentration is called supersaturation concentration (c_s).

Supersaturation: From solubility study, see chapter 4, the approximate supersaturation concentration (c_s) of CuPc in TFA is estimated. The approximate supersaturation concentration (c_s) is estimated from solubility measurement as, see chapter 4:

$$c_s \sim 10 \ (mol \cdot m^{-3}) \tag{7-5}$$

Diffusion: With the help of the Stokes-Einstein relationship [184] the diffusion coefficient (D) of CuPc in TFA is estimated as:

$$D = \frac{kT}{3\pi\eta a} = \frac{1.38 \times 10^{-23}[J \cdot K^{-1}] \times 297[K]}{3 \times 3.14 \times 9.5 \times 10^{-4}[Pa \cdot s] \times 10^{-9}[m]} \approx 4 \times 10^{-10}[m^2 \cdot s^{-1}] \tag{7-6}$$

where η, viscosity of TFA is 8.2 mPa·s^{-1} [180, 181] and a, the diameter of the CuPc is taken ~ 1 nm for the first approximation.

Then Sherwood number for spin casted CuPc/TFA solution is:

$$Sh = \frac{Eh_0}{D} = \frac{5 \times 10^{-7}[m \cdot s^{-1}] \times 7 \times 10^{-6}[m]}{4 \times 10^{-10}[m^2 \cdot s^{-1}]} = 8 \times 10^{-3} \tag{7-7}$$

Sh << 1, which shows that the concentration in the liquid film is almost homogeneous.

Concentration as a function of time: Because of the solvent evaporation the liquid film becomes thinner and the concentration increases. To a first approximation, the thinning of the liquid film is linearly proportional to evaporation rate (*E*). The thickness of liquid film can be indicated as a function of time:

$$h(t) = E.t = E\,(t_{drying} - \delta t) \tag{7-8}$$

$$h(t) = 5 \times 10^{-7}[m \cdot s^{-1}]\ \ t\,, \qquad E \sim 5 \times 10^{-7}\ m \cdot s^{-1}$$

Using equation (7-8) for the thickness, *h(t)*, the total concentration change due to evaporation, *c(t)*, can be calculated as a function of time as:

$$c(t) = \frac{N}{V} = \frac{N}{A\,h(t)} = \frac{\Gamma}{E.t} \tag{7-9}$$

$$c(t) = \frac{\Gamma[mol \cdot m^{-2}]}{5 \times 10^{-7}[m \cdot s^{-1}] \times t} = \frac{1}{5 \times 10^{-7}[m \cdot s^{-1}]} \times \frac{\Gamma}{t}$$

where *V* is the volume of the liquid film, *N* is the number of the molecules in the liquid film, and *Γ* the amount of the material per area (*N/A*, *A*: area). Since CuPc is not volatile, the number of molecules (*N*) is constant and independent of the solvent. Furthermore the area (*A*) is also constant and does not change with film thinning. Therefore it is appropriate to refer to concentration as the amount of molecules per area (Γ), which is proportional to weighted concentration.

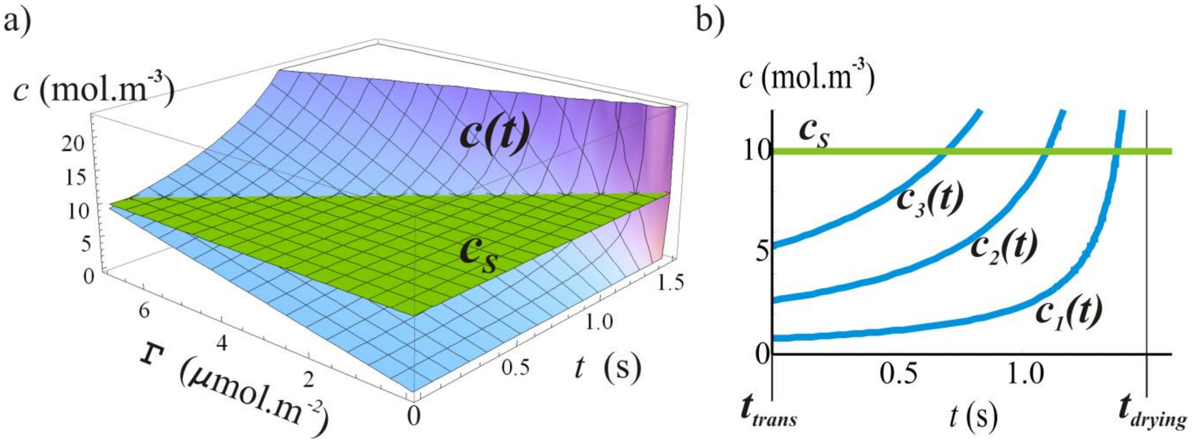

Figure 7-6 a and b) Concentration as a function of time, *c(t)*, of CuPc in the evaporating liquid film and c_s, the supersaturation concentration.

The concentration function of the solution versus time (for different amounts of material per area) is shown in Figure 7-6 in blue, and the concentration at supersaturation in green. After supersaturation, CuPc molecules start to aggregate and after supersaturation, the overall average concentration is approximately constant ($c_S \sim 10\ \mathrm{mol\cdot m^{-3}}$). The "concentration increase" due to evaporation, is compensated by a "concentration decrease" due to aggregation of CuPc molecule. The *c(t)* function reaching supersaturation gives information on the rate of aggregation of CuPc molecules (nucleation and growth rate).

Distance between molecules: The distance between the CuPc molecules in the solution changes due to concentration increase. It can be calculated from equation (7-9) for the mean volume per molecule in the solution, see Figure 7-7:

$$\bar{d}(t) \approx \sqrt[3]{\frac{V}{N}} = \sqrt[3]{\frac{1}{c.N_{av}}} \tag{7-10}$$

$$\bar{d}(t) = \sqrt[3]{\frac{5\times 10^{-7}[m\cdot s^{-1}]}{6.022\times 10^{23}\left[mol^{-1}\right]}\times\frac{t}{\Gamma}} \approx 1\times 10^{-10}\left[mol^{\frac{1}{3}}\cdot m^{\frac{1}{3}}\cdot s^{-\frac{1}{3}}\right]\sqrt[3]{\frac{t}{\Gamma}}$$

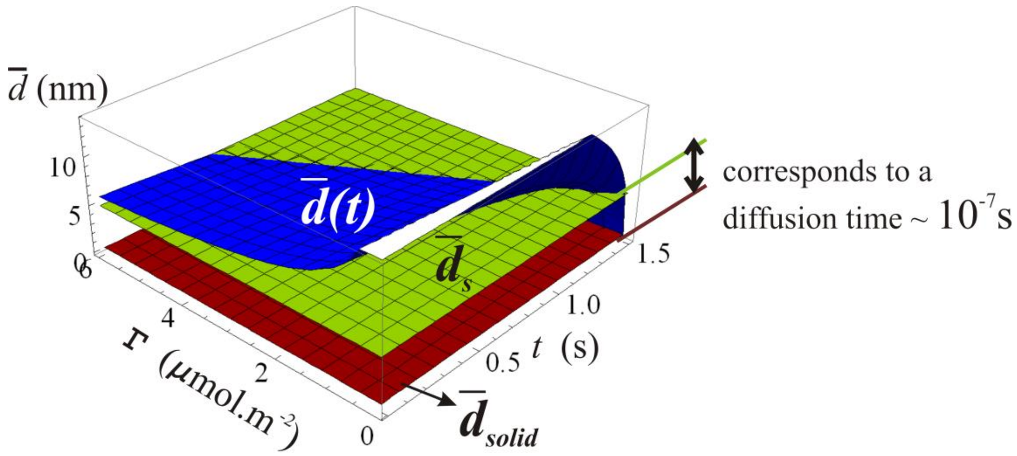

Figure 7-7) $\bar{d}(t)$ the mean distance between CuPc molecules, $\bar{d}_s$,the distance between molecules at supersaturation, and $\bar{d}_{solid}$, in crystal

The distance between the molecules in the solution at supersaturation concentration ($\bar{d}_s$) is estimated from the available volume per molecule at supersaturation concentration (equation 7-5). This distance is:

$$\overline{d_s} \approx \sqrt[3]{V_s} \approx 6\,nm \tag{7-11}$$

The distance between CuPc molecules in crystal can be obtained from the unit cell of α-CuPc crystal [131]:

$$\overline{d_{solid}} \approx \sqrt[3]{V_{crystal}} \approx 0.6\ nm \tag{7-12}$$

The distance curve of CuPc molecules ($\bar{d}(t)$, equation 7-10), the intermolecular distance at supersaturation ($\bar{d}_s$, equation 7-11), and in the crystal ($\bar{d}_{solid}$, equation 7-12) are shown in Figure 7-7 versus time and amount of material per area. Figure 7-7 shows that at supersaturation the distance between the molecules is ~ 10 times larger than the distance between the molecules in crystal. From equation (7-6), this distance between the molecules at supersaturation is equivalent to a diffusion time of 10^{-7}s:

$$\bar{x} = \sqrt{Dt} \tag{7-13}$$

$$t = \frac{\bar{x}^2}{D} = \frac{36 \times 10^{-18}[m^2]}{4 \times 10^{-10}[m^2 \cdot s^{-1}]} = 9 \times 10^{-8}[s] \approx 10^{-7}[s]$$

It means that regarding diffusion the organization of the molecule from solution into solid takes roughly 10^{-7}s time. The drying process after supersaturation typically takes some 10 milliseconds. This means that the aggregation of CuPc at supersaturation is very fast and less influenced by the drying time.

From literature the typical time scale for self-organization of molecules into crystal, is in nano- to microsecond range, including diffusion and conformational dynamics [185, 186]. Figure 7-8 shows the average diffusion time and length of CuPc from equation (7-13). It indicates that in the millisecond range (time from supersaturation to complete drying) the molecule diffusion length is some 100 of nm. With other words, in the microsecond range the diffusion is effective in a region of some 100 nm. Beyond that region concentration gradient can appear. These may result in a local concentration increase over supersaturation and formation of a new nucleus.

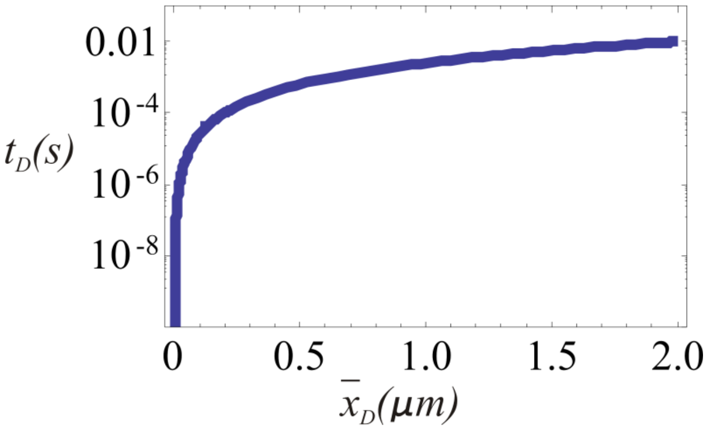

Figure 7-8) The average diffusion time and length of CuPc from $t_D=\bar{x}_D^2/D$

Nucleation: Although the average supersaturation concentration is constant due to a small Sherwood number (effective diffusion in comparison to evaporation), aggregation of CuPcs influences the concentration locally.

At supersaturation, a concentration increase (Δc) causes the CuPc pass the nucleation barrier and forms a nucleus, see Figure 7-9. After the nuclei formation, the CuPc nanoribbons grow spontaneously.

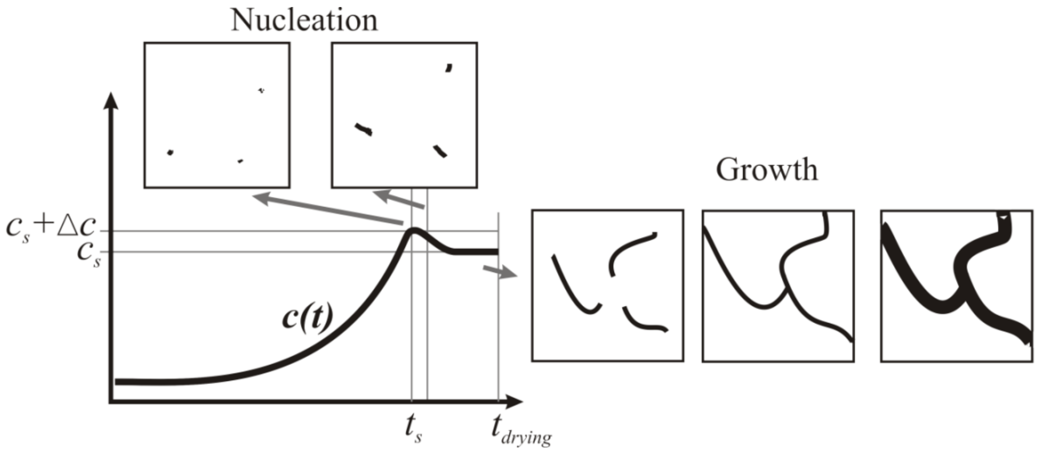

Figure 7-9) Concentration curve of evaporating liquid film

When the nanoribbons form and grow the concentration in a region near the growth fronts decreases slightly and remains at ~ c_S [56]. Molecules from other part of the solution diffuse to this region. The local concentration in that region is determined by the comparative influence of growth rate and diffusion.

In a region where the growth front are more than some 100 nm separated, the diffusion is not effective enough as showed before. The concentration in this region may increase slightly and a concentration gradient forms locally. In that region further nuclei can form. After formation, these nuclei grow. However as they are formed later, they remain smaller. Presumably thinner nanoribbons, which appear in a mesh, are of this type.

7.2 Morphology of the solution processed CuPc film

In the following, the morphology of the CuPc nanoribbons for different concentration is explained. The adsorption of CuPc molecule onto the substrate is discussed. The growth of CuPc nanoribbons in length, width and height of CuPc molecules is explained using AFM images.

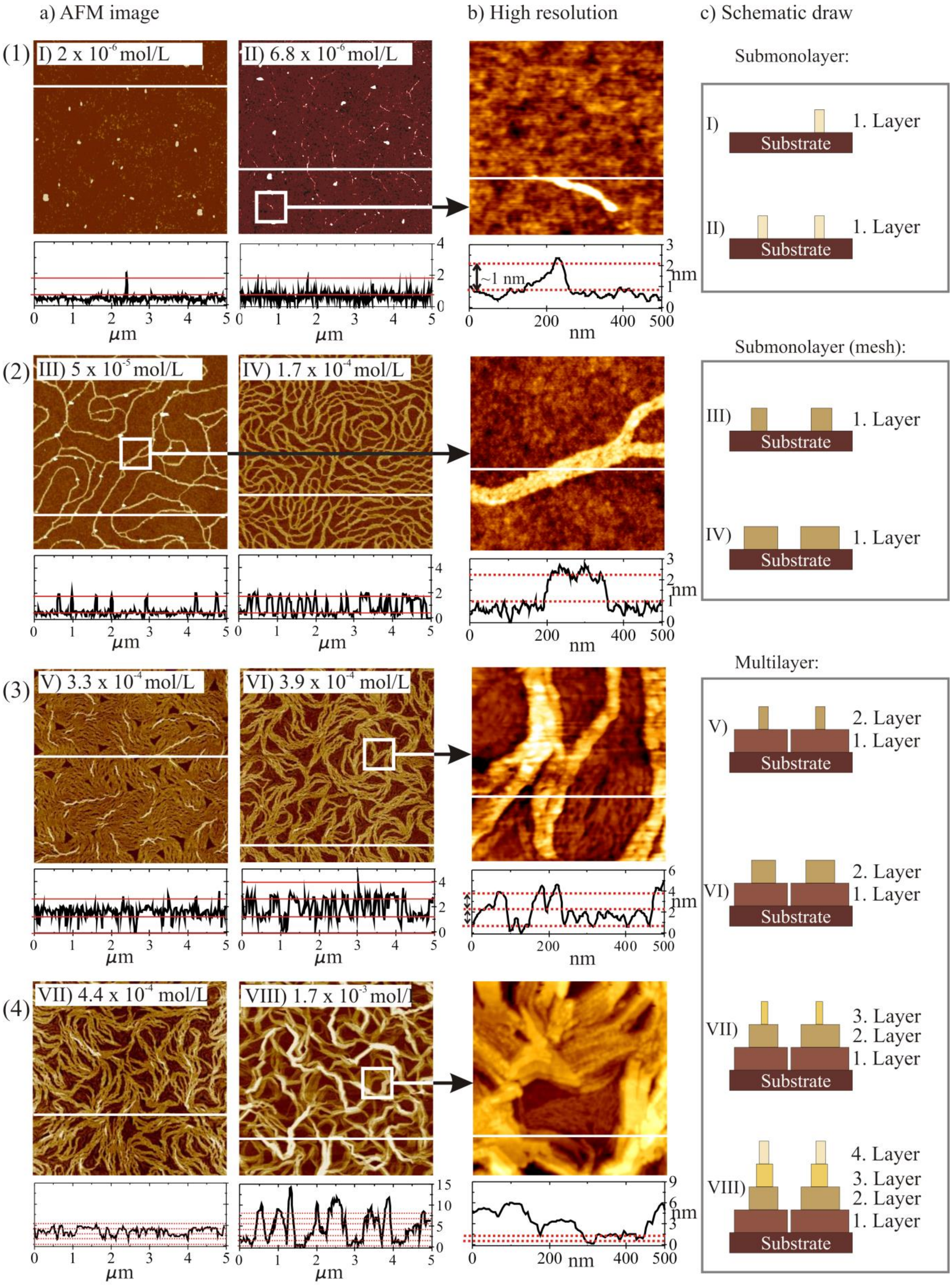

Figure 7-10 a) AFM height image of different solution concentration, b) high resolution AFM image, and c) Schematic draw

Figure 7-10 shows CuPc nanoribbons formed by spin casting CuPc/TFA solutions of different concentrations on a SiO_2 substrate. The SiO_2 serves as planar and smooth model surface to investigate the morphology of CuPc aggregates by AFM. In Figure 7-10a the AFM images of 5µm length, in 7-10b the high resolution AFM images, and in 7-10c the schematic drawing of cross section of AFM images are shown. For each AFM image, a height-profile of a random line is given below the image (cross-section). Images are categorized into four sets: (1) I and II, submonolayer before mesh formation; (2) III and IV, submonolayer after a mesh formation; (3) V and VI, multilayer/ when the second layer forms; (4) VII and VIII, multilayer with more than 2 layers.

1.) First Layer, submonolayer: At very small amount of material per area (< 0.2 µmol·m^{-2} or ~ 7% of a monolayer) small aggregates form, which have the form of individual long strings or sticks, Figure 7-10 (1) with a width distribution < 50 nm. These aggregates increase in length with increasing concentration.

2.) First Layer, submonolayer after mesh formation: As the amount of material per area increases to > 0.2 µmol·m^{-2}, a single-layer-mesh of nanoribbons forms, see Figure 7-10 (2). Each ribbon is typically several tens of nm wide but only about 1 nm thick. In between the ribbons, the bare substrate is exposed. At such submonolayer coverage, CuPc always aggregates into long, interconnected flat nanoribbons of varying widths. The ribbons are lying flat on the substrate without any crossing over, and form a mesh (2-dimentional aggregates). With increasing amount of material per area, the width of the nanoribbons increases.

3.) Second layer: After the amount of material per area increases to ~ 2.5 µmol·m^{-2} (or ~ 80% of a monolayer), a second layer forms, which has also a height of ~ 1 nm, Figure 7-10 (3). By increasing the concentration further the width and length of the nanoribbons in this layer increases, see Figure 7-10 (3).

4.) Multilayer: At larger amount of material per area (> 5 µmol·m^{-2}), a third layer forms. The adsorption in the third layer is similar to the first and second layer, the width and length of the nanoribbons increase with increasing amount of material per area. Importantly, the next layer starts to form at smaller amounts of material per area. The second layer starts when the first layer is filled up to ~ 80%. The third layer forms when the second layer is filled up to ~ 60%

and the fourth layer forms when the third layer is filled up to ~ 30%, see Figure 7-10 (4). In multilayers, the coverage of the upper layer (yellow) is smaller than the layer near the substrate (brown). Hence the cross section of the film has a pyramidal shape, with the apex pointing upward, see Figure 7-10 (4). Based on the shape of the cross-section, a bottom-up growth is assumed, where nucleation and growth starts on the substrate.

7.2.1 Analysis of the morphology of the solution processed CuPc film

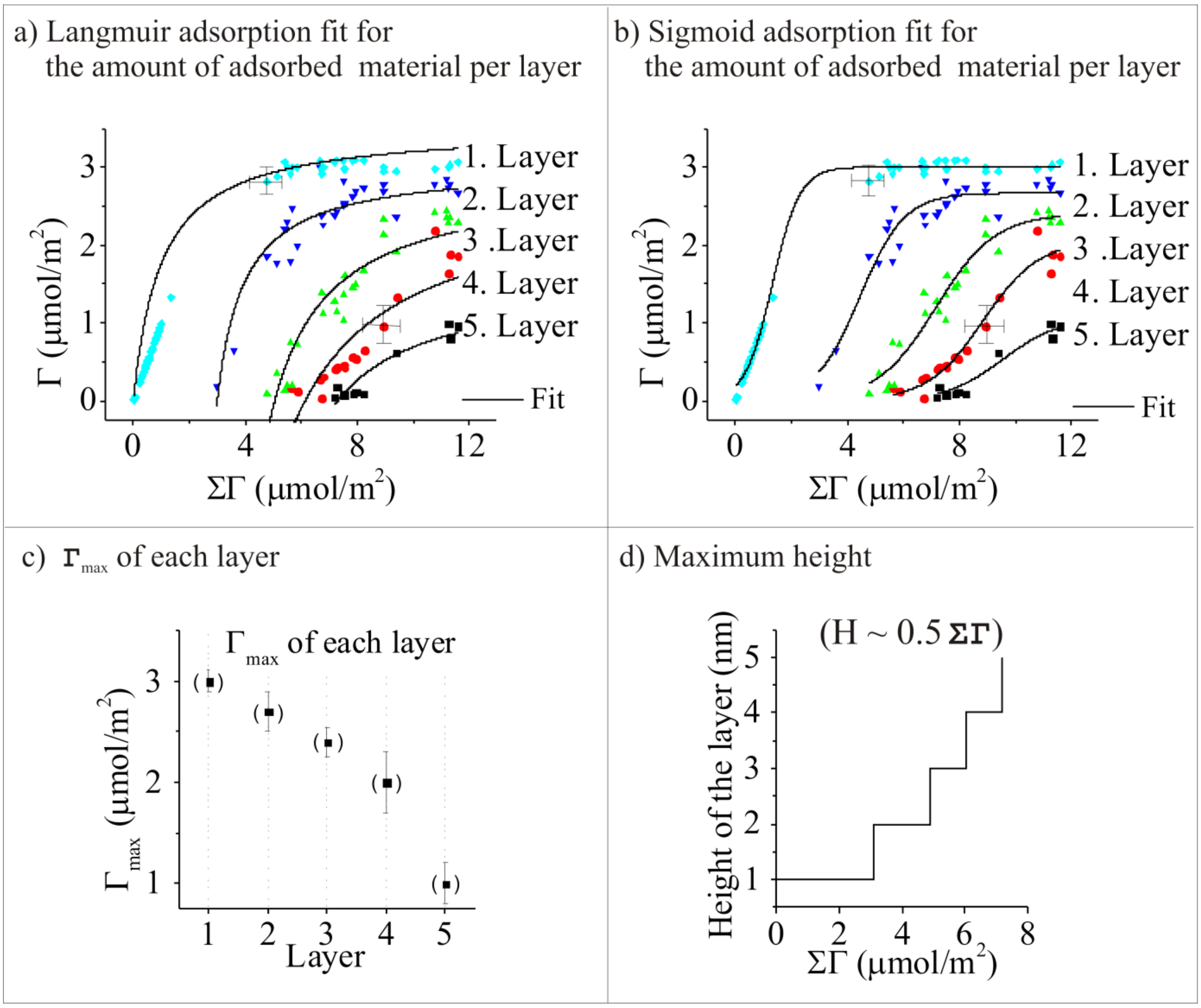

Figure 7-11 Amount of material per area in each layer versus the total amount of material per area a) with Langmuir fit, b) with Sigmoid fit, c) maximum coverage in each layer, d) height (formation of next layer) versus amount of adsorbed material

Figure 7-11 summarizes the results of AFM measurements for multilayer coverage. Figure 7-11a and 7-11b show the amount of material per area in each layer (*Γ*) versus the total amount of material per area ($\Sigma\Gamma$). Each layer is indicated in a different color. Figure 7-11a presents the Langmuir fit and Figure7-11b sigmoidal fit. Figure 7-11c presents the maximum coverage in a layer (Γ_{max}), estimated from the plateau of the fit curve in Figure 7-11b. Figure 7-11d presents the height-change, versus total amount of material per area. The height of each layer is ~ 1 nm. Each point in the curve gives the amount of material per area, at which a new layer is formed, taken from the fit-function of Figure 7-11b.

The Langmuir adsorption assumes that the adsorbing molecules have an interaction with the substrate. Other interactions are assumed to be negligible. The sigmoidal function involves a cooperative growth. In a cooperative adsorption molecules attach better to a surface if they can interact with neighboring adsorbate molecules [53]. The Sigmoid function fits better to the data, see Figure 7-11a and 7-11b. It supposes that the CuPc molecules interact with each other. The adsorbed CuPc neighboring molecules provide a binding site for the free molecules. At the inflection point the amount of adsorbed material in that layer is large enough to provide many binding sites for free molecules and the adsorbent is not yet too saturated. With increasing amount of adsorbed material, the number of vacant sites in the layer decreases so that adsorption rate in that layer also decreases. When the layer becomes saturated the amount of the adsorbed material is maximum (Γ_{max}) and the adsorption rate in the layer decreases to zero and the next layer starts to form.

The maximum coverage for each layer in Figure 7-11a and 7-11b can be calculated from the saturation coverages of that layer, i.e. coverages before the next layer forms. The maximum coverage of the first layer is ~ 3 $\mu mol\cdot m^{-2}$. Within the next layer this value decreases to ~ 2.7 $\mu mol\cdot m^{-2}$, see Figure 7-11c.

Figure 7-11c shows at which amount of material the next layers form. It also explains the relation between the height increase of the film and the amount of adsorbed material for a rough approximation.

Nanoribbon formation: The nanoribbon formation can be studied specially at lower concentration, Figure 7-10 (1) and 7-10 (2). In the following the information on these coverages are summarized and compared.

The measurements show that the size of nanoribbons increases by increasing the amount of material per area; however their height remains constant in submonolayer (~ 1 nm). It is assumed that between nanoribbons of different sizes (area A_1 and A_2, width w_1 and w_2, length L_1 and L_2) geometrical similarities exists. This assumption is just to compare the ratio of nanoribbons size increase. For the first approximation, it is assumed that the length and width are proportional ($w=a\cdot L$):

$$\frac{A_1}{A_2} = \frac{L_1 \cdot w_1}{L_2 \cdot w_2} = \left(\frac{L_1}{L_2}\right)^2 = \left(\frac{w_1}{w_2}\right)^2$$

The area is proportional to the number of the molecule. The number of the molecule per area ($\Sigma\Gamma$) is also proportional to length and width:

$$\frac{\Sigma\Gamma_1}{\Sigma\Gamma_2} \propto \left(\frac{L_1}{L_2}\right)^2$$

In the following, the increase in length, width and height is estimated according to the square root of the amount of material per area. Because of the measurement difficulties, the measured length, width, and height are parameters of different concentration regimes.

The length data is from concentration regimes before a mesh form. The width of nanoribbons in this regime (measured > 5 nm and < 50 nm) is very sensitive to the radius of AFM tip and hard to measure, see appendix 5.

In a concentration regime after mesh formation the width increase is significant. In a mesh, the ribbons are connected and no length can be identified.

The height of the ribbons at submonolayer is ~ 1 nm. The height increase requires a new layer formation, which means that the mesh is almost filled up and no length and width can be measured. At the upper layer, the ratio of width and length is so large that it is not possible to follow the concentration dependence experimentally.

To compare the changes of length, width and height of the nanoribbons, a linear fit is used for fitting the data to the first approximation. This fit allows comparing the ratio of increase in each dimension with increasing the concentration approximately.

Length: before a mesh forms, the length of nanoribbons increases, see Figure 7-12a. In this regime nanoribbons of various length and width are available. Between larger nanoribbons, smaller one appears. These nanoribbons nucleate later, as discussed before. From AFM images of low coverages the increase in the average length versus concentration can be followed, Figure 7-10 (1).

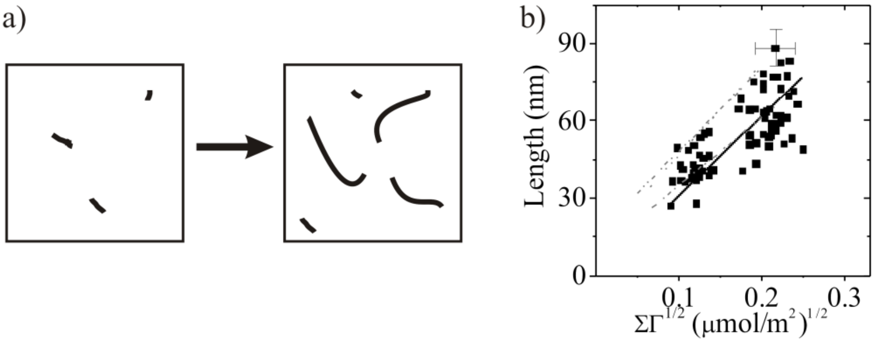

Figure 7-12 a) Schematic draw of length increase, b) length versus square root of amount of material per area

The length of nanoribbons versus the number of molecules per area are shown in Figure 7-12b. The ratio of length-increase (R_L) versus the total number of molecule per area ($\Sigma\Gamma$) is defined to the first approximation as:

$$R_L = \frac{\Delta(L)}{\Delta\sqrt[2]{(\Sigma\Gamma)}} \tag{7-14}$$

Δ(L) is the increase in length of the nanoribbons (L) and ($\Sigma\Gamma$) is the number of the molecule per area. From the linear fit in Figure 7-12b, the ratio of length-increase is:

$$R_L \approx 300\ [\mu mol^{-1/2}] \tag{7-15}$$

Width: when the mesh forms, the average width of the ribbons increases with increasing number of molecules per area, Figure 7-10 (2). In the free spaces between the ribbons of a mesh, thinner ribbons can be seen. Their smaller width supposes that they are formed later than the other ribbons. These ribbons are also connected to the mesh and almost no free ribbon ends can be detected. Therefore in this regime, no length increase can be detected.

Similar to length-increase, R_W is defined to compare the increase in width with the number of molecules per area (*ΣΓ*):

$$R_W = \frac{\Delta(W)}{\Delta\sqrt[2]{(\Sigma\Gamma)}} \tag{7-16}$$

Δ(W) is the increase in width of nanoribbons (*W*). From the linear fit in Figure 7-13b, the ratio of width-increase to the amount of material per area for the first approximation is:

$$R_W \approx 50\ [\mu mol^{-1/2}] \tag{7-17}$$

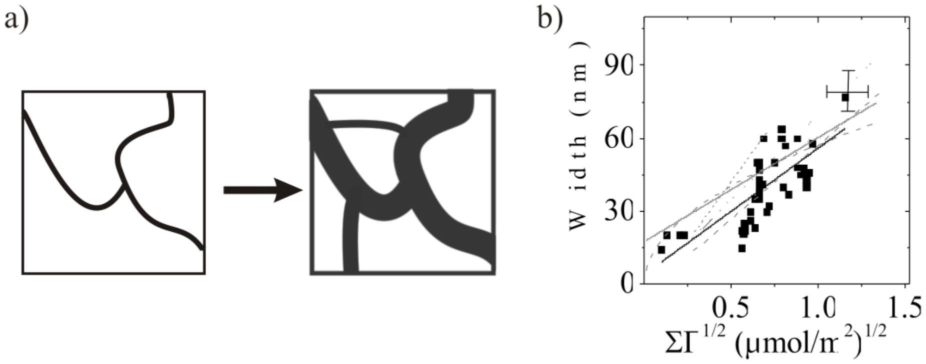

Figure 7-13 a) Schematic draw of width increase, b) width versus square root of amount of material per area

Height: The height of the nanoribbons is approximately 1 nm. The height of the structure increases just when a new layer is formed, Figure 7-11d. The ratio of height-increase versus the total amount of material per area can be estimated by comparing the maximum height of the CuPc film and the total amount of material per area (*ΣΓ*). The ratio of height-increase (R_H) versus the total number of material per area (*ΣΓ*) is defined to the first approximation linearly as:

$$R_H = \frac{\Delta(H)}{\Delta\sqrt[2]{(\Sigma\Gamma)}} \tag{7-18}$$

Δ(H) is the increase in maximum height (*H*) from Figure 7-11d. From the linear fit of the height versus number of molecules per area, the ratio of height-increase is:

$$R_H \approx 1\ [\mu mol^{-1/2}] \qquad (7\text{-}19)$$

Notably, the growth in lateral direction (length and width) is much larger than growth in height (formation of a new layer). In lateral direction growth in length is much more favorable than in width: $R_L > R_W > R_H$. Hence first a mesh forms (significant length growth) and then the width of the nanoribbons in the mesh increases. Later the next layers form.

Nucleation: two kind of nucleation can be defined regarding AFM images. Especially in a mesh, nanoribbons of thinner width can be found. Presumably these nanoribbons are formed later than nanoribbons of larger width.

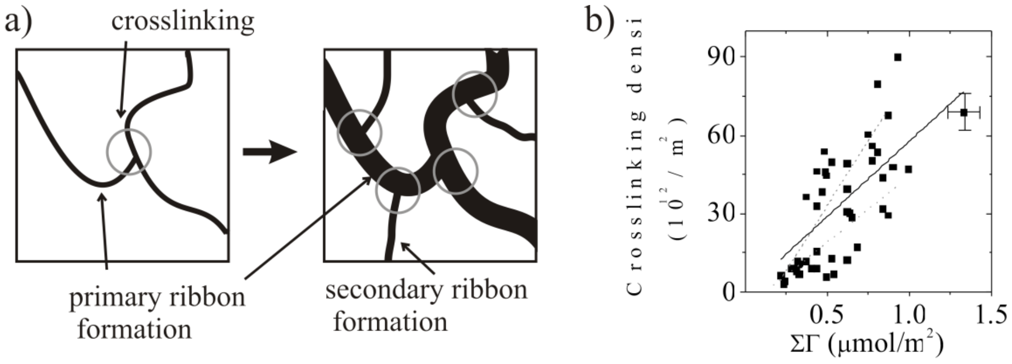

Figure 7-14 a) Schematic draw of ribbon formation, b) crosslinking density versus of amount of material per area

The first nuclei form after supersaturation and grow immediately into nanoribbons. This nucleation is called here primary ribbon formation.

After the primary ribbon formation, these ribbons grow unimpeded. When the distance between the growth-front is comparatively large, and the enrichment rate is high, the diffusion is eventually not effective enough to transport CuPcs to growth front. Due to the local enrichment, new nuclei form on the substrate. This nucleation is called here secondary ribbon formation.

Due to secondary ribbon formation, by increasing the amount of material per area, the numbers of nuclei increases, too, see Figure 7-14.

7.2.2 Discussion on the formation of CuPc nanoribbons

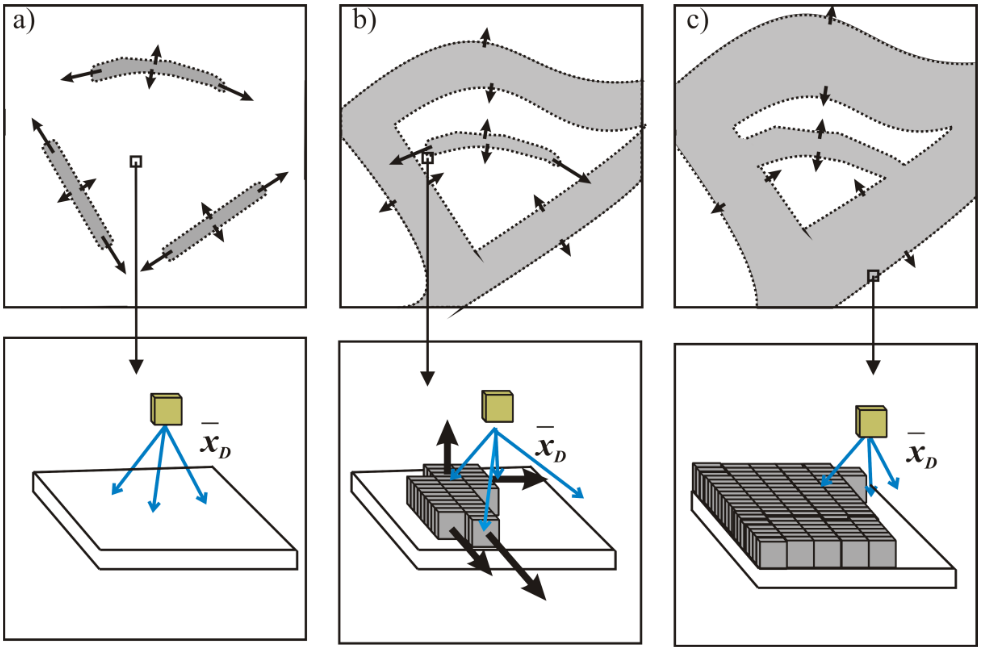

Figure 7-15) Schematic of nanoribbon formation at submonolayer ($\bar{x}_D$: diffusion length)

R_L, R_w, R_H ratios show that when the nuclei form, the aggregation of CuPc molecules in length is the most favorable. When the first nuclei form, they grow in length faster than width, in width faster than height, and thus form nanoribbons (primary ribbon formation), see Figure 7-15a. By increasing the concentration the length and width of primary ribbons increase and also secondary ribbons form, Figure 7-15b and 7-15c. The nanoribbons connect and form a mesh. With further increasing the amount of material the width of nanoribbons grow 7-16a.

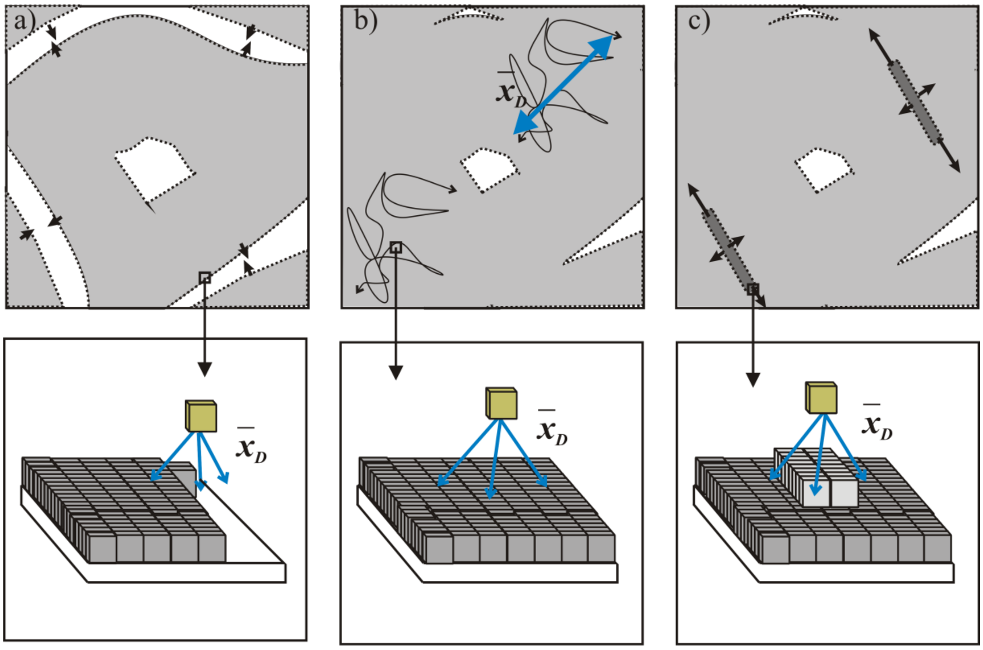

Figure 7-16) Schematic draw of nanoribbons formation at new layer ($\bar{x}_D$: diffusion length)

Eventually the first layer is partially filled, Figure 7-16a, the distance between the growth-fronts increases, Figure 16-7b. Again comparative diffusive transport and local enrichment cause secondary ribbon formation on the first layer, Figure 7-16c.

7.2.3 Discussion on the intermolecular interaction of CuPc and substrate

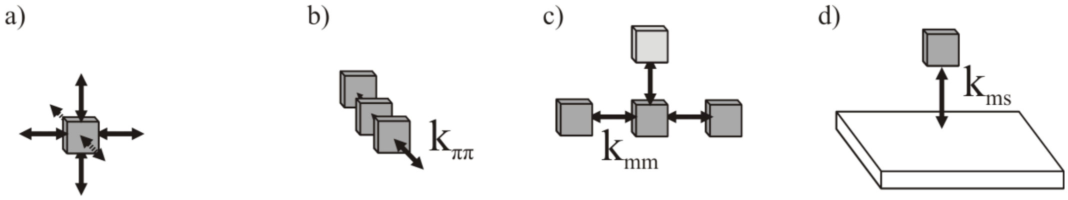

Figure 7-17) Schematic draw of the interactions of CuPc-molecules by adsorption on the substrate

Regarding the geometry of CuPc molecules, 6 directions can be envisioned for the interactions of the molecule with the environment, Figure 7-17a. The interaction vertical to the plane of the disc shaped molecule are mainly π-π interaction, named $k_{\pi\pi}$, Figure 7-17b. The interactions parallel to the plane of the molecule mainly van der Waals, called here k_{mm}, Figure 7-17c. For a molecule in a uniform environment, the van der Waals interactions are of the same strength. For CuPc adsorbed onto the SiO_2 substrate, the molecule interact with the substrate, this interaction is called here k_{ms}, Figure 7-17d.

The k values define the strength of the interaction and thus determine the shape of the aggregates. For example, if all interactions were similar, the molecule would aggregate in all direction with the same probability and form bulky aggregates with the same height, width and length. For CuPc molecules the interaction along the stacking axis is mainly of π-π type and is the strongest (compared with van der Waals). It is more favorable for CuPc molecules to stand and attach face to face together (mainly π-π) rather than to lie on the substrate (mainly van der Waals). Therefore, it is expected that the molecules stand on the substrate, build stacks and grow in the stacking direction faster. Based on this and the fact that the solution is supersaturated, the nucleation and growth scenario is as follows.

When a single stack forms on the substrate, it grows immediately. A second stacks forms parallel to that and grows further. A bundle of these stacks forms nanoribbons. The primary ribbon formation is when the first nuclei are formed and grow into ribbons. When the diffusion is not enough to transport the molecules to growth fronts, local enrichment causes new nucleation (here called secondary ribbon formation).

The ribbons grow in length and width until they form a mesh. In a mesh the width grow further by stacking CuPc molecules. Furthermore, new nuclei (secondary ribbon formation) form and grow. As the CuPc ribbons grow further, the mesh will be partially filled and the distance between the growth front increases. Eventually the diffusion is not effective enough to transport the molecule to growth front. A local enrichment causes nucleation onto the first layer and formation of the second layer. The growth of nanoribbons in the second layer and formation of the upper layers follows similar scenario.

7.3 Summary and conclusion

The mechanism of the formation of CuPc nanoribbons from spin casted CuPc/TFA solution in ambient temperature is investigated and explained. Based on the spin casting theory (the approximation of the binary mixture of an ideal (Newtonian) volatile liquid and nonvolatile solute) the important parameters (e.g. concentration profile) influencing nucleation and growth were calculated. Accordingly the nucleation and growth scenario is developed.

The coverage calculated from spin casting theory was in agreement with coverage from AFM images, which proves the validity of the theory. Parameters like diffusion, concentration variation with time were estimated for spin casted CuPc/TFA solution. Supposedly, after the supersaturation of the solution, the nucleation starts near the substrate by aggregation of CuPc molecules into the substrate.

The growth rate of nanoribbons on SiO_2 substrate in length is larger than in width, and both are larger than in height. After nucleation, CuPc aggregates grow in length faster than in width. Formation of a new layer is delayed until the first layer is approximately filled up. In that case the distances between the growth fronts increase and the diffusion is not effective enough to move the molecules to the free areas of the first layer. The concentration increases locally on the first layer and new layers forms.

Based on a solute-solute and solute-substrate interaction model, the mechanism of the growth is discussed. Due to the strong π-π interaction (between the molecules along the molecular stacks), the growth in length is the most favorable. This leads to a faster growth in length. For a new layer formation, there is a threshold in the amount of material per area which is the largest in first layer (near the substrate). The interaction with substrate (perpendicular to molecular stacks) is stronger than the interaction with molecules in upper layer. As a result the threshold in the amount of material per area in the first layer is the largest. The strength of the interaction with the substrate decreases with increasing the distance to the substrate. Thus upper layers have a smaller coverages and the cross-section of the multilayer film has a pyramidal shape.

8. Application of Copper Phthalocyanine from Solution in Organic Solar Cells

Chapter overview: The unsubstituted CuPc layer prepared via wet-deposition, spin casting and drying from a TFA solution was applied as a donor layer in an OSC. The other layers are formed by established vacuum evaporation. For the first time that unsubstituted CuPc molecular film deposited via spin casting is used in an OSC. In this chapter I report on the preparation, structural characterization, and device performance of this OSC prepared via a combination of solution and vacuum processing.

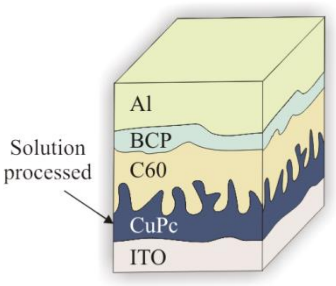

Figure 8-1) Schematic architecture of OSCs prepared by a hybrid solution/vacuum-process. The CuPc electron donor film is prepared by wet-deposition from solution. The other layers are prepared by vacuum deposition.

The OSC structure was maintained intentionally as simple as possible to study the parameters influencing the OSC function concerning solution processed CuPc molecular films. Without using PEDOT:PSS or blending C60, a comparable PCE of up to 0.5% was obtained by improving the CuPc molecular film property. The resulting cell architecture is shown schematically in Figure 1.

The results are published in “Thin Solid Films” [187].

8.1 CuPc films from solution

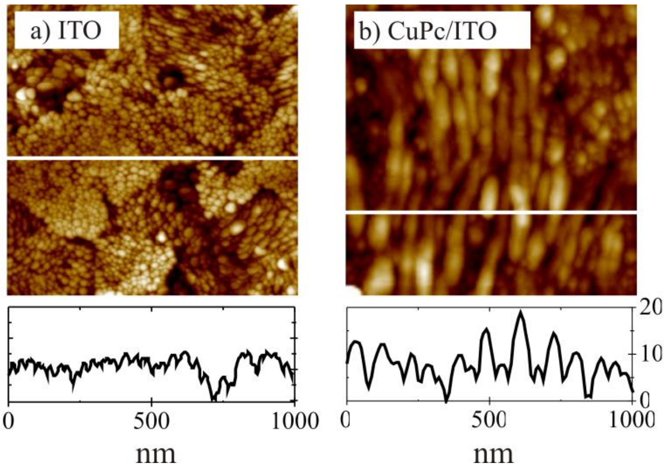

Figure 8-2) AFM images of the morphologies of a) bare ITO substrate, b) CuPc molecular film deposited by single drop spin casting onto the ITO substrate from 1.7×10^{-3} mol·L^{-1} CuPc/TFA solution.

ITO has a much higher roughness (R_a> 5nm, see Figure 8-2a) in comparison with SiO_2 (R_a<0.2 nm). Despite the roughness of the underlying ITO template one can see that the CuPc forms fiber structures. The CuPc morphology on ITO differs from the morphology on SiO_2. On both substrates columnar aggregates of CuPc are formed. On SiO_2 homogeneous coverages of nanoribbon shaped aggregates with a height of ~1nm were discovered. On ITO fiber shaped aggregates of CuPc are present with a height of some 10 nm. In the µm range the coverage is not homogeneous. AFM image of Figure 8-2b is from the same sample of CuPc/TFA spin coated on ITO (1.7×10^{-3} mol·L^{-1}) .The aggregates of CuPc on ITO obtained by single and multiple drop spin casting (each drop is added after the film is dried) are also different. Two distinctly different types of CuPc aggregates are found. With CuPc concentrations significantly below the saturation limit and single drop deposition the CuPc forms fiber-like aggregates. These aggregates are favorable for the OSC performance. With concentrations approaching the saturation limit or with multiple drop deposition also large micron size aggregates are found. These aggregates do not contribute to the OSC efficiency, they even deteriorate the performance. Nevertheless, with multi drop deposition it is possible to obtain significantly higher coverages with the preferred ribbon like aggregates with a lower portion of micron size aggregates than via single drop preparations with any CuPc concentration.

8.2 Morphologies of the surfaces buried within a hybrid solution/vacuum-processed OSC

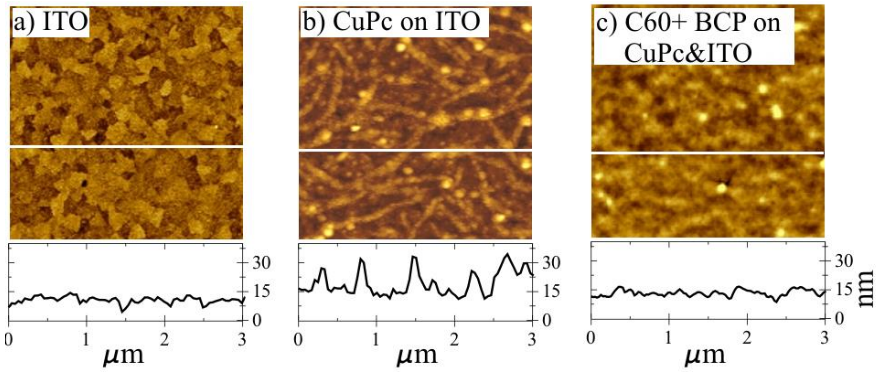

Figure 8-3) AFM images of the morphologies of buried interfaces of the hybrid wet/vacuum prepared OSC: a) bare ITO substrate, b) CuPc molecular film deposited by spin casting onto the ITO substrate from 1.7×10^{-3} $\mathrm{mol\cdot L^{-1}}$ CuPc/TFA solution (20 drop deposition, RT, 35rps), c) C60 and BCP film on surface (b) prepared by vacuum deposition.

Figure 8-3a presents the surface morphology of the ITO/air surface with its typical polycrystallinity and surface roughness. Figure 8-3b shows the surface morphology of a wet deposited CuPc layer on top of the ITO. Figure 8-3c shows the surface morphology of the film of BCP and C60, covering the CuPc layer. The surface is smoother than that of Figure 8-3b. Obviously the evaporated BCP and C60 covers the CuPc ribbons but also fills up the holes between them.

8.3 Device performance of the hybrid solution/vacuum-processed OSCs

Figure 8-4 presents the current-voltage characteristics of OSCs with different CuPc layer thicknesses.

The power-conversion efficiency (PCE) of OSCs without CuPc layer is negligible (case (i)). With increasing CuPc layer thickness, the PCE is 0.2% for a thickness of ~5-7 nm (ii) and 0.3% for ~13 nm (iii). With a CuPc-coverage of ~18 nm the PCE reaches ~0.5% (iv). This value is nearly twice as large as the one for hybrid solution/vacuum prepared OSCs with substituted Pcs [19]. For even higher CuPc layer thickness of 25-30 nm (v) the PCE again drops to ~0.15%.

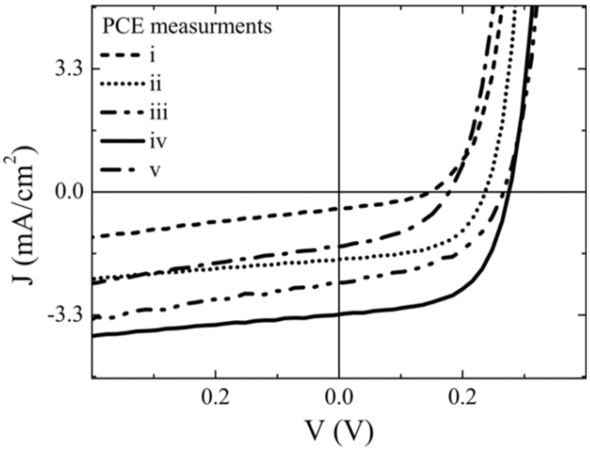

	film d(nm)	FF%	V_{OS}(V)	J_{SC} (mA/cm^2)	PCE%
i	0	36	0.15	0.45	0.03
ii	~5-7	54	0.24	1.8	0.2
iii	~13	50	0.26	2.4	0.3
iv	~18	55	0.28	3.3	0.5
v	~25-30	40	0.18	1.45	0.15

Figure 8-4) I-V characteristics of various OSCs with CuPc electron-donor films of different coverage/thicknesses that were wet-deposited from CuPc/TFA-solution. i: no CuPc film (just the solvent, TFA, is spin coated onto ITO. Using bare ITO without TFA led to the same results); ii: single step (1.7×10^{-3} mol·L^{-1}), iii, iv and v: multi-step spin coated CuPc film with 35rps (iii: 100 drops, 6.5×10^{-4} mol·L^{-1}; iv: 20 drops, 1.7×10^{-3} mol·L^{-1}; v: 100 drops, 1.7×10^{-3} mol·L^{-1}). The coverages are derived from AFM-scratching experiments and reflect the effective film thickness of a closed CuPc layer. The vacuum deposited parts of the OSCs are all identical.

The findings can be explained by a combination of optical and structural contributions. By increasing the coverage with CuPc, more light will be absorbed. This will increase the efficiency because the absorbance of CuPc films only a few tens of nm thick is still quite low (~%10) despite the very high specific absorption coefficient of CuPc (~105 cm^{-1}) [188]. Thus, for thin CuPc films a large amount of light is not absorbed, the PCE is therfore low. With increasing film thickness more photons get absorbed and converted, so the PCE increases [189]. However, as the CuPc coverage increases, also the layer structure changes. In this case, in particular, an increasing amount of large, micron-sized CuPc crystals/aggregates were found. In Figure 8-5 the optical image of the CuPc surface for each type of OSC is presented. The light-grey areas are homogeneous coverages of the CuPc film with a morphology similar to the AFM image of Figure 8-2b. The dark grey areas show large aggregates. These aggregates are typically more than 300 nm in height and their size increases in width with every spin casting step. Large aggregates are absent in case (ii), they cover ≈5% of the area in case (iii), ~10% in case (iv), and ~50% in case (v), see supporting information. The large aggregates do not contribute to the power conversion [108]. Excitons produced within the aggregates in most cases cannot reach the interface within their life time and recombine internally [189, 190]. Thus charge generation is inefficient. In addition, the large aggregates may even reduce the efficiency of the adjacent film with the CuPc nano-bundle structure by changing its interface and thus influencing the charge separation [191, 192].

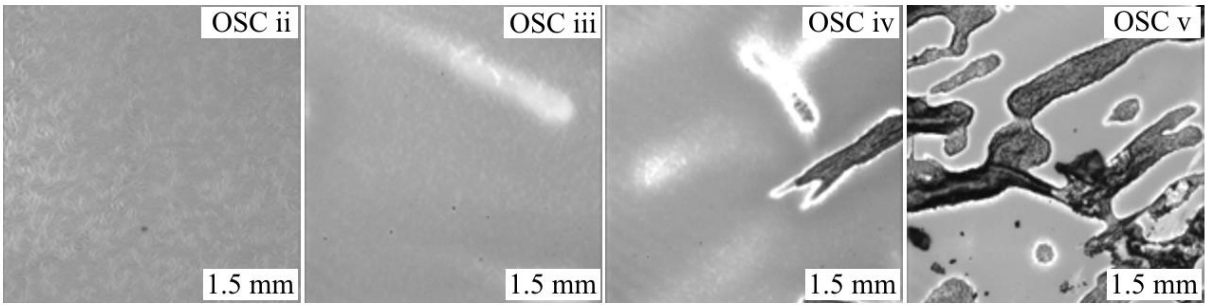

Figure 8-5) Optical images of CuPc films spin coated from a solution of CuPc/TFA by single and multi-step spin casting with 35 rps. The grey areas are covered with CuPc film with the ribbon morphology as described in the manuscript. The dark areas are large aggregates with thickness beyond 300 nm.

8.4 Summary and conclusions

In this chapter the preparation, structural investigation, and performance of bilayer heterojunction OSCs whose absorption layer consists of CuPc nanoribbons is reported. The CuPc-ribbon coverage is, however, less than 10 nm thick resulting in a low overall absorbance. To some degree this drawback has been overcome by multi-drop spin casting which increases the amount of deposited Pc. However, multi-drop spin casting under ambient conditions also leads to an increasing amount of unfavorable, large CuPc aggregates. For cells with optimum performance the CuPc layer absorbance is only about 0.1. This is the main cause for the rather low cell efficiency of 0.5%. A substantial increase of the CuPc coverage respectively overall absorbance without unfavorable large CuPc aggregates appears quite feasible by multi-step spin casting under optimized nucleation and growth conditions (e.g., elevated temperatures, different solvents respectively solvent mixtures). Alternatively one might also increase the overall absorbance by adding nano-aggregates [193], see appendix 9.

9. Overall summary and conclusions

Organic solar cells (OSC) are interesting as cost-efficient alternative to conventional solar cells. In heterojunction OSC unsubstituted metal phthalocyanines (Pc) are used as excellent electron donating molecules. Usually OSCs with Pcs are produced by vapor deposition, although solution based deposition (like spin casting) is cheaper and offers more possibilities to control the structure of the film. The nanostructure of the film determines the performance of OSC. Several parameters (like temperature, solvent, etc.) affect the self-organized structure formation in the nucleation and growth process in solution. The reason why vapor deposition is still preferred is the poor solubility of the metal-phthalocyanines in most common solvents. Furthermore the process of nucleation and growth of Pc from solution is not well-understood. For the preparation of Pc films from solution, it is necessary to find appropriate solvents and to assess the solution deposition techniques, such as dip coating and spin casting. It is necessary to understand the nucleation and growth process leading to aggregation/precipitation.

In this thesis, the solubility of 8 different metal phthalocyanines was studied, the solubility limit in 28 different solvents was determined, and the chemical stability of these solutions was analyzed. Out of this set of 224 solutions, 10 solutions were selected, that showed promising properties favorable for OSC assembly. These properties include good solubility of the Pc's ($> 10^{-3}$ mol L^{-1}), good chemical stability of the solutions (> 1 week), and a sufficiently high evaporation rate of the solvent for forming a dry film under ambient conditions. The 10 solutions were used in an evaluation study of film formation by solution deposition. The morphology of the resulting thin films was characterized using atomic force microscopy. As a result out of the 10 Pc solution, copper phthalocyanine, CuPc, dissolved in Trifluoroacetic acid, TFA, was chosen as a model system and as most promising for an in depth analysis due to its optimum combination of film morphology, solubility limit, and chemical stability.

In solution, UV-Vis absorption spectroscopy and Cryo-TEM proved that CuPc is dissolved by TFA homogeneously and that aggregates are absent in these solutions. Upon evaporation of the solvent in the solution deposition process under ambient condition, CuPc molecules aggregate into nanoribbons. These nanoribbons are formed from bundles of stacks of the disc-like CuPc molecule parallel to the surface with individual CuPc molecules standing upright. Notably, the length and width of the nanoribbons depend on the initial concentration of the CuPc solution and on the preparation temperature. At 70°C to 80°C, discrete nanorod-like aggregates of up to 15 nm height are formed. At 0°C, a multilayer film of interconnected nanostripes assembles from solution. At room temperature, CuPc molecules aggregate into nanoribbons of ~ 1 nm thickness (~ height of CuPc molecule) deposited onto the substrate (SiO_2, ITO,…). The length and width of these nanoribbons depend on the initial concentration of the CuPc solution. The ribbon formation at ambient temperature can be divided into three regimes: (1) formation of individual, isolated ribbons, (2) formation of an interconnected mesh of nanoribbons, and (3) formation of multilayers of nanoribbons. These results were obtained by an elaborate atomic force microscopy (AFM), UV-Vis-spectroscopy, FTIR-spectroscopy, and X-ray diffraction (XRD) investigation.

The nanoribbons can be produced by drop casting, dip coating, and spin casting. For a further in depth analysis, CuPc nanoribbons produced by spin casting at room temperature were selected as a model system to study the nucleation and growth mechanism. The coverage of nanoribbons measured from AFM images is in agreement with the coverage calculated from spin casting theory. The theory assumes an ideal binary mixture of nonvolatile solute and evaporative solvent. Right after the deposition of the solution on the rotating substrate the liquid film thins mainly fluid-dynamically and due to spin-off. After a transition point, where hydrodynamic and evaporative thinning is equal, the thinning is dominated by evaporation of solvent from liquid-vapor interface. This increases the solute (Pc) concentration. The Pc concentration gradient in the liquid film is determined by the competition between the evaporation rate and diffusion, which is characterized by the Sherwood number. It is shown that in case of CuPc and TFA, the Sherwood number is << 1 i.e., the concentration with the thinning film is almost homogeneous. While the solvent evaporates, the solution becomes eventually supersaturated. After supersaturation CuPc molecules aggregate and form individual nuclei. These nuclei grow into ribbons like aggregate at the substrate surface.

Based on the spin casting theory and intermolecular interactions, a model of the nucleation and growth of CuPc nanoribbons from a supersaturated solution on the substrate is developed. In this model nucleation and growth is discussed based on the enrichment and transport of CuPc in supersaturated TFA solution. The model shows that the typical size of the pattern in lateral dimension is given by the diffusion/transport length of the system in μm range. The strong π-π interaction between the molecules along the stacking axis compared to the weaker van der Waals interaction leads to the stack formation and finally to the nanoribbons.

Finally, a functioning hybrid vacuum/solution processed OSC is produced with CuPc nanoribbons spin casted from solution. Although due to limitations in thickness of the CuPc layer the light absorbance was low (up to ~ 0.1), a conversion efficiency of up to 0.5% could be realized. This efficiency is comparable to the one of OSCs produced with functionalized phthalocyanine molecules. It can be envisioned, that the efficiency of CuPc based OSC's can be improved by tailoring the structures deposited from solution via a rational approach as described in this thesis.

References

1. Yue, D., P. Khatav, F. You and S.B. Darling, *Deciphering the uncertainties in life cycle energy and environmental analysis of organic photovoltaics.* Energy & Environmental Science, 2012. **5**(11): p. 9163-9172.

2. Steim, R., *The Impact of Interfaces on the Performance of Organic Photovoltaic Cells*. 2010: KIT Scientific Publishing.

3. Benanti, T. and D. Venkataraman, *Organic Solar Cells: An Overview Focusing on Active Layer Morphology.* Photosynthesis research, 2006. **87**(1): p. 73-81.

4. Yang, F. and S.R. Forrest, *Photocurrent Generation in Nanostructured Organic Solar Cells.* Acs Nano, 2008. **2**(5): p. 1022-1032.

5. Yang, F., K. Sun and S.R. Forrest, *Efficient Solar Cells Using All-Organic Nanocrystalline Networks.* Advanced Materials, 2007. **19**(23): p. 4166-4171.

6. Kadish, K.M., K.M. Smith and R. Guilard, *The Porphyrin Handbook: Applications of phthalocyanines*. 2003: Academic Press.

7. Dent, C.E. and R.P. Linstead, *Phthalocyanines part IV Copper phthalocyanines.* Journal of the Chemical Society, 1934: p. 1027-1031.

8. Turek, P., P. Petit, J.J. Andre, J. Simon, R. Even, B. Boudjema, G. Guillaud and M. Maitrot, *A new series of molecular semiconductors: phthalocyanine radicals.* Journal of the American Chemical Society, 1987. **109**(17): p. 5119-5122.

9. Beaumont, N., I. Hancox, P. Sullivan, R.A. Hatton and T.S. Jones, *Increased efficiency in small molecule organic photovoltaic cells through electrode modification with self-assembled monolayers.* Energy & Environmental Science, 2011. **4**(5): p. 1708-1711.

10. Singh, V.P., B. Parsarathy, R.S. Singh, A. Aguilera, J. Anthony and M. Payne, *Characterization of high-photovoltage CuPc-based solar cell structures.* Solar Energy Materials and Solar Cells, 2006. **90**(6): p. 798-812.

11. McIntosh, A.R., A. Siemiarczuk, J.R. Bolton, M.J. Stillman, T.F. Ho and A.C. Weedon, *Intramolecular Photochemical Electron Transfer. 1. EPR and Optical Absorption Evidence for Stabilized Charge Separation in Linked Porphyrin-Quinone Molecules.* Journal of the American Chemical Society, 1983. **105**(25): p. 7215-7223.

12. Jian-Fei, Y., W. Zhi-Ming, T. Hui-Ling, L. Xian, W. Yao, S. Yuan-Jie and P. Cong. *The investigation of the formaldehyde gas sensor based on organic thin-film-transistors*. in *2010 International Conference on Apperceiving Computing and Intelligence Analysis (ICACIA 2010)*. 2010. Chengdu, China: Ieee.

13. Klug, A., K. Schmoltner and E.J.W. List, *Organic field-effect transistors applicable for gas and ion detection*, in *Organic Semiconductors in Sensors and Bioelectronics Iii*, R. Shinar and I. Kymissis, Editors. 2010, Spie-Int Soc Optical Engineering: Bellingham.

14. van Ewyk, R.L., A.V. Chadwick and J.D. Wright, *Effects of oxygen, nitrogen dioxide and trifluoroborane on photoconductivity of perylene and phthalocyanine single crystals.* Journal of the Chemical Society, Faraday Transactions 1: Physical Chemistry in Condensed Phases, 1981. **77**(1): p. 73-79.

15. Mohammed, R.A.C.a.K.A., *Gas sensitivity of some metal phthalocyanines.* Journal of Physics D: Applied Physics, 1988. **21**(1): p. 154.

16. Rapp, L., S. Ne non, A.P. Alloncle, C. Videlot-Ackermann, F. Fages and P. Delaporte, *Multilayer laser printing for Organic Thin Film Transistors.* Applied Surface Science, 2011. **257**(12): p. 5152-5155.

17. Kim, H.G., J.S. Jang, S.T. Hur, S.W. Choi, S.S. Kim, H. Tada, H. Takezoe and K. Ishikawa, *Thin-film field-effect transistors of copper phthalocyanine on a rubbed polyethersulfone.* Thin Solid Films, 2011. **519**(6): p. 2011-2014.

18. Madru, M., G. Guillaud, M.A. Sadoun, M. Maitrot, C. Clarisse, M.L. Contellec, J.J. André and J. Simon, *The first field effect transistor based on an intrinsic molecular semiconductor.* Chemical Physics Letters, 1987. **142**(1-2): p. 103-105.

19. Schunemann, C., C. Elschner, A.A. Levin, M. Levichkova, K. Leo and M. Riede, *Zinc phthalocyanine - Influence of substrate temperature, film thickness, and kind of substrate on the morphology.* Thin Solid Films, 2011. **519**(11): p. 3939-3945.

20. Gregory, P., *Industrial applications of phthalocyanines.* Journal of Porphyrins and Phthalocyanines, 2000. **4**(4): p. 432-437.

21. Gu, D., Q. Chen, J. Shu, X. Tang, F. Gan, S. Shen, K. Liu and H. Xu, *Optical recording performance of thin films of phthalocyanine compounds.* Thin Solid Films, 1995. **257**(1): p. 88-93.

22. Pile, D., *View from... 2010 MRS spring meeting: Solar cells stimulate discussion.* Nat Photon, 2010. **4**(6): p. 351-351.

23. Kadish, K.M., K.M. Smith and R. Guilard, *The Porphyrin Handbook: Phthalocyanines : properties and materials*. 2003: Academic Press.

24. Kadish, K.M., K.M. Smith and R. Guilard, *The Porphyrin Handbook: Phthalocyanines: Spectroscopic And Electrochemical Characterization*. 2002: Academic Press.

25. Wöhrle, D. and D. Meissner, *Organic Solar Cells.* Advanced Materials, 1991. **3**(3): p. 129-138.

26. Hoppe, H. and N.S. Sariciftci, *Organic solar cells: An overview.* Journal of Materials Research, 2004. **19**(7): p. 1924-1945.

27. Wolden, C.A., J. Kurtin, J.B. Baxter, I. Repins, S.E. Shaheen, J.T. Torvik, A.A. Rockett, V.M. Fthenakis and E.S. Aydil, *Photovoltaic manufacturing: Present status, future prospects, and research needs.* Journal of Vacuum Science & Technology A, 2011. **29**(3).

28. Benanti, T.L. and D. Venkataraman, *Organic solar cells: an overview focusing on active layer morphology.* Photosynthesis research, 2006. **87**: p. 73-81.

29. Forrest, S.R., *The path to ubiquitous and low-cost organic electronic appliances on plastic.* Nature, 2004. **428**(6986): p. 911-918.

30. Li, G., V. Shrotriya, J. Huang, Y. Yao, T. Moriarty, K. Emery and Y. Yang, *High-efficiency solution processable polymer photovoltaic cells by self-organization of polymer blends.* Nature Materials, 2005. **4**: p. 864-868.

31. Ough, E.A., M.J. Stillman and K.A.M. Creber, *Absorption and magnetic circular dichroism spectra of nitrogen homologues of magnesium and zinc phthalocyanine.* Canadian Journal of Chemistry-Revue Canadienne De Chimie, 1993. **71**(11): p. 1898-1909.

32. Nyokong, T., Z. Gasyna and M.J. Stillman, *Phthalocyanine Pi-Cation-Radical species - Photochemical and electrochemical Preparation of (ZnPc -1)+ in solution.* Inorganic Chemistry, 1987. **26**(4): p. 548-553.

33. Rawling, T., C. Austin, F. Buchholz, S.B. Colbran and A.M. McDonagh, *Ruthenium Phthalocyanine-Bipyridyl Dyads as Sensitizers for Dye-Sensitized Solar Cells: Dye Coverage versus Molecular Efficiency.* Inorganic Chemistry, 2009. **48**(7): p. 3215-3227.

34. Zhang, C.X., S. Kaderli, M. Costas, E.-i. Kim, Y.-M. Neuhold, K.D. Karlin and A.D. ZuberbÃ¼hler, *Copper(I)−Dioxygen Reactivity of [(L)CuI]+ (L = Tris(2-pyridylmethyl)amine): Kinetic/Thermodynamic and Spectroscopic Studies Concerning the Formation of Cu−O2 and Cu2−O2 Adducts as a Function of Solvent Medium and 4-Pyridyl Ligand Substituent Variations.* Inorganic Chemistry, 2003. **42**(6): p. 1807-1824.

35. Lever, A.B.P., *The phthalocyanines—molecules of enduring value; a two-dimensional analysis of redox potentials.* Journal of Porphyrins and Phthalocyanines, 1999. **3**(6-7): p. 488-499.

36. Ling, M.M. and Z. Bao, *Thin Film Deposition, Patterning, and Printing in Organic Thin Film Transistors.* Chemistry of Materials, 2004. **16**(23): p. 4824-4840.

37. Zhu, Y., L. Qian, M. Xue, Q. Sheng, Q. Zhang and Y. Liu, *Morphological control of copper phthalocyanine films by protonation-electrophoretic deposition.* Applied Surface Science, 2010.

38. Su, J., M. Xue, N. Ma, Q. Sheng, Q. Zhang and Y. Liu, *Dissolution of copper phthalocyanine and fabrication of its nano-structure film.* Science in China Series B: Chemistry, 2009. **52**: p. 911-915.

39. Shrestha, N.K., H. Kohn, M. Imamura, K. Irie, H. Ogihara and T. Saji, *Electrophoretic Deposition of Phthalocyanine in Organic Solutions Containing Trifluoroacetic Acid.* Langmuir, 2010. **26**(22): p. 17024-17027.

40. Komino, T. and M. Matsuda, *The fabrication method of unsubstituted planar phthalocyanine thin films by a spin-coating technique.* Thin Solid Films, 2009. **518**: p. 688-691.

41. Rajaputra, S., G. Sagi and V. Singh, *Schottky diode solar cells on electrodeposited copper phthalocyanine films.* Solar Energy Materials and Solar Cells, 2009. **93**: p. 60-64.

42. Jung, J.S., J.W. Lee, K. Kim, M.Y. Cho, S.G. Jo and J. Joo, *Rectangular Nanotubes of Copper Phthalocyanine: Application to a Single Nanotube Transistor.* Chemistry of Materials, 2010. **22**: p. 2219-2225.

43. Chintakula, G., S. Rajaputra and V.P. Singh, *Schottky diodes on nanowires of copper phthalocyanine.* Solar Energy Materials and Solar Cells, 2010. **94**: p. 34-39.

44. Chintakula, G., *Schottky Diodes On Copper Phthalocyanine Nanowire Arrays Embedded In Porous Alumina Templates.* 2008.

45. Derouiche, H., H.B. Miled and A.B. Mohamed, *Enhanced performance of a CuPc: PCBM based solar cell using bathocuproine BCP or nanostructured TiO 2 as hole-blocking layer.* Physica Status Solidi (a), 2010. **207**: p. 479-483.

46. Edwards, L. and Gouterma.M, *Porphyrins: 15. Vapor absorption spectra and stability: Phthalocyanines.* Journal of Molecular Spectroscopy, 1970. **33**(2): p. 292-&.

47. Xiao, K., R. Li, J. Tao, E.a. Payzant, I.N. Ivanov, A.a. Puretzky, W. Hu and D.B. Geohegan, *Metastable Copper-Phthalocyanine Single-Crystal Nanowires and Their Use in Fabricating High-Performance Field-Effect Transistors.* Advanced Functional Materials, 2009. **19**: p. 3776-3780.

48. Peumans, P. and S.R. Forrest, *Very-high-efficiency double-heterostructure copper phthalocyanine/C-60 photovoltaic cells.* Applied Physics Letters, 2001. **79**(1): p. 126-128.

49. Adamson, A.W., *Physical chemistry of surfaces*. 1982: J. Wiley.

50. Mer, V.K.L., *Nucleation in Phase Transitions.* Industrial & Engineering Chemistry, 1952. **44**(6): p. 1270-1277.

51. Gibbs, J.W., H.A. Bumstead, R.G. Van Name and W.R. Longley, *The collected works of J. Willard Gibbs*. 1902: Longmans, Green and Co.

52. Ohtaki, H., *Crystallization processes*. 1998: Wiley.

53. Butt, H.J., K. Graf and M. Kappl, *Physics and Chemistry of Interfaces*. 2006: Wiley.

54. Cao, G. and Y. Wang, *Nanostructures and Nanomaterials: Synthesis, Properties, and Applications*. 2010: World Scientific.

55. Jackson, K.A., *Kinetic Processes: Crystal Growth, Diffusion, and Phase Transformations in Materials*. 2006: Wiley.

56. Markov, I.V., *Crystal Growth for Beginners: Fundamentals of Nucleation, Crystal Growth and Epitaxy*. 2003: World Scientific.

57. Kossel, W., *Zur Theorie des Kristallwachstums.* Nachrichten von der Gesellschaft der Wissenschaften zu Göttingen, Mathematisch-Physikalische Klasse, 1927: p. 135-143.

58. Stranski, I.N., *Zur Theorie des Kristallwachstums.* Zeitschrift für physikalische Chemie, 1928. **136**: p. 259.

59. Becker, R. and W. Döring, *Kinetische Behandlung der Keimbildung in übersättigten Dämpfen.* Annalen der Physik, 1935. **416**(8): p. 719-752.

60. Burton, W.K., N. Cabrera and F.C. Frank, *The Growth of Crystals and the Equilibrium Structure of their Surfaces.* Philosophical Transactions of the Royal Society of London. Series A, Mathematical and Physical Sciences, 1951. **243**(866): p. 299-358.

61. Brunauer, S., P.H. Emmett and E. Teller, *Adsorption of Gases in Multimolecular Layers.* Journal of the American Chemical Society, 1938. **60**(2): p. 309-319.

62. Seber, G.A.F. and C.J. Wild, *Nonlinear Regression*. 2005: Wiley.

63. Kisliuk, P., *The sticking probabilities of gases chemisorbed on the surfaces of solids.* Journal of Physics and Chemistry of Solids, 1957. **3**(1–2): p. 95-101.

64. Frumkin, A., *The capillary curve of higher fatty acids and the constitutive equation of the surface layer.* Zeitschrift Fur Physikalische Chemie--Stochiometrie Und Verwandtschaftslehre, 1925. **116**(5/6): p. 466-484.

65. Fowler, R.H., *Adsorption isotherms - Critical conditions.* Proceedings of the Cambridge Philosophical Society, 1936. **32**: p. 144-151.

66. Eres, M.H., D.E. Weidner and L.W. Schwartz, *Three-Dimensional Direct Numerical Simulation of Surface-Tension-Gradient Effects on the Leveling of an Evaporating Multicomponent Fluid.* Langmuir, 1999. **15**(5): p. 1859-1871.

67. Brune, H., *Microscopic view of epitaxial metal growth: nucleation and aggregation.* Surface Science Reports, 1998. **31**(4–6): p. 125-229.

68. Zalc, J.M. and F.J. Muzzio, *Parallel-competitive reactions in a two-dimensional chaotic flow.* Chemical engineering journal, 1999. **72**(3): p. 1053-1069.

69. Turing, A.M., *The Chemical Basis of Morphogenesis.* Philosophical Transactions of the Royal Society of London. Series B, Biological Sciences, 1952. **237**(641): p. 37-72.

70. Chandrasekhar, S., *Hydrodynamic and Hydromagnetic Stability*. 1981: Dover Publications.

71. Boubnov, B.M. and G.S. Golitsyn, *Experimental study of convective structures in rotating fluids.* Journal of Fluid Mechanics, 1986. **167**: p. 503-531.

72. Einstein, A., *Investigations on the Theory of the Brownian Movement*. 1956: Dover Publications.

73. Emslie, A.G., F.T. Bonner and L.G. Peck, *Flow of a Viscous Liquid on a Rotating Disk.* Journal of Applied Physics, 1958. **29**(5): p. 858-862.

74. Meyerhofer, D., *Characteristics of resist films produced by spinning.* Journal of Applied Physics, 1978. **49**(7): p. 3993-3997.

75. Karpitschka, S., C.M. Weber and H. Riegler *Physics of Spin Casting Dilute Solutions*. ArXiv e-prints, 2012.

76. Spiers, R.P., C.V. Subbaraman and W.L. Wilkinson, *Free coating of a Newtonian liquid onto a vertical surface.* Chemical Engineering Science, 1974. **29**(2): p. 389-396.

77. Brinker, C.J., G.C. Frye, A.J. Hurd and C.S. Ashley, *Fundamentals of sol-gel dip coating.* Thin Solid Films, 1991. **201**(1): p. 97-108.

78. Landau, L.D. and B.G. Levich, *Dragging of a Liquid by a Moving Plate.* Acta Physiochim, U.R.S.S.

, 1942. **17**.

79. Stillman, M., J. Mack and N. Kobayashi, *Theoretical aspects of the spectroscopy of porphyrins and phthalocyanines.* Journal of Porphyrins and Phthalocyanines, 2002. **6**(4): p. 296-300.

80. Tang, C.W., *Two layer organic photovoltaic cell.* Applied Physics Letters, 1986. **48**(2): p. 183-185.

81. Braun, A. and J. Tcherniac, *Über die Produkte der Einwirkung von Acetanhydrid auf Phthalamid.* Ber. Dtsch. Chem. Ges., 1907. **40**: p. 2709-2714.

82. DANDRIDGE, A.G., H.A.E. DRESCHER, J. THOMAS and L. Scottish Dyes, *Improvements in and relating to the manufacture and use of colouring matters* 1929.

83. Weickert, J., R.B. Dunbar, H.C. Hesse, W. Wiedemann and L. Schmidt-Mende, *Nanostructured Organic and Hybrid Solar Cells.* Advanced Materials, 2011. **23**(16): p. 1810-1828.

84. Vollhardt, D., T. Gutberlet, G. Emrich and J.H. Fuhrhop, *Dendritic Crystal Growth in N-Dodecylgluconamide. Monolayers at the Air-Water Interface.* Langmuir, 1995. **11**(7): p. 2661-2668.

85. Eastwood, D., L. Edwards, M. Gouterman and J. Steinfeld, *Spectra of porphyrins : Part VII. Vapor absorption and emission of phthalocyanines.* Journal of Molecular Spectroscopy, 1966. **20**(4): p. 381-390.

86. Kumar, G.A., V. Thomas, G. Jose, N.V. Unnikrishnan and V.P.N. Nampoori, *Optical properties of porphyrins in borate glassy matrix.* Materials Chemistry and Physics, 2002. **73**: p. 206-211.

87. Kumar, G.a., J. Thomas, N.V. Unnikrishnan, V.P.N. Nampoori and C.P.G. Vallabhan, *Optical absorption and emission spectral studies of phthalocyanine molecules in DMF.* Journal of Porphyrins and Phthalocyanines, 2001. **5**: p. 456-459.

88. Gouterman, M. *Excited states of porphyrins and related ring systems*. in *Symposium on Excited States of Matter*. 1973. Lubbock, TX, USA: Texas Tech. Univ.

89. Mack, J. and M.J. Stillman, *Assignment of the optical spectra of metal phthalocyanines through spectral band deconvolution analysis and ZINDO calculations.* Coordination Chemistry Reviews, 2001. **219**: p. 993-1032.

90. McHugh, A.J., C. Weiss and Gouterma.M, *Porphyrins .24. energy, oscillator strength, and zeeman splitting calculations (scmo-ci) for phthalocyanine, porphyrins, and related ring-systems.* Theoretica Chimica Acta, 1972. **24**(4): p. 346-&.

91. Schaffer, A.M., Gouterma.M and E.R. Davidson, *Porphyrins XXVIII. Extended Hückel calculations on metal phthalocyanines and tetrazaporphins.* Theoretica Chimica Acta, 1973. **30**(1): p. 9-30.

92. Minor, P.C., M. Gouterman and A.B.P. Lever, *Electronic-spectra of phthalocyanine radical-anions and cations.* Inorganic Chemistry, 1985. **24**(12): p. 1894-1900.

93. Hollebon, B. and M.J. Stillman, *Observation of davydov splitting in mcd spectra of alpha metal-free phthalocyanine.* Chemical Physics Letters, 1974. **29**(2): p. 284-286.

94. Mack, J., S. Kirkby, E.A. Ough and M.J. Stillman, *Ground-state and optical-spectrum of metallophthalocyanine radical-anions from low-temperature magnetic circular-dichroism spectroscopy.* Inorganic Chemistry, 1992. **31**(9): p. 1717-1719.

95. Mack, J. and M.J. Stillman, *Photochemical formation of the anion-radical of zinc phthalocyanine and analysis of the absorption and magnetic circular-dichroism spectral data - assignment of the optical-spectrum of [znpc(-3)](-).* Journal of the American Chemical Society, 1994. **116**(4): p. 1292-1304.

96. Mack, J. and M.J. Stillman, *Assignment of the optical spectra of metal phthalocyanine anions.* Inorganic Chemistry, 1997. **36**(3): p. 413-425.

97. Nyokong, T., Z. Gasyna and M.J. Stillman, *Photochemical formation of ruthenium phthalocyanine PI-cation radical species.* Inorganica Chimica Acta, 1986. **112**(1): p. 11-15.

98. Williamson, B.E., T.C. Vancott, M.E. Boyle, G.C. Misener, M.J. Stillman and P.N. Schatz, *Determination of the Ground State of Manganese. Phthalocyanine in an Argon Matrix Using Magnetic Circular. Dichroism and Absorption Spectroscopy.* Journal of the American Chemical Society, 1992. **114**(7): p. 2412-2419.

99. Jones, J.G. and M.V. Twigg, *Dimerisation and de-dimerisation of ferrous phthalocyanine in DMSO.* Inorganic and Nuclear Chemistry Letters, 1972. **8**(4): p. 305-308.

100. Linßen, T.G. and M. Hanack, *Synthesis, Separation and Characterization of Unsymmetrically Substituted Phthalocyanines.* Chemische Berichte, 1994. **127**(10): p. 2051-2057.

101. Kippelen, B. and J.-L. Bredas, *Organic photovoltaics.* Energy & Environmental Science, 2009. **2**(3): p. 251-261.

102. Peumans, P., S. Uchida and S.R. Forrest, *Efficient bulk heterojunction photovoltaic cells using small-molecular-weight organic thin films.* Nature, 2003. **425**(6954): p. 158-162.

103. Yu, G., J. Gao, J.C. Hummelen, F. Wudl and A.J. Heeger, *Polymer Photovoltaic Cells: Enhanced Efficiencies via a Network of Internal Donor-Acceptor Heterojunctions.* Science, 1995. **270**(5243): p. 1789-1791.

104. Xue, J., B.P. Rand, S. Uchida and S.R. Forrest, *A Hybrid Planar–Mixed Molecular Heterojunction Photovoltaic Cell.* Advanced Materials, 2005. **17**(1): p. 66-71.

105. Scharber, M.C., D. Mühlbacher, M. Koppe, P. Denk, C. Waldauf, A.J. Heeger and C.J. Brabec, *Design Rules for Donors in Bulk-Heterojunction Solar Cells—Towards 10 % Energy-Conversion Efficiency.* Advanced Materials, 2006. **18**(6): p. 789-794.

106. Mutihac, R.-C. and H. Riegler, *Phase Transition Broadening Due to Interfacial Premelting: A New Quantitative Access to Intermolecular Interactions within Submonolayer Films at Solid/Vapor Interfaces.* Langmuir, 2009. **26**(9): p. 6394-6399.

107. Riegler, H. and R. Kohler, *How pre-melting on surrounding interfaces broadens solid-liquid phase transitions.* Nat Phys, 2007. **3**(12): p. 890-894.

108. Peumans, P., A. Yakimov and S.R. Forrest, *Small molecular weight organic thin-film photodetectors and solar cells.* Journal of Applied Physics, 2003. **93**(7): p. 3693-3723.

109. Dumoulin, F., M. Durmus, V. Ahsen and T. Nyokong, *Synthetic pathways to water-soluble phthalocyanines and close analogs.* Coordination Chemistry Reviews, 2010.

110. Chen, Y., M. Hanack, W.J. Blau, D. Dini, Y. Liu, Y. Lin and J.R. Bai, *Soluble axially substituted phthalocyanines: Synthesis and nonlinear optical response.* JOURNAL OF MATERIALS SCIENCE, 2006. **41**(8): p. 2169-2185.

111. Walker, B., C. Kim and T.-Q. Nguyen, *Small Molecule Solution-Processed Bulk Heterojunction Solar Cells†.* Chemistry of Materials, 2010. **23**(3): p. 470-482.

112. Varotto, A., C.-Y. Nam, I. Radivojevic, J. P. C. Tomé, J.A.S. Cavaleiro, C.T. Black and C.M. Drain, *Phthalocyanine Blends Improve Bulk Heterojunction Solar Cells.* Journal of the American Chemical Society, 2010. **132**(8): p. 2552-2554.

113. Schumann, S., R.A. Hatton and T.S. Jones, *Organic Photovoltaic Devices Based on Water-Soluble Copper Phthalocyanine.* Solutions, 2011: p. 4916-4921.

114. Derouiche, H., S. Saidi and A.B. Mohamed, *The Effect of Energy Levels of the Electron Acceptor Materials on Organic Photovoltaic Cells.* Smart Grid and Renewable Energy, 2011. **2**(3): p. 278.

115. AG, J.I., *The NanoWizard AFM Handbook*, 2009, JPK Instruments AG.

116. Schmitz, I., M. Schreiner, G. Friedbacher and M. Grasserbauer, *Tapping-Mode AFM in Comparison to Contact-Mode AFM as a Tool for in Situ Investigations of Surface Reactions with Reference to Glass Corrosion.* Analytical Chemistry, 1997. **69**(6): p. 1012-1018.

117. Wu, W. and C.M. University, *Control, Manipulation, Characterization and Complex Crystallization Behavior of Macromolecular Assemblies*. 2008: Carnegie Mellon University.

118. Pawlak, R., S. Kawai, S. Fremy, T. Glatzel and E. Meyer, *High-resolution imaging of C 60 molecules using tuning-fork-based non-contact atomic force microscopy.* Journal of Physics: Condensed Matter, 2012. **24**(8): p. 084005.

119. Meyer, E., H.J. Hug and R. Bennewitz, *Scanning Probe Microscopy: The Lab on a Tip*. 2003: Springer.

120. *Effect of the tip curvature radius and cone angle*. 2012.

121. *AFM probe characterization*. 2012.

122. Zitzler, L., S. Herminghaus and F. Mugele, *Capillary forces in tapping mode atomic force microscopy.* Physical Review B, 2002. **66**(15): p. 155436.

123. Mathur, A.B., A.M. Collinsworth, W.M. Reichert, W.E. Kraus and G.A. Truskey, *Endothelial, cardiac muscle and skeletal muscle exhibit different viscous and elastic properties as determined by atomic force microscopy.* Journal of Biomechanics, 2001. **34**(12): p. 1545-1553.

124. *SPIP Manual*, 2012, Image Metrology A/S: http://www.imagemet.com/.

125. Zhuravlev, L.T., *The surface chemistry of amorphous silica. Zhuravlev model.* Colloids and Surfaces A: Physicochemical and Engineering Aspects, 2000. **173**(1–3): p. 1-38.

126. Kohli, R. and K.L. Mittal, *Developments in Surface Contamination and Cleaning, Vol. 3: Methods for Removal of Particle Contaminants*. 2011: Elsevier Science.

127. Sulman, E.M. and B.V. Romanovskii, *Catalytic properties of metal phthalocyanines in hydrogen activation.* Uspekhi Khimii, 1996. **65**(7): p. 659-666.

128. Tanaka, S., T. Onishi and K. Tamaru, *Decomposition of Formic Acid over Metal Phthalocyanines.* Bulletin of the Chemical Society of Japan, 1968. **41**(11): p. 2557-&.

129. Deegan, R.D., O. Bakajin, T.F. Dupont, G. Huber, S.R. Nagel and T.A. Witten, *Capillary flow as the cause of ring stains from dried liquid drops.* Nature, 1997. **389**(6653): p. 827-829.

130. Kadish, K.M., K.M. Smith and R. Guilard, eds. *The Porphyrin Handbook: Phthalocyanines: Structural Characterization*. 2003, ACADEMIC PRESS

131. Hoshino, A., *research papers Redetermination of the crystal structure of a-copper phthalocyanine grown on KCl research papers.* Acta Crystallographica Section B, 2003: p. 393-403.

132. Heutz, S., P. Sullivan, B.M. Sanderson, S.M. Schultes and T.S. Jones, *Influence of molecular architecture and intermixing on the photovoltaic, morphological and spectroscopic properties of CuPc-C60 heterojunctions.* Solar Energy Materials and Solar Cells, 2004. **83**(2-3): p. 229-245.

133. Ghani, F., J. Kristen and H. Riegler, *Solubility Properties of Unsubstituted Metal Phthalocyanines in Different Types of Solvents.* Journal of Chemical & Engineering Data, 2012. **57**(2): p. 439-449.

134. Ledson, D.L. and M.V. Twigg, *Acid-base behaviour of phthalocyanine.* Inorganica Chimica Acta, 1975. **13**: p. 43-46.

135. McNaught, A.D. and A. Wilkinson, *IUPAC Compendium of Chemical Terminology*, in *the Gold Book*1997, Blackwell Scientific Publications: Oxford.

136. Kobayashi, N., J. Mack, K. Ishii and M.J. Stillman, *Electronic structure of reduced symmetry peripheral fused-ring-substituted phthalocyanines.* Inorganic Chemistry, 2002. **41**(21): p. 5350-5363.

137. Mack, J. and M.J. Stillman, *Electronic Structure of Metal Phthalocyanine Complexes from the Analysis of the UV-Visible Absorption and Magnetic Circular Dichroism Spectra and Molecular Orbital Calculations*, in *Phthalocyanines: Spectroscopic and Electrochemical Characterization*

2003, Academic Press: San Diego. p. 43-116.

138. Stillman, M.J. and A.J. Thomson, *Assignment of the charge-transfer bands in some metal phthalocyanines. Evidence for the S= 1 state of iron (II) phthalocyanine in solution.* Journal of the Chemical Society-Faraday Transactions Ii, 1974. **70**(5): p. 790-804.

139. Nyokong, T., Z. Gasyna and M.J. Stillman, *Analysis of the absorption and magnetic circular dichroism spectra of zinc phthalocyanine and the .pi.-cation-radical species [ZnPc(1-)]+.* Inorganic Chemistry, 1987. **26**(7): p. 1087-1095.

140. Hush, N.S. and I.S. Woolsey, *Electronic absorption spectra of phthalocyanine monomers and dimers.* Molecular Physics, 1971. **21**(3): p. 465-&.

141. Kumar, a., G. Jose, V. Thomas, N.V. Unnikrishnan and V.P.N. Nampoori, *NIR to UV absorption spectra and the optical constants of phthalocyanines in glassy medium.* Spectrochimica acta. Part A, Molecular and biomolecular spectroscopy, 2003. **59**: p. 1-11.

142. Kumar, G.A., J. Thomas and N. George, *Physical and optical properties of phthalocyanine doped inorganic glasses.* JOURNAL OF MATERIALS SCIENCE, 2000. **5**: p. 2539 - 2542.

143. Kumar, G., *Optical properties of phthalocyanine molecules in cyano acrylate polymer matrix.* Materials Research Bulletin, 2001. **36**: p. 1-8.

144. Berezin, B.D., *Mechanism of dissociation of metalphthalocyanines.* Zhurnal Fizicheskoi Khimii, 1964. **38**(4): p. 850-857.

145. Berezin, B.D., *Dissociation kinetics of stable phthalocyanines in sulfuric acid solutions.* Zhurnal Fizicheskoi Khimii, 1963. **37**(11): p. 2474-2482.

146. Gunsser, W., R. Priess and B. Doscher, *Interactions between copper phthalocyanine and sulfuric-acid.* Inorganica Chimica Acta-Articles, 1980. **40**(2): p. X103-X103.

147. Löbbert, G., *Phthalocyanines*. Ullmann's Encyclopedia of Industrial Chemistry. 2000: Wiley-VCH Verlag GmbH & Co. KGaA.

148. Ellis, J., A.H. Jackson, G.W. Kenner and J. Lee, *Porphyrin nuclear magnetic resonance spectra.* Tetrahedron Letters, 1960. **1**(23): p. 23-27.

149. Hanke, W., *Katalyse an Phthalocyaninen. II. Ameisensäuredampfzerfall an polymerem Kupfer-Phthalocyanin und die Bedeutung des elektronischen Faktors.* Zeitschrift für anorganische und allgemeine Chemie, 1966. **347**(1-2): p. 67-81.

150. Hanke, W., *Katalyse an Phthalocyaninen. I. Ameisensäuredampfzerfall an Metall-Phthalocyaninen.* Zeitschrift für anorganische und allgemeine Chemie, 1966. **343**(3-4): p. 121-130.

151. Ogata, Y., K. Marumo and T. Kwan, *On the Interaction of Oxygen with Cobalt Phthalocyanine in Solution as investigated by ESR* Chemical & Pharmaceutical Bulletin, 1969. **17**(6): p. 1194-&.

152. Gasyna, Z., W.R. Browett and M.J. Stillman, *Pi-cation-radical formation following visible-light photolysis of porphyrins in frozen solution using alkyl chlorides or quinones as electron-acceptors.* Inorganic Chemistry, 1985. **24**(15): p. 2440-2447.

153. Kronenberg, N.M., M. Deppisch, F. Würthner, H.W.a. Lademann, K. Deing and K. Meerholz, *Bulk heterojunction organic solar cells based on merocyanine colorants.* Chemical communications (Cambridge, England), 2008: p. 6489-91.

154. Nyokong, T., Z. Gasyna and M.J. Stillman, *Photooxidation of Phthalocyanines. Photoinduced Reactivity of the Triplet State.* Acs Symposium Series, 1986. **321**: p. 309-327.

155. Ough, E.A. and M.J. Stillman, *Analysis of the Absorption and Magnetic Circular Dichroism Spectra of Low Spin (S = l/2). Iron(II1) Phthalocyanine.* Inorganic Chemistry, 1995. **34**(17): p. 4317-4325.

156. Ough, E.A. and M.J. Stillman, *Analysis of the absorption and magnetic circular dichroism spectra of iron(II) phthalocyanine.* Inorganic Chemistry, 1994. **33**(3): p. 573-583.

157. Lever, A.B.P., S.R. Pickens, P.C. Minor, S. Licoccia, B.S. Ramaswamy and K. Magnell, *Charge-transfer spectra of metallophthalocyanines - correlation with electrode-potentials.* Journal of the American Chemical Society, 1981. **103**(23): p. 6800-6806.

158. Ough, E., Z. Gasyna and M.J. Stillman, *Photochemical, electrochemical, and chemical formulation of the. pi. -cation-radical species of magnesium phthalocyanine. Analysis of the absorption and MCD spectra of (MgPc(-1)).* Inorganic Chemistry, 1991. **30**(10): p. 2301-2310.

159. Barraclough, C.G., R.L. Martin, S. Mitra and R.C. Sherwood, *Paramagnetic Anisotropy, Electronic Structure, and Ferromagnetism in Spin S = (3/2) Manganese(II) Phthalocyanine.* The Journal of Chemical Physics, 1970. **53**(5): p. 1638-1642.

160. Rosswurm, H., R. Haevecker and A. Doiwa, *Katalyse an organischen Halbleitern. I. Ameisensäuredampfzerfall an Phthalocyaninen.* Zeitschrift für anorganische und allgemeine Chemie, 1967. **350**(1-2): p. 1-8.

161. Braterman, P.S., R.C. Davies and R.J.P. Williams, *The Properties of Metal-Porphyrin and Similar Complexes*. Advances in Chemical Physics. 1964: John Wiley & Sons, Inc. 359-407.

162. Lever, A.B.P. and P.C. Minor, *Solvent dependence of phthalocyanine redox equilibria.* Advances in Molecular Relaxation and Interaction Processes, 1980. **18**(2): p. 115-126.

163. Dolotova, O.V., N.I. Bundina, O.L. Kaliya and E.A. Lukyanets, *Manganese phthalocyanine coordination chemistry: recent results and present status.* Journal of Porphyrins and Phthalocyanines, 1997. **1**(4): p. 355-366.

164. Mack, J. and M.J. Stillman, *Band deconvolution analysis of the absorption and magnetic circular-dichroism spectral data of znpc(-2) recorded at cryogenic temperatures.* Journal of Physical Chemistry, 1995. **99**(20): p. 7935-7945.

165. Bruder, I., J. Schöneboom, R. Dinnebier, A. Ojala, S. Schäfer, R. Sens, P. Erk and J. Weis, *What determines the performance of metal phthalocyanines (MPc, M=Zn, Cu, Ni, Fe) in organic heterojunction solar cells? A combined experimental and theoretical investigation.* Organic Electronics, 2010. **11**(3): p. 377-387.

166. Achar, B.N. and K.S. Lokesh, *Studies on polymorphic modifications of copper phthalocyanine.* Journal of Solid State Chemistry, 2004. **177**(6): p. 1987-1993.

167. Sharp, J.H. and M. Abkowitz, *Dimeric structure of a copper phthalocyanine polymorph.* The Journal of Physical Chemistry, 1973. **77**(4): p. 477-481.

168. Knudsen, B.I., *Copper Phthalocyanine: Infrared Absorption Spectra of Polymorphic Modifications.* Acta Chemica Scandinavica, 1966. **20**(5): p. 1344.

169. Lebedeva, N., E. Mal'kova and A. V'yugin, *Polymorphism and molecular metal phthalocyanine complexes.* Review Journal of Chemistry, 2012. **2**(1): p. 20-50.

170. Brown, C.J., *Crystal structure of [small beta]-copper phthalocyanine.* Journal of the Chemical Society A: Inorganic, Physical, Theoretical, 1968: p. 2488-2493.

171. Robertson, J.M., *An X-ray study of the structure of the phthalocyanines Part I The metal-free, nickel, copper, and platinum compounds.* Journal of the Chemical Society, 1935: p. 615-621.

172. Singh, S., S.K. Tripathi and G.S.S. Saini, *Optical and infrared spectroscopic studies of chemical sensing by copper phthalocyanine thin films.* Materials Chemistry and Physics, 2008. **112**(3): p. 793-797.

173. Xu, H.-B., H.-Z. Chen, W.-J. Xu and M. Wang, *Fabrication of organic copper phthalocyanine nanowire arrays via a simple AAO template-based electrophoretic deposition.* Chemical Physics Letters, 2005. **412**(4–6): p. 294-298.

174. Lin, M.-J., X. Fang, M.-B. Xu and J.-D. Wang, *The effect of protonation on the spectra and stabilities of alkoxyl substituted phthalocyaninatometals.* Spectrochimica Acta Part A: Molecular and Biomolecular Spectroscopy, 2008. **71**(4): p. 1188-1192.

175. Bamfield, P., *Chromic Phenomena: Technological Applications of Colour Chemistry*. 2002: Royal Society of Chemistry.

176. Li, D., Z. Peng, L. Deng, Y. Shen and Y. Zhou, *Theoretical studies on molecular structure and vibrational spectra of copper phthalocyanine.* Vibrational Spectroscopy, 2005. **39**(2): p. 191-199.

177. Redington, R.L. and K.C. Lin, *Infrared spectra of trifluoroacetic acid and trifluoroacetic anhydride.* Spectrochimica Acta Part A: Molecular Spectroscopy, 1971. **27**(12): p. 2445-2460.

178. Kagarise, R.E., *Infrared Spectrum of Trifluoroacetic Acid Vapor.* The Journal of Chemical Physics, 1957. **27**(2): p. 519-522.

179. Efimov, A.M. and V.G. Pogareva, *Water-related IR absorption spectra for some phosphate and silicate glasses.* Journal of Non-Crystalline Solids, 2000. **275**(3): p. 189-198.

180. Fischer, J. and A. Weiss, *Transport Properties of Liquids. V. Self Diffusion, Viscosity, and Mass Density of Ellipsoidal Shaped Molecules in the Pure Liquid Phase.* Berichte der Bunsengesellschaft für physikalische Chemie, 1986. **90**(10): p. 896-905.

181. Frurip, D.J., L.A. Curtiss and M. Blander, *Vapor phase association in acetic and trifluoroacetic acids. Thermal conductivity measurements and molecular orbital calculations.* Journal of the American Chemical Society, 1980. **102**(8): p. 2610-2616.

182. Djurišić, A.B., C.Y. Kwong, T.W. Lau, W.L. Guo, E.H. Li, Z.T. Liu, H.S. Kwok, L.S.M. Lam and W.K. Chan, *Optical properties of copper phthalocyanine.* Optics Communications, 2002. **205**(1-3): p. 155-162.

183. Gu, D. and Q. Chen, *Copper phthalocyanine film studied with spectroscopic ellipsometry.* Optics Communications, 1994. **110**(5-6): p. 576-580.

184. Einstein, A. and R. Fürth, *Investigations on the theory of Brownian movement*. 1956, New York, N.Y.: Dover Publications.

185. Bartels, L., *Tailoring molecular layers at metal surfaces.* Nat Chem, 2010. **2**(2): p. 87-95.

186. Walsh, M.R., C.A. Koh, E.D. Sloan, A.K. Sum and D.T. Wu, *Microsecond Simulations of Spontaneous Methane Hydrate Nucleation and Growth.* Science, 2009. **326**(5956): p. 1095-1098.

187. Ghani, F., I. Bochukov, K. Fostiropoulos and H. Riegler, *Hybrid solution/vacuum-processed bilayer heterojunction organic solar cells: Structural characterization and performance.* Thin Solid Films, 2012. **525**(0): p. 177-181.

188. Schechtman, B.H. and W.E. Spicer, *Near infrared to vacuum ultraviolet absorption spectra and the optical constants of phthalocyanine and porphyrin films.* Journal of Molecular Spectroscopy, 1970. **33**(1): p. 28-48.

189. Forrest, S.R., *T he Limits to Organic Photovoltaic Cell Efficiency.* MRS Bulletin, 2005. **30**: p. 28-32.

190. Yu, G. and A.J. Heeger, *Charge separation and photovoltaic conversion in polymer composites with internal donor/acceptor heterojunction.* Journal of Applied Physics, 1995. **78**(7): p. 4510-4515.

191. Sariciftci, N.S., L. Smilowitz, A.J. Heeger and F. Wudl, *Photoinduced Electron Transfer from a Conducting Polymer to Buckminsterfullerene.* Science, 1992. **258**(5087): p. 1474-1476.

192. Veenstra, S.C., G.G. Malliaras, H.J. Brouwer, F.J. Esselink, V.V. Krasnikov, P.F. van Hutten, J. Wildeman, H.T. Jonkman, G.A. Sawatzky and G. Hadziioannou, *Sexithiophene-C60 blends as model systems for photovoltaic devices.* Synthetic Metals, 1997. **84**(1-3): p. 971-972.

193. Atwater, H.A. and A. Polman, *Plasmonics for improved photovoltaic devices.* Nat Mater, 2010. **9**(3): p. 205-213.

194. Michler, G.H. and W. Lebek, *Ultramikrotomie in der Materialforschung*. 2004: Hanser.

195. Danino, D., A. Bernheim-Groswasser and Y. Talmon, *Digital cryogenic transmission electron microscopy: an advanced tool for direct imaging of complex fluids.* Colloids and Surfaces A: Physicochemical and Engineering Aspects, 2001. **183–185**(0): p. 113-122.

196. Atkins, P. and J. de Paula, *Physical Chemistry*. 2009: W. H. Freeman.

197. Haken, H. and H.C. Wolf, *Molekülphysik und Quantenchemie: Einführung in die experimentellen und theoretischen Grundlagen*. 2006: Springer.

198. Demtröder, W., *Experimentalphysik 3: Atome, Moleküle und Festkörper*. 2010: Springer.

199. Ashcroft, N.W. and N.D. Mermin, *Solid state physics*. 1976: Saunders College.

200. Aliofkhazaeri, M. and N. Ali, *Two-Dimensional Nanostructures*. 2012: CRC PressINC.

201. Solanki, J.N. and Z.V.P. Murthy, *Controlled Size Silver Nanoparticles Synthesis with Water-in-Oil Microemulsion Method: A Topical Review.* Industrial & Engineering Chemistry Research, 2011. **50**(22): p. 12311-12323.

202. Huang, J., F. Kim, A.R. Tao, S. Connor and P. Yang, *Spontaneous formation of nanoparticle stripe patterns through dewetting.* Nat Mater, 2005. **4**(12): p. 896-900.

Acknowledgement

It would not have been possible to write this doctoral thesis without the help and support of the kind people around me, to only some of whom it is possible to give particular mention here.

Foremost, I would like to express my sincere gratitude to Prof. Dr. Helmuth Möhwald for the excellent working conditions and helpful scientific discussions in the Department of Interfaces.

This thesis would not have been possible without the help, support and patience of my principal supervisor, Dr. Hans Riegler. His guidance helped me in all the time of research.

I am thankful to Dr. Torsten Sievers for fruitful discussions, instructions and his patience in reading and correcting the thesis.

I thank Dr. Juliane Kristen for her support in solubility measurements, Dr. Antonio Stocco for support in ellipsometric measurements, Dr. Christoph Böttcher for Cryo-TEM measurements at Free university-Berlin, Stefan Karpitschka, and Dr. John Berg for discussions, Mrs. Anne Heilig for support in AFM lab.

My sincere thanks also go to project partners Dr. Konstantinos Fostiropoulos and his group, especially Dr. Ivelin Bochukov for allowing me to work in their lab at Heterogeneous Material Systems Institute of Helmholtz Zentrum Berlin and supporting me in preparation of organic solar cells.

I am thankful to all group members, colleagues, and technicians in the Max Planck Institute for Colloids and Interfaces for support.

I would like to thank Bundesministerium für Bildung und Forschung (BMBF) for funding (Project 03X3525F, SOHyb – Keimbildungsinduzierte Selbstorganisation zur Strukturierung organischer Hybridsolarzellen).

I express my gratitude to all my friends and family in Berlin, especially my husband, Soheil, for support and encouragement during the work. Last but not the least; I would like to express my deepest gratitude to my parents, Massomeh Ansarian and Mehdi Ghani for their constant spiritual support and care throughout my life.

Appendix 1 – Methods

- Scanning electron microscopy (SEM)
- Transmission electron microscopy (TEM)
- Cryogenic Transmission Electron Microscopy (Cryo-TEM)
- Spectroscopy
- FT-IR Spectroscopy
- X-Ray powder diffraction
- High vacuum vapor deposition

Scanning electron microscopy (SEM)

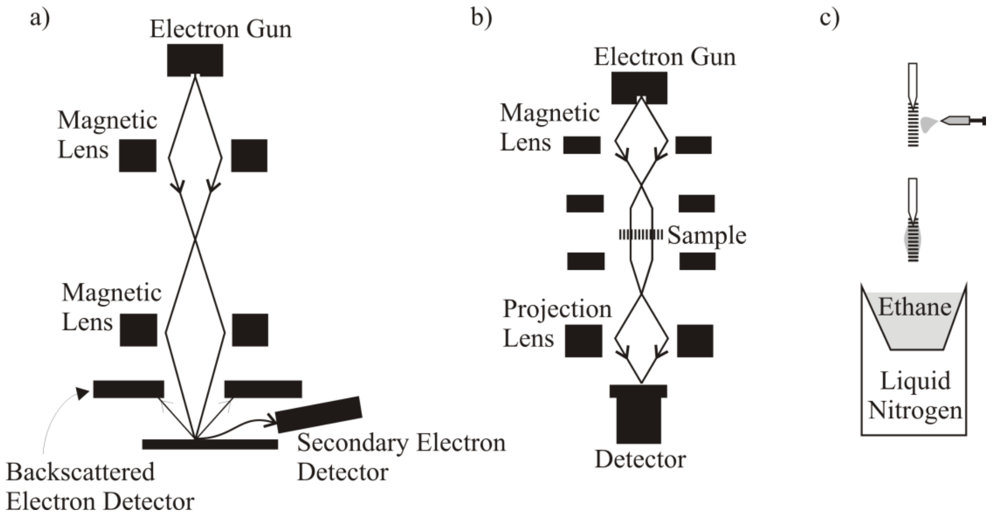

Fig. 1) Schematic draw of a) SEM device, b) TEM, c) sample preparation for cryo-TEM.

In SEM the surface of the sample is scanned with a focused electron beam, called primary electron beam. This beam is focused using electromagnetic lenses. By interaction of the primary beam and atoms near the sample surface, elastic and in elastic scattering, the secondary electron, back scattered electron, characteristic X-rays and etc. are emitted from the surface of the sample, see fig. 1a. Typically the secondary electrons are used to produce images of the sample surface. Due to the narrow electron beam, high resolution images with detailed information of up to 1 nm resolution can be taken using appropriate devices [194].

The samples were measured with a Gemini Leo 1550 instrument at an operation voltage of 3 keV. The measured SEM images have almost a resolution of some 10 nm and are not suitable for measuring the nanostructures

Transmission electron microscopy (TEM)

TEM works similar to light microscopy but uses electron radiation. The wavelength of the electron is 10^5 times smaller than that of visible light, so that smaller features of a few Angstrom size can be detected. In a TEM the electron radiation travels through vacuum in the column of the microscope, see fig. 1b. The radiation is focused by electromagnetic lenses so that a parallel radiation passes through the sample. Depending on the density of the material some of the electron may be scattered. The unscattered electron hits the detector at the bottom of the microscope. It is important that the sample is transparent for the electron radiation [194].

I used gold TEM grids and dropped a solution on them. After evaporation of the solvent, the samples were transported to the TEM device for measurement.

Cryogenic Transmission Electron Microscopy (Cryo-TEM)

Cryo-TEM is a well-established method to detect fine specimens as macromolecules floating in the solution. The sample is frozen immediately and preserved in a special cooling sample holder in liquid nitrogen. The preparation is as follows: a TEM grid is picked up with tweezers and a drop of the sample is placed on it. The grid is transferred to a cell cooled immediately with ethanol and then with liquid nitrogen, see fig. 1c. The frozen sample is transferred undercooled to the microscope [195].

Spectroscopy

In spectroscopy, the interaction between light and matter is studied. The light, as an electromagnetic field, interacts with the molecule as a quantum system. In quantum mechanics the molecule is described as a system of N electrons and Z nuclei with the Hamiltonian [196, 197]:

$$H_{mol} = T_{el} + V_{el-nuc} + V_{el-el} + T_{nuc} + V_{nuc-nuc} \tag{2-19}$$

where T_{el} and T_{nuc} are the kinetic energy of electrons and nuclei, $V_{el\text{-}nuc}$, $V_{el\text{-}el}$ and $V_{nuc\text{-}nuc}$ are the potential energy of the interaction of nuclei and electrons, the interaction of electrons among themselves and of nuclei, respectively. Different quantum mechanical approximations offer the possibility to estimate the solution of such complicated systems. According to the Born-Oppenheimer approximation, the nuclei are presumed fixed, while the electrons move. The resulting Hamiltonian yields the potential energy surface of the molecule as a function of nuclei separation.

As illustrated in fig. 2, the energy values of a molecule are expressed with quantum numbers, which fall usually into three groups: (1) n, which is associated with the electronic motion and can be obtained from the Born-Oppenheimer approximation (2) v, the quantum number, which defines vibrational states of the nuclei (c) quantum number J, which depends on the rotation of the nuclei. The vibration of the molecule is described as a function of nuclei displacement from their equilibrium position.

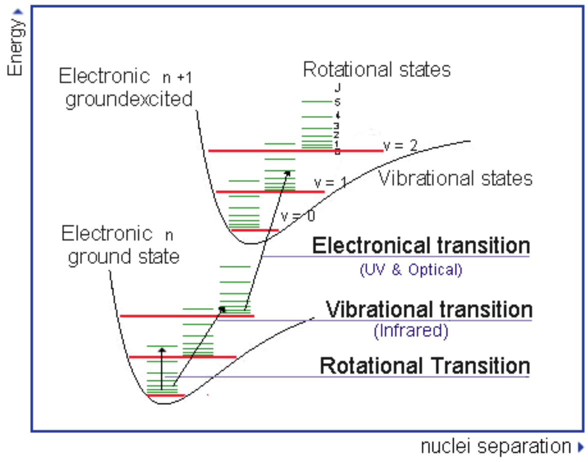

Fig. 2) Schematic drawing of energy states of a molecule

Molecules or atoms can absorb or emit radiation if the energy state of the matter and the frequency of the radiation match, the molecules or atoms can transit from an initial state (Ψ_i) to a final state (Ψ_f). Quantum mechanically the transition dipole moment is expressed as (μ: dipole moment operator):

$$\mu_{fi} = \int \Psi_f^* \, \mu \, \Psi_i \tag{2-20}$$

If the transition moment is not zero ($\mu_{fi} \neq 0$), the transition appears in the infrared or ultra violet spectrum.

UV-Vis Spectroscopy

The wavelength of ultra violet and visible light ranges from 200 to 900 nm. This radiation energy can cause a change of electronic state of the molecules or atoms. The electrons in a molecule are usually in three possible types of ground state: single bond (σ), multiple bond (π) and non-bonding (n). By absorbing the radiated energy the electrons transit from HOMO to LUMO. σ-electrons have the lowest energy level and require a lot of energy to be excited. π-electrons are in higher energy levels and can be excited with relatively lower energies. n-electrons are electrons belonging to a lone pair and are of higher energy levels. Both n- and π-electrons can be excited in the UV-Vis range. Transitions of σ-electrons appear seldom in this range [198].

FT-IR Spectroscopy

The heart of the spectrometer is the interferometer, generally a Michelson interferometer. It includes mainly a beam splitter, BS. The beam splitter allows half of the polychromatic radiation to be transmitted toward a moving mirror MM. The other half of the radiation will be reflected toward the fixed mirror perpendicular to the first, see fig. 3. Mirror MM moves back and forward on an axis parallel to its normal with an amplitude x. The reflected radiation from MM reaches the beam splitter after the distance 2(L + x). The one from the fixed mirror reaches the beam splitter after 2L. As a result the two interfere constructively if x is an even multiple of wavelength λ, and destructively if it’s an odd multiple of l/2. Thus the intensity I(x) in the interferogram of the radiation leaving the interferometer would be:

$$I(x) = S(\nu)\cos(2\pi\nu x), \qquad \nu = 1/\lambda$$

S(n) the intensity of the radiation at wave number ν.

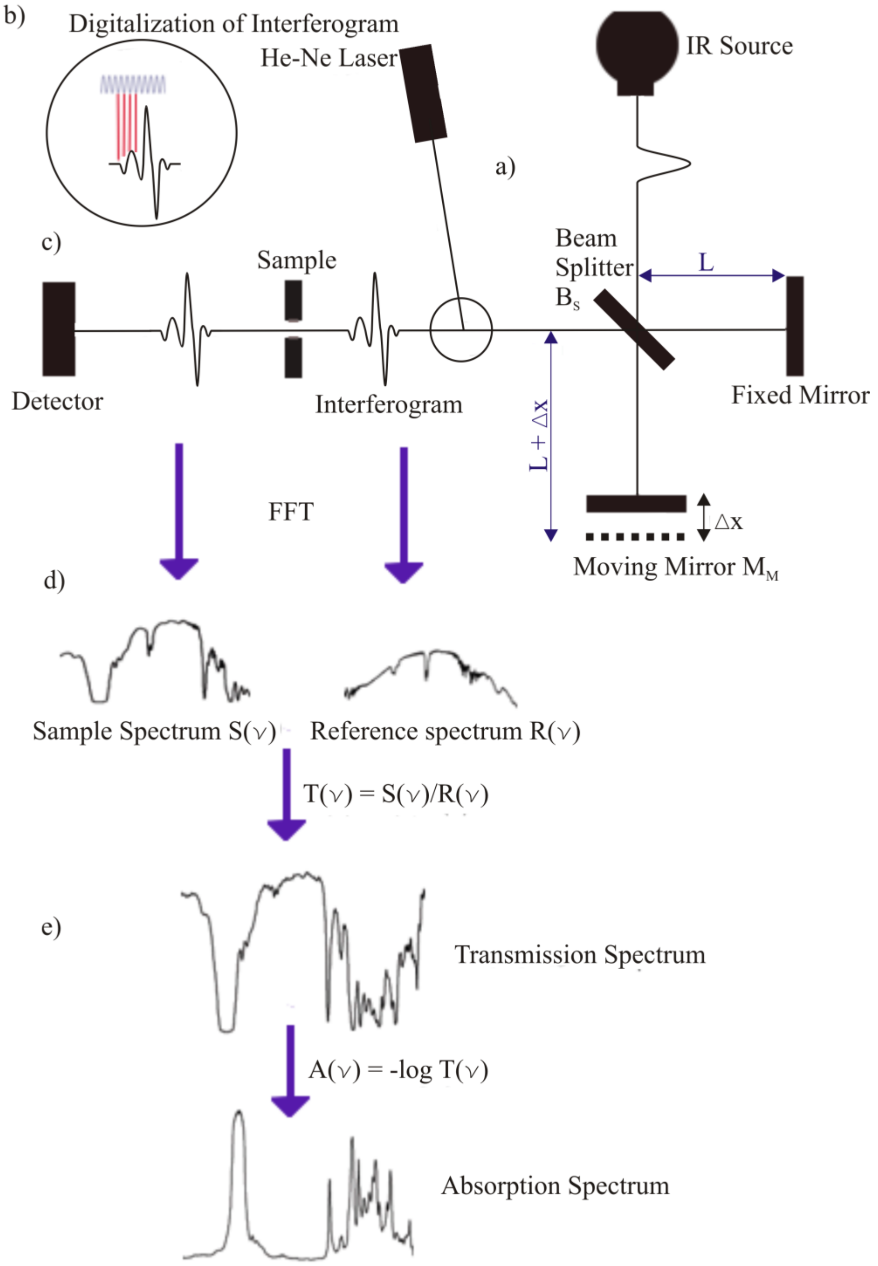

Fig. 3 a) Interferometer, b) using a He-Ne laser to digitize the interferogram, c) the probe beam passes through the sample, d) calculating the Fourier transformation of sample and reference interferogram by computer, e) finding the absorption spectrum

The probe beam passes through the sample exciting the molecular vibrational and rotational transitions which are active in the infrared range. At corresponding wave numbers the intensity will be reduced because of absorption and the interference with the reference beam is changed. The computer takes this interferogram from the detector and calculates the spectrum with some special Fourier transformation algorithms. The transmission spectrum is deduced from these two spectra:

$$\mathrm{T(v)} = \frac{\mathrm{S(v)}}{\mathrm{R(v)}}$$

S(n) is the intensity of the radiation at wave number n. To improve the precision of the spectroscopy the monochromatic beam of a He-Ne laser will be used to digitize the interferogram.

X-Ray powder diffraction

Bragg considers crystals made of parallel planes of atoms, spaced a distance d apart. The condition for a sharp X-ray peak is 1) X-ray should be specular reflected by species in one plane, 2) The reflected ray should interfere constructively. The geometrical relation between wavelength (λ), the spacing between parallel plane (d) and the angle between the incident ray and the plane (θ) is [199], see Figure 2-10a:

$$n\lambda = 2d\sin\theta, \qquad n = 1, 2, \ldots \tag{2-23}$$

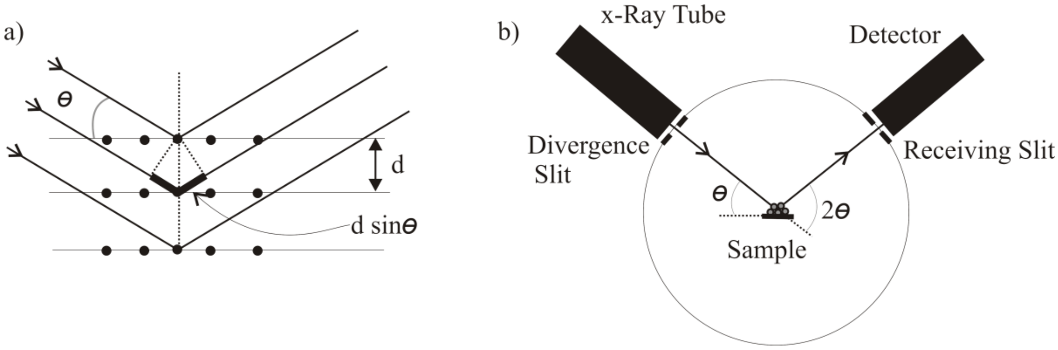

Fig. 4 a) Schematic drawing of a) Bragg diffraction b) x-ray diffractometer

In Von Laue formulation, the crystal is assumed to be composed of identical macroscopic objects (set of ions or atoms) placed at the site R of a lattice, each of which can radiate the incident radiation in all direction. Sharp peaks will be observed just in the direction and at a wavelength for which the rays scattered from all lattice points interfere constructively. Incident X-rays are considered to be from very far away, along a direction $\boldsymbol{n}$ with a wavelength λ, a wave vector $\boldsymbol{k}=2\pi\boldsymbol{n}/\lambda$. The scattered ray will be observed in $\boldsymbol{n}'$ direction with the same wavelength and wave vector $\boldsymbol{k}'=2\pi\boldsymbol{n}'/\lambda$, provided that the path difference between the reflected waves is an integer number of wavelength [199], see Fig. 5:

$$\boldsymbol{k}.\boldsymbol{K} = \frac{1}{2}K. \tag{2-24}$$

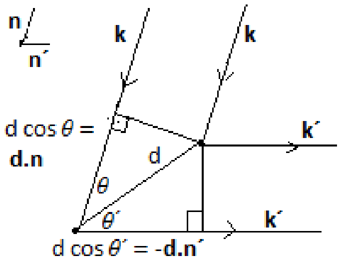

Fig. 5) Laue condition of diffraction

An incident wave vector $\boldsymbol{k}$ will satisfy the Laue condition if and only if the tip of the vector lies in a plane that is perpendicular bisector of a line joining the origin of k-space to a reciprocal lattice point **K**. Such k-space planes are called Bragg planes.

The Bragg condition requires that θ and λ match (or the Laue that the tip of **k** lies on a k-space Bragg plane of the crystal lattice). X-ray with the wavelength λ striking a 3 dimensional crystal at an arbitrary incidence angle will generally not satisfy the Bragg (or Laue) condition and will not be reflected. Hence experimentally a continuous range of λ or θ should be studied, usually θ. The simple geometric construction of Ewald allows to visualize these methods. Ewald draws a sphere in k-space centered on the tip of incident wave vector k of radius k. There will be some wave vector k´ satisfying the Laue condition if and only if some reciprocal lattice point in addition to the origin lies on the surface of the sphere. In that case there will be a Bragg reflection from a family of direct lattice planes perpendicular to the RL vector.

There are different methods to search for the crystal structure. In the powder diffraction method (Debye-Scherrer) the diffraction pattern is a combination of diffraction patterns of all orientations because powder grains are randomly oriented. The diffraction patterns are determined by fixing the incident $\boldsymbol{k}$ vector and with it the Ewald sphere and letting the reciprocal lattice rotate around all possible angles about the origin, so that the reciprocal lattice vector **K** generates a sphere of radius **K** about the origin. The sphere intersects the Ewald sphere in a circle if K is less than 2k. Thus each reciprocal lattice vector K, K<2k, generates a cone of scattered radiation with angle φ to the forward direction. An X-ray power diffractometer consists of an X-ray source, a sample stage and a detector, see fig. 4b. The angle, θ, has to be varied during the measurement.

High vacuum vapor deposition

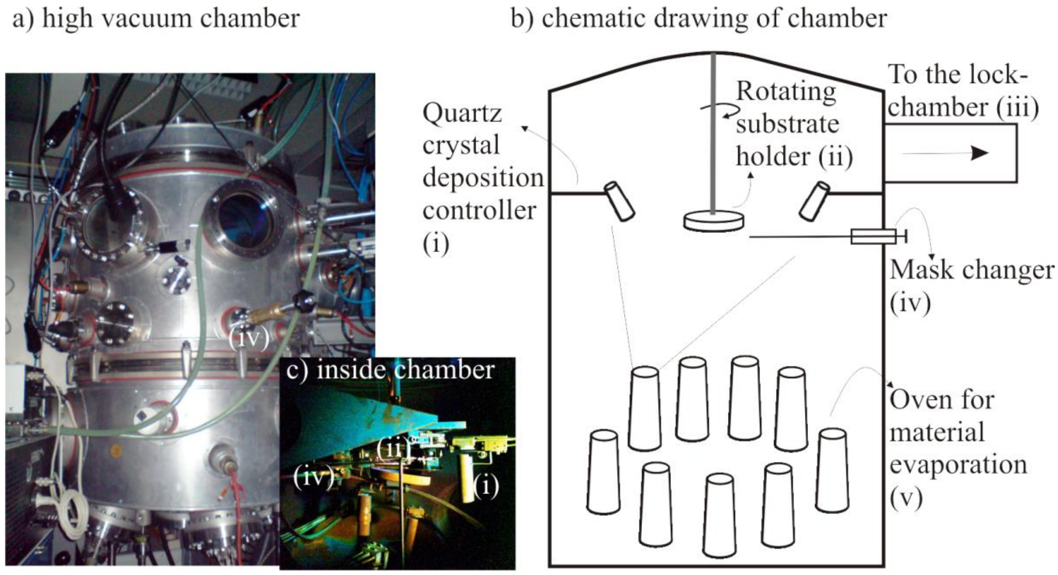

Fig. 6 a) Photograph of high vacuum chamber, b) schematic drawing of the chamber, c) photograph of sample holder, mask changer and quartz crystal deposition controller inside the chamber

For vapor deposition of organic material and metal deposition a high vacuum deposition chamber was used, see fig. 6. The evaporation chamber of organic material was supplied with a pre-pump and turbo pump. The organic ovens were positioned on the bottom of the chamber with their opening facing upward. Each oven was closed with a shutter. A heater and a water cooling system surrounded the ovens to control the temperature. For evaporation the shutter over the oven has to be opened and the temperature has to be set up.

Samples were mounted on the sample holder and transported to the organic evaporation chamber through a lock-chamber. The sample holder was rotating during the evaporation to provide a homogeneous growth of the deposited layer. The thickness of the deposited layer was monitored using a quartz-crystal deposition controller near the sample holder; see fig. 3b and 3c. The deposition rate depends on the oven temperature.

Appendix 2 – Supporting measurements

- Film thickness measurement with X-ray reflectivity
- Film thickness measurement with ellipsometry
- Evaporation rate results by reflectometry

Film thickness measurement with X-ray reflectivity

The X-ray beam is scattered at small angles (< 10°) from a thin layer (CuPc) with a refractive index different from the substrate (SiO_2). As a result of constructive and destructive interference of the reflected beam from the two interfaces (CuPc and SiO_2) and the reflected beam becomes an oscillating function with periods called Kiessig fringes. The thickness of a thin layer can be directly determined from Kiessig fringe analysis, see fig. 1:

$$n\lambda = 2dsin\theta$$

$$4\,\pi\,(n_2 - n_1) = 2d\,(q_2 - q_1)$$

$$d = \frac{2\pi}{\Delta q}$$

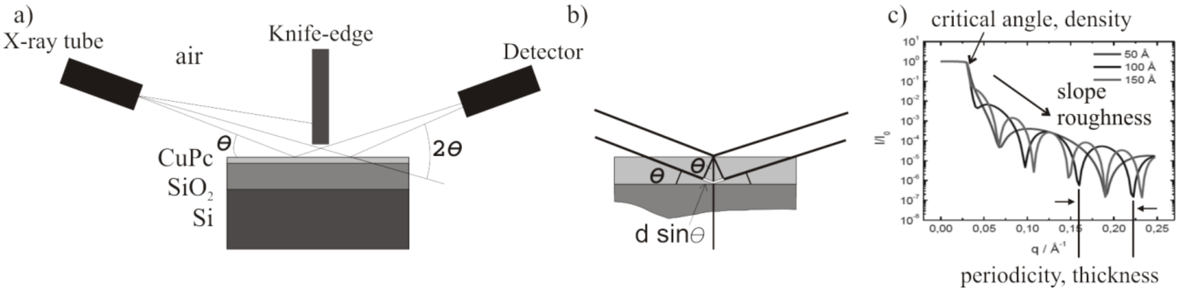

Fig. 1 a) Set-up of reflectivity measurements, b) Reflection at surface, c) a typical X-ray reflectivity intensity for three different sample thicknesses from

Fig.2 shows the result for a multilayer of CuPc deposited by spin casting (200 rps) CuPc/TFA for two concentrations: 1.2×10^{-3}mol·L^{-1} and 3.4×10^{-4}mol·L^{-1}. Even for these two concentrations the Kiessig fringes are not clearly distinguishable, so that the error of the measurements is large: $1.2 \times 10^{-3}\,\mathrm{mol \cdot L^{-1}}$, $d \approx 6 \pm 1\ nm$ and $3.4 \times 10^{-3}\,\mathrm{mol \cdot L^{-1}}$, $d \approx (3 \pm 1)\ nm$. At lower concentration (submonolayer) the results were not reliable.

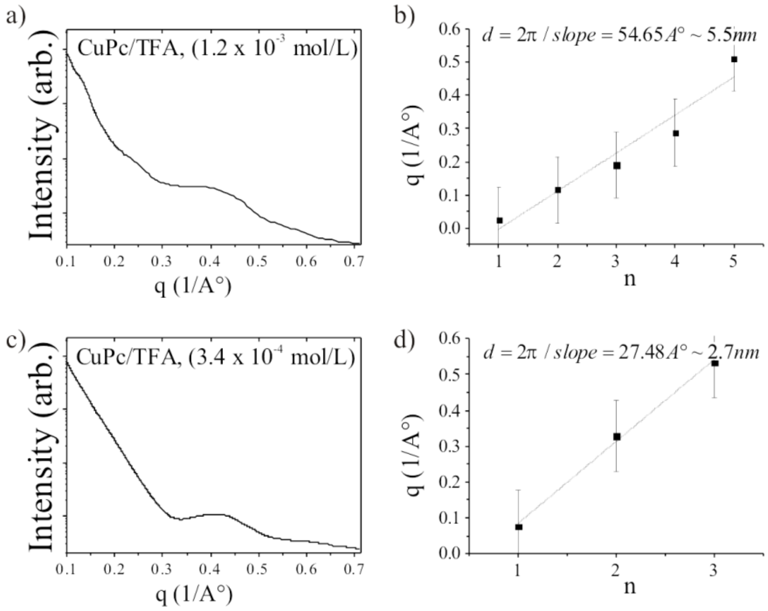

Fig. 2) X-ray reflectivity measurement for multilayers of CuPc deposited by spin casting (200 rps) solutions of a and b) $1.2 \times 10^{-3}\,\mathrm{mol \cdot L^{-1}}$, c and d) $3.4 \times 10^{-3}\,\mathrm{mol \cdot L^{-1}}$

Film thickness measurement with ellipsometry

In ellipsometry linearly polarized light is produced by polarizer/compensator and hits the sample surface. The two components of the electric field, parallel (E_p) and perpendicular (E_s) to the plane of incidence are out of phase after reflection. Both phase and amplitude of the light change after reflection depending on the optical property of the surface, see fig. 5.

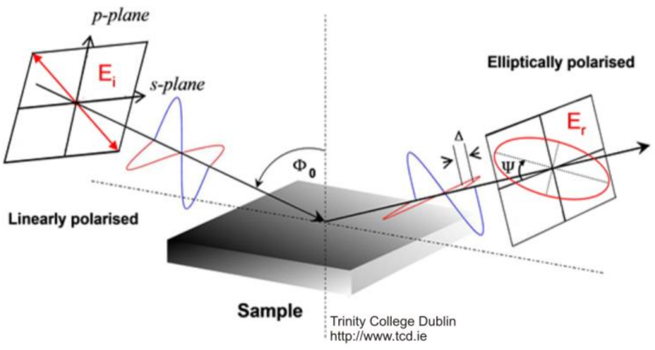

Fig. 3) Schematic diagram of a polarizer – compensator - analyzer ellipsometer

The incident and reflected electric field of light have an angular frequency (ω), a wavenumber (q) and a phase term (δ):

$$E = E_0 \cos(qz - \omega t + \delta)$$

In an ellipsometric measurement the phase difference (Δ) between the two reflected electric fields, parallel (E_p) and perpendicular (E_s):

$$\Delta = \delta_{rp} - \delta_{rs}$$

And also the change in the ratio of the amplitudes is measured:

$$\tan \Psi = \left| \frac{r_p}{r_s} \right|$$

$$\tan \Psi \, . \, e^{i\Delta} = \frac{r_p}{r_s}$$

where r is the Fresnel coefficient of the p and s polarized light. The film thickness can be calculated from the measured value of Δ and ψ. The film thickness was calculated using the Fit-software. Ellipsometry measurements and evaluation have been performed with the kind support of Dr. Antonio Stocco, see fig. 6. Due to the several uncertainties in the measurement, especially at low concentration the film is not complete (submonolayer) and the roughness and a complex refractive index are necessary to obtain reliable results.

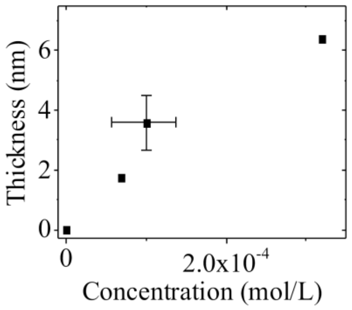

Fig. 4) Ellipsometry result of CuPc thickness deposited by spin casting from different concentrations

The measured thickness for a concentration range is not linear, see fig. 4, which is not acceptable concerning the spin casting physics discussed in chapter 2 and 6. However, at higher concentration (near saturation concentration), presumably a certain fraction of the CuPc, that was deposited already in the preceding deposition step, is again re-dissolved and spun-off.

Evaporation rate results by reflectometry

The evaporation rate was determined by measuring the change of the TFA liquid-film in the spin casting process. The spin coater was placed in an ellipsometer set-up, see fig.1a. The changes in the film thickness produce an interferometry pattern see fig. 1b.

The changes in thickness (*Δd*) were determined from the maximum point of the oscillation amplitude in the reflection pattern, see fig. 1a and b:

$$\Delta d = \frac{\lambda}{2(\sqrt{n^2 - sin^2\theta})}$$

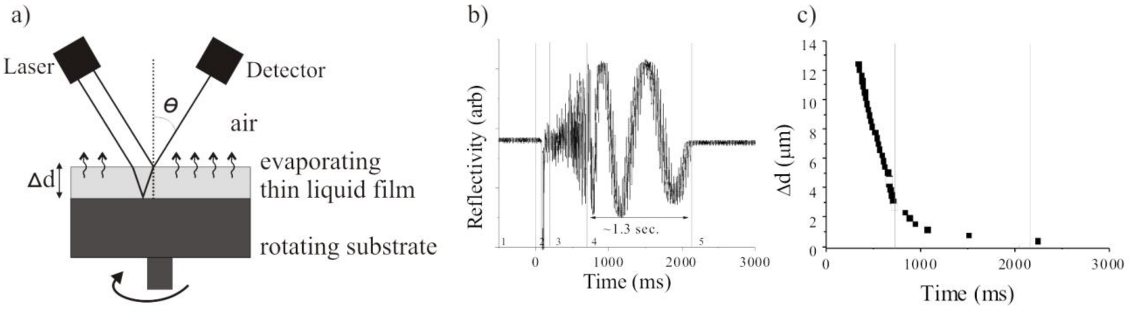

Fig. 5 a) Schematic set-up of film-thickness measurement during spin casting, b) reflectivity versus time, c) changes of film thickness versus time.

Unfortunately the measurement for TFA is not very accurate. At the beginning of the spin casting the liquid film becomes thinner by spin-off and evaporation. At this stage the fluctuations in oscillation are very high. Later as equilibrium film thickness is reached, the film thickness changes due to the evaporation. However after one or three oscillations TFA is evaporated. This makes it difficult to measure a reliable value for the changes in film thickness. From about 10 measurements, the evaporation rate is estimated to be 0.5 μm·s^{-1}.

Appendix 3 – XRPD results

X-ray diffraction measurement

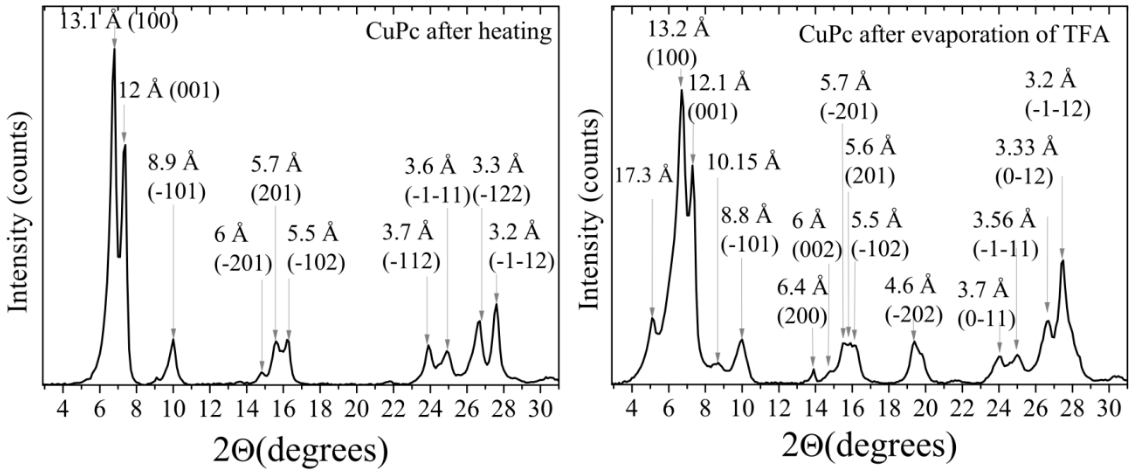

Fig. 1) X-ray powder diffraction pattern of α-CuPc (right) and CuPc deposited from TFA (left).

Table 0-1) Experimental data available on α-CuPc [131]

Chemical formula	$C_{32}H_{16}CuN_8$	Density (mg·m^{-3})	1.64
Volume of unit cell (Å^3)	582.3	a, b, c (nm)	~ 1.3, ~ 0.38, ~ 1.2

Table 1) Diffraction peaks and d-spacing and estimates using crystal structure visualization software “Diamond” version 3.1f compared to simulated pattern and unit cell of α-CuPc from Hoschino et al. [131]

CuPc after TFA evaporation			after TFA evaporation and heating			α-CuPc[131]		
2Θ° ± 0.1°	d-spacing Å	Intensity	2Θ°± 0.1°	d-spacing Å		d-spacing Å	Intensity	h k l
5.1	17.3*	4504						
6.7	13.2	20339	6.8	13.1	24147	12.8849	3029933	100
7.3	12.1	15094	7.4	12	17234	11.9892	1919467	001
8.7	10.2+	1397						
10	8.8	3018	10	8.87	3261	8.8280	291459	-101
13.9	6.4	951	‡	‡		6.4425	5032	200
14.8	5.98	814	14.8	5.98	898	5.9946	56027	002
15.5	5.7	2754	15.6	5.67	3124	5.6480	328398	201
15.9	5.57†	2771						
16.2	5.46	2612	16.2	5.47	3229	5.459	372942	-102

19.4	4.5	2870	‡	‡		4.4140	1725	-202
24	3.7	1833	23.9	3.72	2844	3.6919	53232	0-11
25	3.6	1950	24.9	3.57	2425	3.6043	52133	-1-11
26.7	3.33	4306	26.7	3.34	4579	3.3443	653464	0-12
27.5	3.24	8499	27.6	3.23	5806	3.2373	717386	-1-12

*, +, †: new peaks (~ 2 × 8.8), (~ 2× 5.4)

‡ the intensity of the peaks were too low in comparison with α-CuPc[131].

Appendix 4 – The adsorption function results

The amount of adsorbed material ($\Gamma_a(N)$) in each layer (*a*: layer number) versus the total amount of adsorbed material (*N*) can be calculated using a sigmoid function (Γ_{max}, N_0 and γ_a are constants defined for each layer):

$$\Gamma_a(N) = \frac{\Gamma_{max}}{1 + e^{-\gamma_a(N-N_0)}} \tag{7-17}$$

The inflection point of the sigmoidal function (N_0) is where the adsorption rate ($d\Gamma/dN$) is maximum [62].

Table 1) Sigmoid growth function for the amount of adsorbed material in each layer

Layer	Adsorption function	Γ_{max}	γ	N_0
1	$\Gamma_1(N) = \frac{3}{1 + e^{-2(N-1.3)}}$	3 ± 0.1	2 ± 0.1	1.3 ± 0.1
2	$\Gamma_2(N) = \frac{2.7}{1 + e^{-1.3(N-4.4)}}$	2.7 ± 0.1	1.3 ± 0.2	4.4 ± 0.2
3	$\Gamma_3(N) = \frac{2.4}{1 + e^{-(N-7.2)}}$	2.4 ± 0.1	1 ± 0.2	7.2 ± 0.2
4	$\Gamma_4(N) = \frac{2}{1 + e^{-(N-8.8)}}$	2 ± 0.2	1 ± 0.2	8.8 ± 0.3
5	$\Gamma_5(N) = \frac{1}{1 + e^{-(N-9.6)}}$	1 ± 0.3	1 ± 0.4	9.6 ± 0.8
a	$\Gamma_a(N) \approx \frac{3.6 - 0.5\,a}{1 + e^{-(2-0.3a)(N-2a)}}$	(3.6 ± 0.3) – (0.5 ± 0.1) *a*	(2 ± 0.3) – (0.3 ± 0.1) *a*	(2.1 ± 0.7) *a*

Appendix 5 – Supporting AFM measurements

- AFM images of drop casted film
- Influence of the tip on the structures

AFM images of drop casted film:

In a drop casted film the morphology is not homogeneous and different coverages can be found in different parts of the drop area. Fig.1 shows different areas of a drop of CuPc/TFA solution dried under ambient condition.

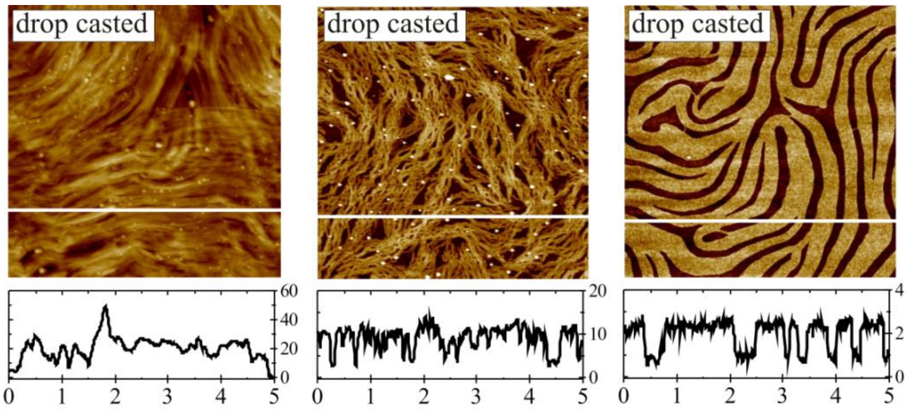

Fig. 1) AFM image of different part of drop casted film

Influence of tip on the structures in high resolution measurements:

As mentioned in chapter 2, the material loosely binding to the substrate can be attracted to the AFM tip. This effect can change the features and also the tip radius. Especially at high resolution measurement, the tip is longer in contact with the sample. In that case the influence of the tip is more prominent. In low resolution measurements, the influence of tip is not significant and the AFM images are up to several scans (at least 5 scan per area) reproducible.

Fig. 2 shows AFM images taken sequentially from a ribbon of ~ 50 nm width. The images are taken by a soft tapping AFM mode. The amplitude image (fig 2 c) shows that the measurement is not noisy. At monolayer coverage, the structures were slightly changed by measuring in light tapping mode with JPK-Nanowizard:

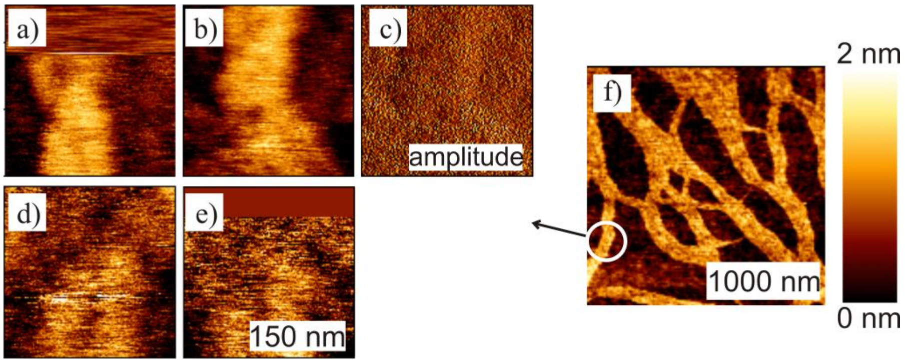

Fig. 2) Sequential Tapping mode AFM scans of a nanoribbon on SiO_2. The images show the influence of a tip on the structure. a) Height image of first scan, b) height image of second scan, c) amplitude image of second scan, d) height image of third scan, e) height image of fourth image, and f) height image of the larger area.

At multilayer coverage, the structures can be changed easier than in monolayer coverages, see fig. 3. This verifies that the binding of the molecule with substrate (monolayer coverage) is stronger than binding of molecules with molecules in the next layer (multilayer coverage).

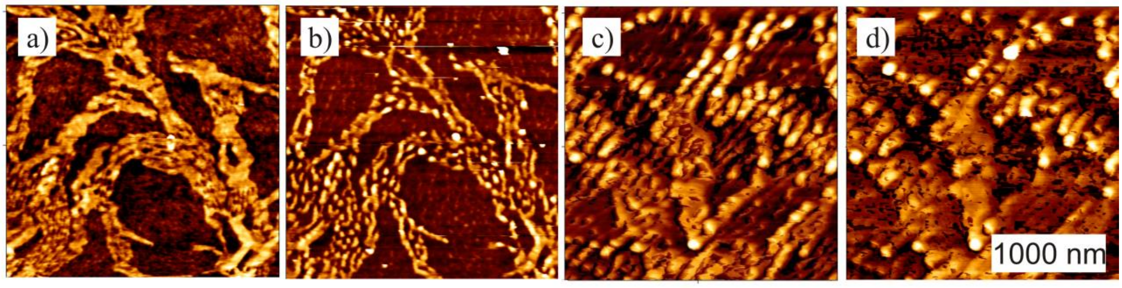

Fig.3) Sequential Tapping mode AFM scans of a multilayer coverage on SiO_2.

Dip coating in a solution mixture

With a mixture of TFA and chloroform (1:1) solvent, two different structures were deposited: the typical CuPc nanoribbons as deposited from TFA (see Figure 5-2a) and larger aggregates (40-50 nm). Measurements showed that the mixing ratio influences the structure of the film.

Appendix 6 – Results on CuPc film from solution mixture

for application in organic solar cells

Solvent mixture is used to produce 3-dimensional structures for OSC application. Using TFA and TCM mixture as solvent, I was able to produce novel structures of CuPc nanoribbons (< 10nm) with larger aggregates on top (some 10s of nm), see fig. 1.

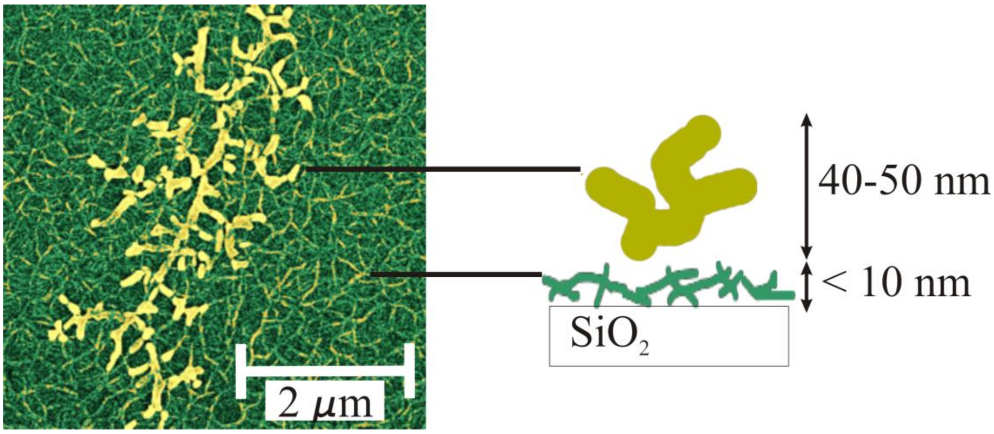

Fig. 1) SEM image of CuPc deposited from TFA and chloroform (TCM) mixture

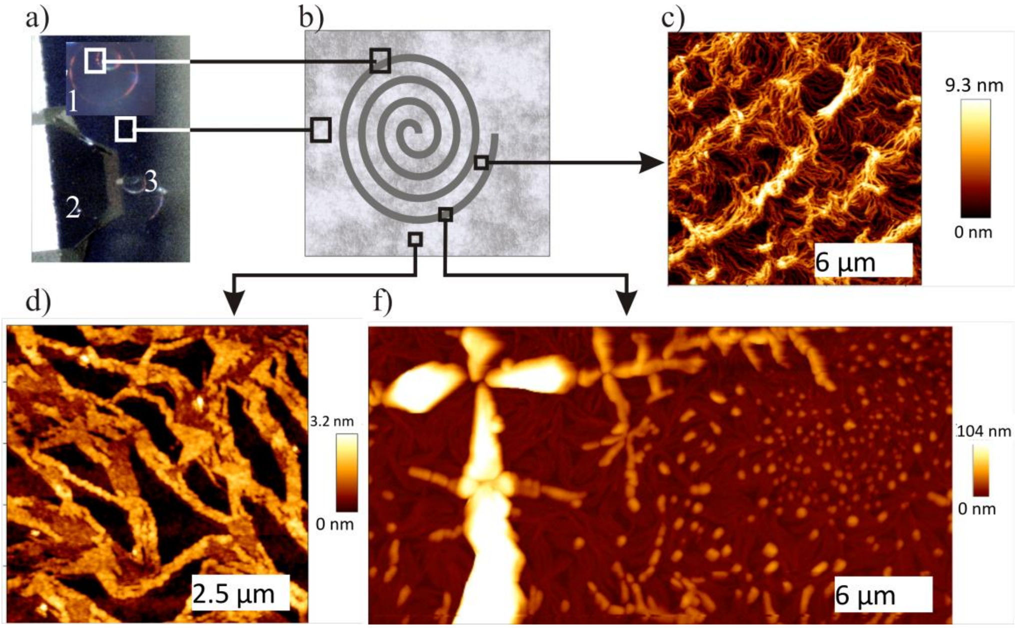

Fig. 2 a) optical image of drying pattern produced by spin casting CuPc/TFA/TCM (1,3) and AFM cantilever (2) b) schematic drawing of the drying pattern c, d, and f) AFM image of the film

Further AFM measurements show that by spin casting the CuPc/TFA/TCM solution in ambient atmosphere, a film of nanoribbons is produced. On this film drying patterns (Marangoni instability) are formed, see fig. 2a and 2b. The AFM image of the film is presented in fig. 2b, and of larger aggregates/ drying patterns in fig. 2c and 2.d.

The AFM images indicate a phase separation during film formation, where two kinds of solid aggregate nucleate and grow from solution. Furthermore the influence of water was studied on CuPc/TCM/TFA solution. To this end a drop of water (0.2 ml) is added to a CuPc/TCM/TFA solution (1:1). The CuPc/TCM/TFA is homogeneous and has a light reddish blue color, see fig. 3a. By adding water, the color of the solution changes to green and an elliptical liquid volume (pink-blue) precipitates on the bottom of the container, see fig. 3b and 3c. The green part of the solution is CuPc/TFA (see chapter 6 aggregation of CuPc in TFA/water mixture), and the elliptical volume is CuPc/TCM/(with presumably small amount of TFA).

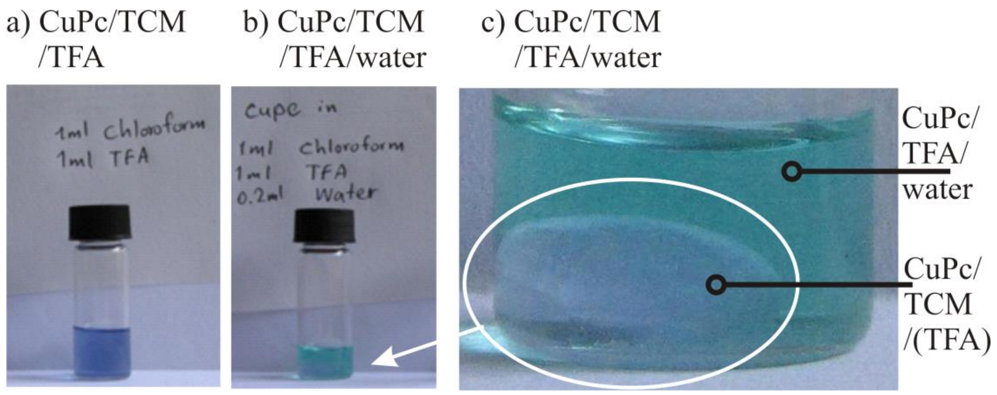
a) CuPc/TCM /TFA

b) CuPc/TCM /TFA/water

c) CuPc/TCM /TFA/water

Fig. 3) Solution of a) CuPc/TFA/TCM, b) solution (a) + 0.2 ml water, and c) larger picture of solution (b)

Furthermore the contact angle of the solvent mixture of TFA/TCM on planar SiO_2 surfaces for different volume content is measured (vol. %), see fig. 4a and 4b. The contact angle of TFA on SiO_2 substrate is ~ 0°and of TCM ~ 10°. The contact angle of the mixture is changing from 0° to 40°. This indicates that not just the water content of the atmosphere, but also the mixing ratio of TFA and TCM play a major role on dewetting during aggregation of CuPc in the solution mixture.

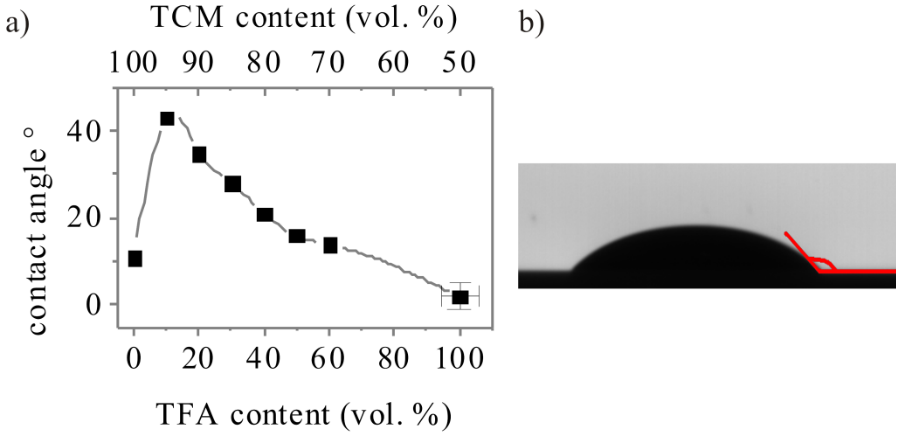

Fig. 4) contact angle measurement of TFA/TCM mixture on SiO_2 substrate

Supposedly, the large aggregates (some 10s of nm) are formed due to a dewetting of the solution due to the water existence. The nucleation and growth of the structure is caused by instabilities during the drying process and therefore is very sensitive to experimental conditions, especially water content. Due to the hydrophobicity of chloroform and the sensitivity of the chloroform to the environment condition, the experiments are not exactly reproducible in ambient condition. For understanding the system and producing aggregates of favorable sizes, the instabilities have to be controlled in laboratory conditions. Therefore further equipment was necessary to continue the experiment.

Appendix 7 – Results on CuPc/ Hexacosane as template

for application in organic solar cells

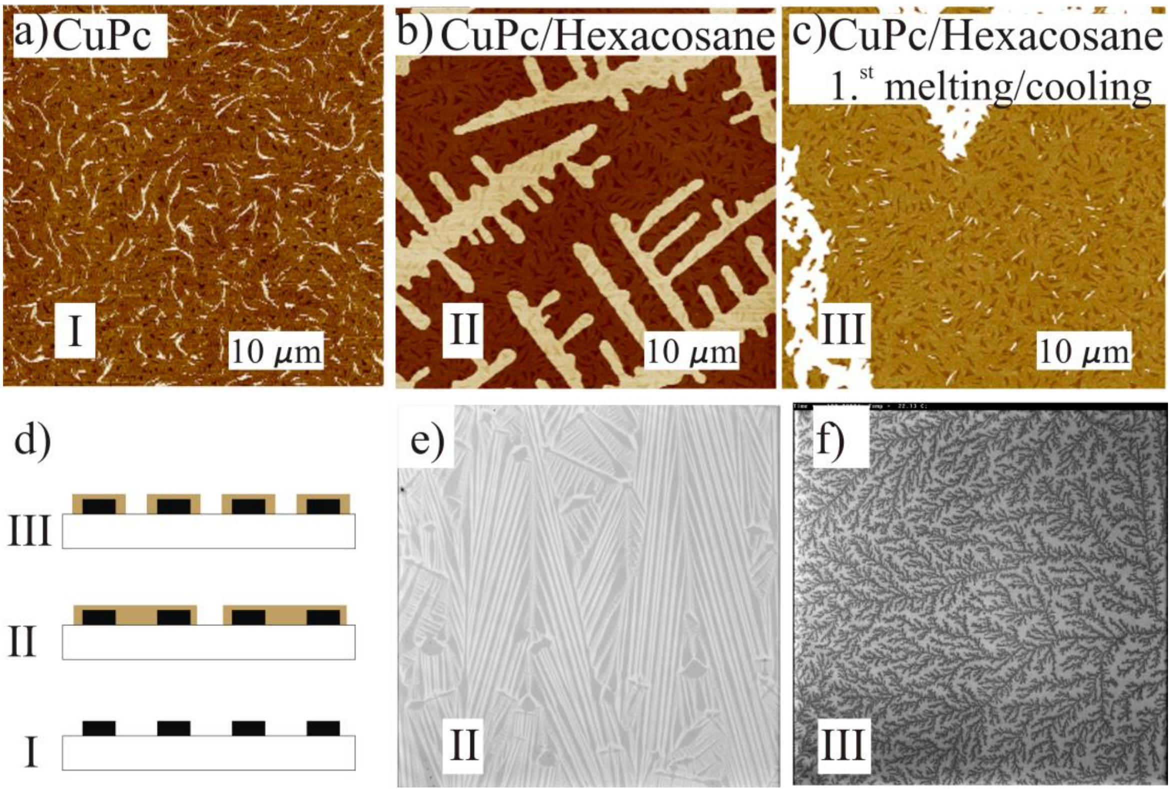

Fig. 1) AFM image of a) CuPc nanoribbons prepared by dip coating , b) sample a dip coated into hexacosane/toluene solution, c) sample b heated and cooled down. d) Schematic drawing of the experiment; optical image of e) sample b, and f) sample c

CuPc/hexacosane is used to produce a template for OSC. The idea is to cover part of the surface with a blocking layer (nonconductive) and then evaporate the organic layer to produce a dendrite structure, which may help for effective exciton diffusion and charge transport in OSC. The dendrite structure needs to be in the nm-range (exciton diffusion length). Unfortunately the structures are much larger (µm range), see fig. 1.

CuPc nanoribbons dipped into toluene solvent: Submonolayer and multilayer of CuPc nanoribbons can be washed out by immersion into toluene for ~ 3 min. With 10 dippings and drawing into toluene solvent (1 mm/s), the coverage becomes lower, however CuPc nanoribbons can still be seen with AFM.

CuPc nanoribbons dipped into hexacosane/toluene solution: Multilayer (two layer) coverages of CuPc nanoribbons were produced by dipping SiO_2 wafers into CuPc/TFA (1×10^{-3} $mol \cdot L^{1}$, 1mm/s) solutions, fig 1a. Then the sample was dipped into hexacosane/toluene solution, fig 1b. The dry film is first heated to 60°C and then cooled down (20°C per min), fig 1c. The melting temperature of alkane is far below the CuPc phase transition temperature.

Although a multilayer coverage of CuPc was used, fig. 1a, after dipping the observed CuPc coverage was a submonolayer, fig. 1b and 1e. By heating the alkane melts and by cooling down it aggregates into solid, fig. 1d. The front of solid aggregates of alkane follows the CuPc nanoribbons shape, fig. 1c and 1f.

Appendix 8 – Results on the effect of the CuPc nanoribbons

as template in organic solar cells

CuPc and ZnPc are used as donor layer in OSC. I studied the influence of CuPc nanoribbons (prepared by spin casting in ambient condition) as a morphological template for ZnPc deposition in high vacuum.

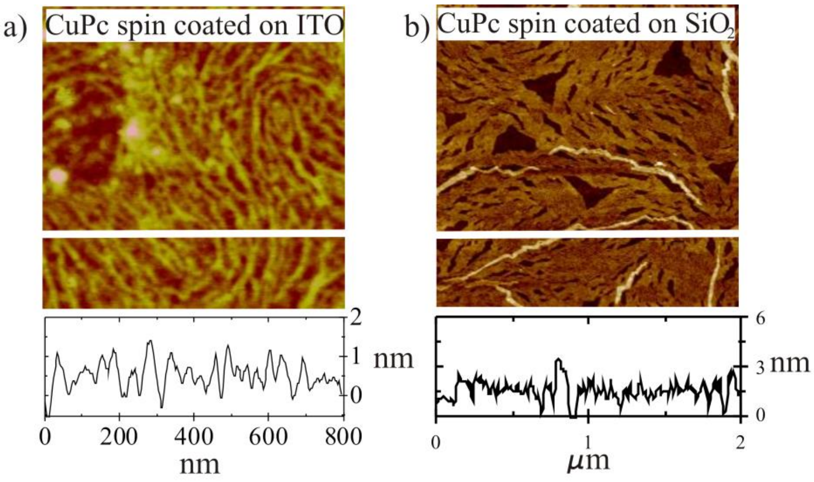

Fig. 1) CuPc spin coated from solution on a) SiO2 CuPc, b) on ITO, (3.2 × 10-4 mol/L and 50 rps)

In comparison with ITO, SiO_2 substrates have a low roughness <1nm and have no special morphological features in AFM, therefore features of the deposited layer can be studied with less ambiguity on that surface. I used SiO_2 parallel to ITO for the morphological study, fig. 1.

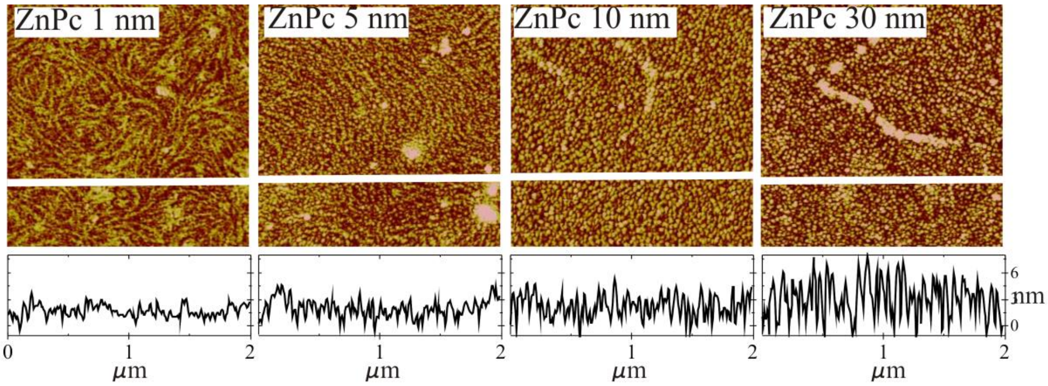

Fig. 2) ZnPc evaporated on CuPc/SiO_2 (fig. 1a) for 1, 5, 10, 30nm.

CuPc/TFA was spin coated onto the SiO2 substrate to prepare a template with nanoribbons, fig 1. a. ZnPc was evaporated in high vacuum onto the template with a ZnPc film-thickness of 1nm, 5nm, 10nm, 30nm. By a ZnPc film of 10nm the pre-structure of the template is partially filled, by 30nm the pre-structures are completely filled, fig. 2. Presumably the template influences mainly the interface between the ITO contact and ZnPc as electron donor-layer in OSC.

Performance OSC

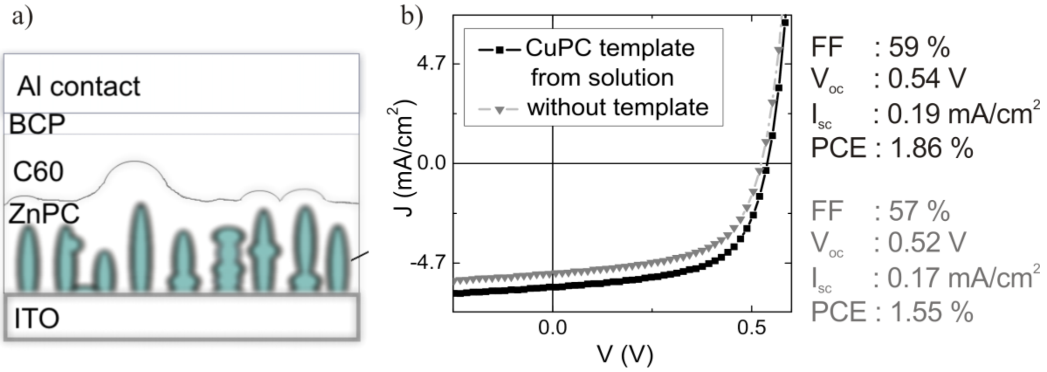

Fig. 3 a) schematic drawing of OSC, b) Comparison of I-V characteristics of with and without a thin solution based template layer of CuPc

The wet deposition was performed via spin-coating, followed by drying, both under ambient conditions (RT). A rather thin wet-deposited CuPc layer served as template for a conventional vacuum evaporation deposited ZnPc layer. 25 nm zinc phthalocyanine (0.07 nm/sec) as electron donor, 30nm fullerene (0.07nm) as electron acceptor and bathocuproine (BCP, 0.01nm) as hole-blocking layer and aluminum (AL, 0.1nm/sec) as electric contact were evaporated sequentially by thermal evaporation in ultrahigh vacuum (~10^{-7} mbar) with the substrate at room temperature. The highest PCE of an optimized typical ZnPc/C60/BCP/AL OSC prepared at the same conditions without any template can reach up to 1.5%. Using the template increases the efficiency up to 1.83%.

Appendix 9 – Results processing silver nanoparticles

from TFA solution for application in organic solar cells

Silver nanoparticles are usually synthetized by physical vapor deposition or through complicated methods like ion implantation or wet chemistry [200] [201]. A self-assembly method is of interest due to its simplicity and cost-efficiency [202]. By combining physical vapor deposition and solvent treatment (spin casting), I applied a simple hybrid method to produce appropriate silver nanoclusters for organic solar cells. Through evaporation of the silver film (~ 5 nm), nanoclusters (of ~4 nm height and ~ 25 nm widths) cover the surface. By spin casting the solvent, a thin liquid film covers the evaporated film. The silver clusters redistribute in the solution film and by evaporation of the solvent, they aggregate in larger clusters (~20 nm height and ~45 nm width). The process is influenced via physical parameters of growth from solution like evaporation rate and liquid film concentration. I show that the size of the clusters can be controlled by the thickness of the deposited film, type of solvent, and spin casting speed. I applied this method to increase the efficiency of a hybrid solution processed and vacuum deposited unsubstituted copper phthalocyanine/fullerene organic solar cells.

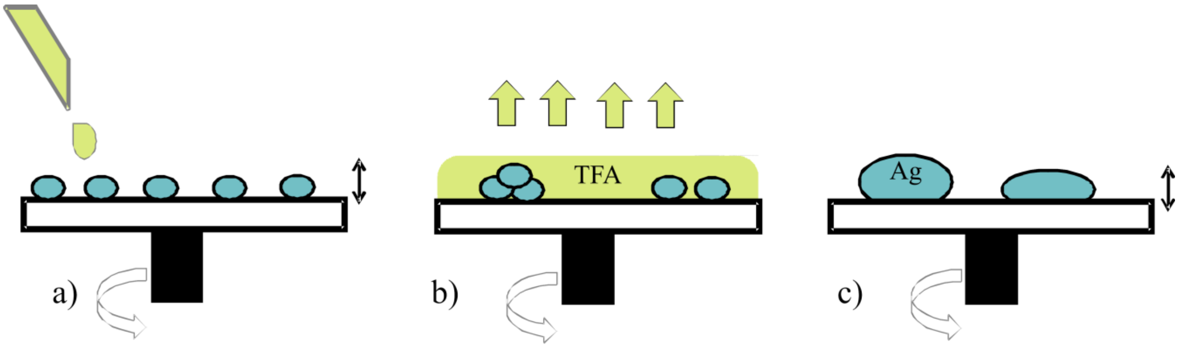

Fig. 1) Schematic drawing of formation of silver clusters by spin casting TFA solvent on evaporated silver film

Ag was evaporated onto the substrate in high vacuum for three film thicknesses: 2, 5 and 30 nm. A thin liquid film of TFA was spin coated on the Ag film in ambient atmosphere (50 rps), fig. 1a.The deposited Ag cluster becomes mobile in the liquid film and aggregates into larger clusters, simultaneously the solvent evaporates, fig. 1b. By evaporation of the solvent the Ag nanoclusters precipitate onto the substrate, fig. 1c. Nanoclusters were studied using AFM. Spectral changes were measured with UV-Vis spectroscopy.

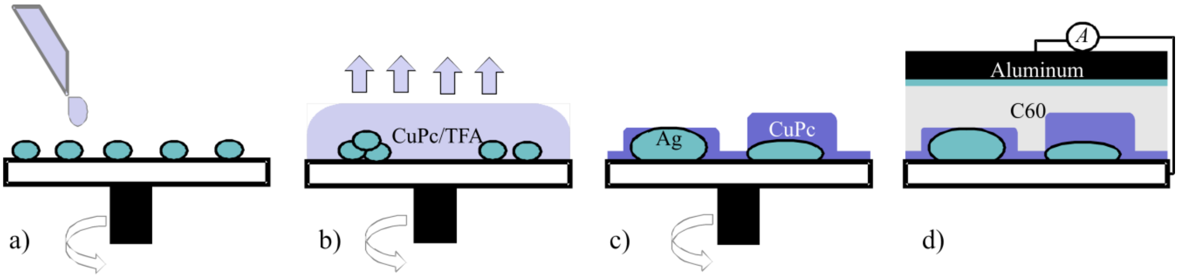

Fig. 2) Formation of silver clusters by spin casting CuPc/TFA solution on evaporated silver film

CuPc dissolved in TFA was spin coated onto the Ag film in ambient atmosphere, fig. 2a. Ag nanoclusters aggregate in the solution. Fig. 2b. Simultaneously TFA evaporates and CuPc becomes supersaturated. After complete solvent evaporation CuPc and Ag aggregates precipitate onto the substrate, fig 2c. For organic solar cells, C60, BCP and Aluminum are evaporated in high vacuum, fig. 2d. A control sample was prepared by spin casting CuPc directly onto ITO.

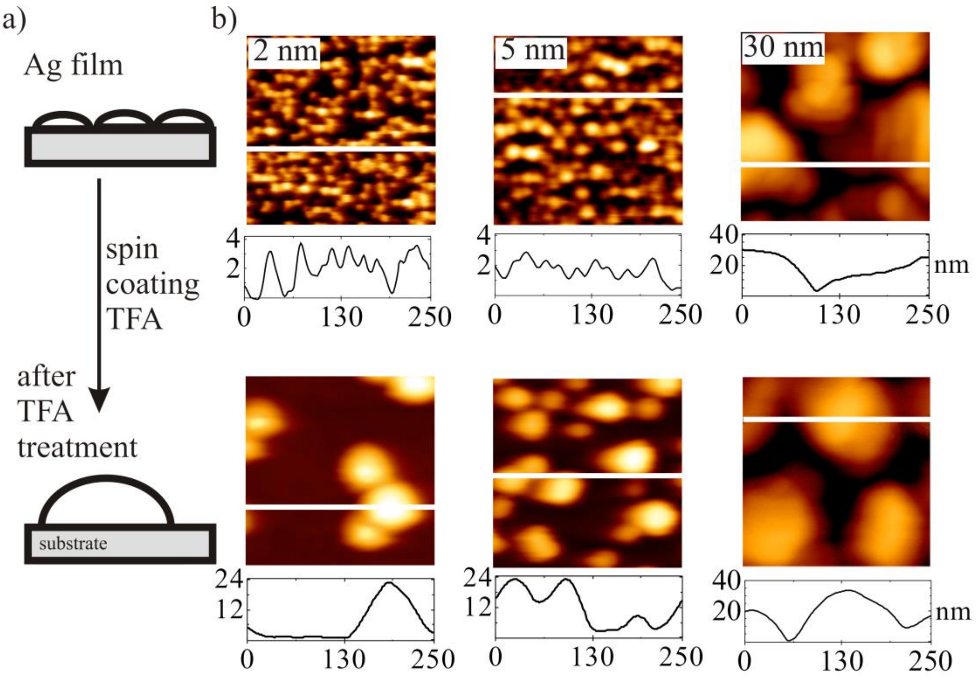

Fig. 3 a) AFM image, b) schematic drawing of silver clusters as evaporated and after solvent treatment

By deposition of Ag in high vacuum the SiO_2 substrate is covered with nanoclusters. The nanoclusters' size depends on the film thickness. The size of the nanoclusters can be changed by aggregation in liquid. The nanoclusters become mobile in the solution, redistribute and aggregate to larger nanoclusters. After solvent treatment of 2 and 5 nm thick films, the nanoclusters aggregate into particles with 20-25 nm height and 50-70 nm width. In case of 30 nm film thickness, the size does not change that much.

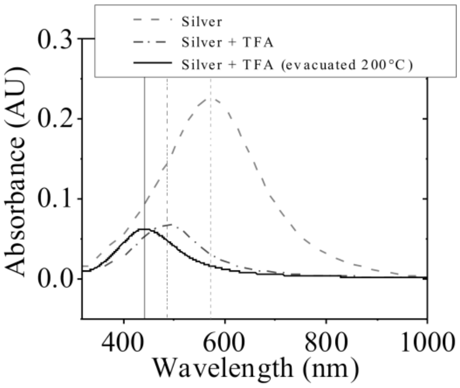

Fig. 4) Absorption spectrum of silver clusters as evaporated and after solvent treatment

The absorption band of Ag films with 5 nm thickness shifts to higher energy due to the increase in the size of the nanoclusters, fig. 4.

Using Ag particles increases the thickness of the solution processed CuPc film, fig 5a and 5b. Presumably Ag nanoclusters increase the wettability for CuPc. Using Ag nanoparticles increases the absorption twice, fig. 5c. Therefore the PCE increases by Ag nanocluster incorporation, fig. 5d.

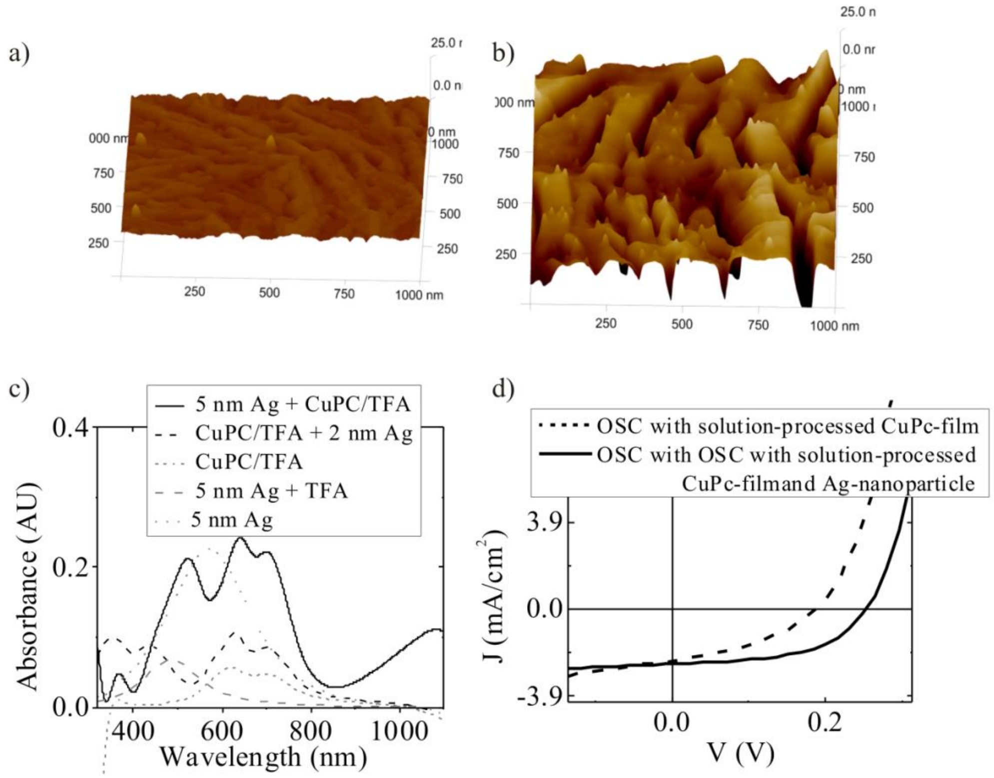

Fig. 5) CuPc/TFA film spin coated from CuPc/TFA on a) SiO_2 substrate, b) silver film evaporated on SiO_2 substrate, c) absorption spectra of CuPc nanoribbons without and with silver cluster, d) current voltage characteristics of OSC prepared with CuPc nanoribbons without and with silver cluster.

Appendix 10 – Results on sequential solution based deposition

of CuPc/acceptor thin films for application in organic solar cells

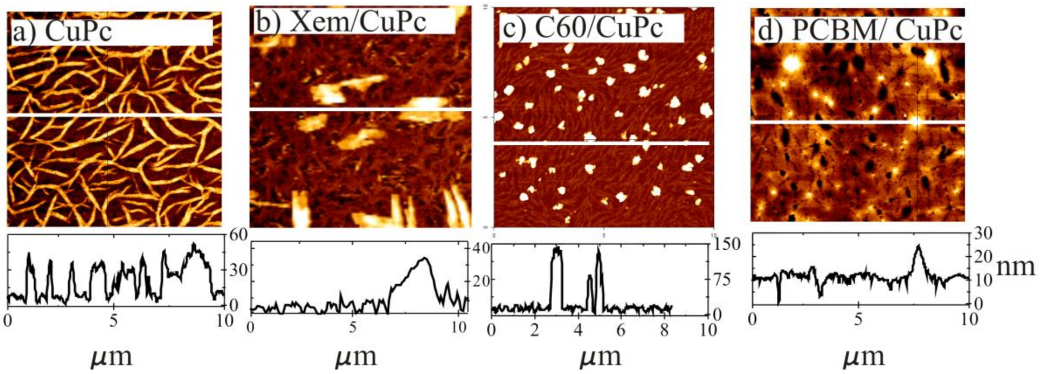

Fig. 1 a) CuPc spin casted from TFA solution on ITO (50 Ω/□), b, c, d) acceptor molecule spin casted on CuPc film

For a solution based heterojunction OSC, acceptor molecules are spin casted on CuPc structures.

Xem, is an acceptor molecule form Hemholtz-Zentrum Berlin. This molecule is dissolved in TFA, mixed with CuPc/TFA solution and spin casted onto the substrate. Unfortunately, the molecules do not wet the CuPc film and forms large aggregate. These aggregates are not favorable for OSC.

C60 is dissolved in toluene and spin casted onto the dry CuPc nanoribbon film. Again the molecule forms aggregate and the coverage is not large enough to cover the CuPc film.

PCBM dissolved in dichlorobenzene and spin casted onto dry CuPc film produce almost close film. It seems to produce promising structures for further study and preparation of a completely solution based heterojunction OSC and is going to be investigated further. This work is done with the help of Markus Regnat.

Eidesstattliche Erklärung

Hiermit erkläre ich, dass die Arbeit an keiner anderen Hochschule eingereicht sowie selbstständig und nur mit den angegebenen Mitteln angefertigt wurde.

Potsdam, den November 2012